# SYNTHESIS AND REACTIVITY OF LOW-VALENT URANIUM AND NEPTUNIUM COMPLEXES

---

A Dissertation

presented to

the Faculty of the Graduate School

at the University of Missouri-Columbia

---

In Partial Fulfillment

of the Requirements for the Degree

Doctor of Philosophy

---

By

ALEXANDER J. MYERS

Dr. Justin R. Walensky, Dissertation Supervisor

DECEMBER 2019

The undersigned, appointed by the dean of the Graduate School, have examined the dissertation entitled

SYNTHESIS AND REACTIVITY OF LOW-VALENT URANIUM AND NEPTUNIUM COMPLEXES

presented by Alexander J. Myers, a candidate for the degree of Doctor of Philosophy of Chemistry, and hereby certify that, in their opinion, it is worthy of acceptance.

---

Professor Justin R. Walensky

---

Professor Silvia S. Jurisson

---

Professor Wesley H. Bernskoetter

---

Professor Bret D. Ulery

## Acknowledgements

I would like to thank my wife, Heather Saxon, who encouraged me to go to graduate school in the first place. None of this would have happened if it wasn't for you.

My advisor, Justin Walensky, for all of his help, advice and the opportunities he has given me. I don't know how you put up with me all these years but I'm glad you did.

Wayne Lukens for all of his help; teaching me about preparing and running my SQUID and EPR samples.

Charles Barnes, Steven Kelley, and Wei Wycoff, for their help with X-ray Crystallography and NMR spectroscopy

Everyone in the Walensky group: Andrew Behrle, Pokpong Rungthanaphatsophon, Michael Tarlton, Robert Ward, Sean Vilanova, Alexander Gremillion, Andrew Lane, Andrew Breshears, Kira Behm, Matthew Vollmer, Steven Renfroe, and Jonathan Fajen.

## TABLE OF CONTENTS

Acknowledgements ..... ii

List of Figures ..... vi

List of Tables ..... x

List of Abbreviations ..... xii

Abstract ..... xiv

Introduction ..... 1

**Chapter 1: Structure and Properties of $[(4,6\text{-}^{t}Bu_2C_6H_2O)_2Se]_2An(THF)_2$, An = U, Np, and Their Reaction with *p*-Benzoquinone** ..... 6

Introduction ..... 6

Experimental ..... 7

General Considerations ..... 7

General considerations for $^{237}Np$ ..... 8

Crystallographic Data Collection and Structure Determination ..... 10

Magnetic Measurements ..... 12

EPR Experimental ..... 17

Results and Discussion ..... 18

Conclusion ..... 30

**Chapter 2: U(III) and Th(IV) Alkyl Complexes as Potential Starting Materials** ..... 31

Introduction ..... 31

Experimental ..... 32

General Considerations ..... 32

Crystallographic Data Collection and Structure Determination ..... 36

Magnetism Measurements ..... 38

Results and Discussion ..... 40

Conclusion ..... 48

**Chapter 3: Synthesis and Utility of a Neptunium(III) Hydrocarbyl Complex** ..... 49

Introduction ..... 49

Experimental ..... 51

General considerations ..... 51

General considerations for $^{237}$Np ..... 52

Crystallographic Data Collection and Structure Determination ..... 53

Magnetic Measurements ..... 55

Results and Discussion ..... 57

Conclusion ..... 65

**Chapter 4: Formation of Np(IV)-Chalcogenido Bonds from E-E Bond Cleavage with a Np(III) Aryloxide Complex** ..... 66

Introduction ..... 66

Experimental ..... 67

General Considerations for $^{237}$Np ..... 67

Crystallographic Data Collection and Structure Determination ..... 69

Results ..... 71

**Appendix A: Influence of Substituents on the Electronic Structure of Mono- and Bis(Phosphido) Thorium(IV) Complexes** ..... 74

Introduction ..... 74

Experimental ..... 76

General Considerations ..... 76
Computational Details ..... 81
Crystal Structure Determination and Refinement ..... 82
Results and Discussion ..... 84
Spectroscopy and TD-DFT Calculations ..... 90
Conclusion ..... 99
**Appendix B: Coordination Chemistry and QTAIM Analysis of Homoleptic Dithiocarbamate Complexes, $M(S_2CN^iPr_2)_4$, M = Ti, Zr, Hf, Th, U, Np** ..... 101
Introduction ..... 101
Experimental ..... 103
General Considerations ..... 103
General Considerations for $^{237}Np$ ..... 103
Crystallographic Data Collection and Structure Determination ..... 108
Computational Details ..... 110
Results ..... 111
Topological Properties of the Electron Density ..... 116
Integrated Properties of the Electron Density ..... 117
Discussion ..... 119
Conclusion ..... 120
References ..... 121
Vita ..... 155

## List of Figures

**Figure 1.** Radial Distribution Plot ..... 3

**Figure 2.** Graphical representation of orbital extensions ..... 4

**Figure 1-1.** Equation used to calculate molar susceptibility ..... 13

**Figure 1-2.** Variable temperature magnetic susceptibility of **1** without ferromagnetic correction ..... 15

**Figure 1-3.** Variable temperature magnetic susceptibility of **2** without ferromagnetic correction ..... 15

**Figure 1-4.** Variable temperature magnetic susceptibility of **3a-c** without ferromagnetic correction ..... 16

**Figure 1-5.** Reaction scheme of $AnCl_4(DME)_x$ with two equivalents of $K_2[^{Ar}OSeO^{Ar}]$ in THF ..... 19

**Figure 1-6.** Thermal ellipsoid plot of **1** shown at the 50% probability level ..... 20

**Figure 1-7.** Variable temperature magnetic susceptibility of **1** corrected for the presence of a ferromagnetic impurity ..... 21

**Figure 1-8.** Thermal ellipsoid plot of one of the two independent molecules of **2** shown at the 50% probability level ..... 22

**Figure 1-9.** Variable temperature magnetic susceptibility of **2** from 10 K to 300 K ..... 23

**Figure 1-10.** Variable field magnetization of **2** at 2 K and 3 K ..... 24

**Figure 1-11.** EPR spectrum and simulation for **2** ..... 25

**Figure 1-12.** Electronic absorption spectra of **3** in toluene with NIR region of interest in the inset ..... 26

**Figure 1-13.** Thermal ellipsoid plot of **3** shown at the 50% probability level ..... 27

**Figure 1-14.** Variable temperature magnetic susceptibility of **2** from 2 K to 20 K and **3b** at 1 T from 2 K to 20 K ..... 28

**Figure 1-15.** Variable temperature magnetic susceptibility of **3a**, **3b**, and **3c** corrected for the presence of a ferromagnetic impurity ..... 29

**Figure 1-16.** Variable temperature magnetic susceptibility of **3** at 1T from 10 K to 300 K ..... 30

**Figure 2-1.** Equation used to calculate molar susceptibility ..... 39

**Figure 2-2.** Reaction scheme of $UI_3(THF)_4$ with three equivalents of $K[Me_2NC(H)C_6H_5]$ in $Et_2O$ ..... 41

**Figure 2-3.** Thermal ellipsoid plot of **1** and **2** shown at the 50% probability level..... 42

**Figure 2-4.** Variable field magnetization data at 2 K, 3 K, 5 K, and 300 K ..... 43

**Figure 2-5.** Variable temperature magnetic moment of **1**..... 44

**Figure 2-6.** Reaction scheme of $ThCl_4(DME)_2$ with four equivalents of $K[Me_2NC(H)C_6H_5]$ in THF ..... 45

**Figure 2-7.** Reaction scheme of **1** and **2** with four equivalents of $HS_2C[2,6\text{-}(Mes)_2C_6H_3]$ in THF..... 47

**Figure 2-8.** Thermal ellipsoid plot of **3** shown at the 50% probability level ..... 48

**Figure 3-1.** Equation used to calculate molar susceptibility ..... 56

**Figure 3-2.** Reaction Scheme of the synthesis of complexes **1**, **2**, and **3**..... 57

**Figure 3-3.** Thermal ellipsoid plot of **1** shown at the 50% probability level ..... 58

**Figure 3-4.** Electronic absorption spectrum of **2** in toluene..... 60

**Figure 3-5.** Thermal ellipsoid plot of **2** shown at the 50% probability level ..... 61

**Figure 3-6.** Thermal ellipsoid plot of **3** shown at the 50% probability level ..... 62

**Figure 3-7.** Variable-temperature magnetic moment of **2** and **3** at 0.1 T .....63

**Figure 4-1.** Thermal ellipsoid plots of **1** shown at the 50% probability level.....71

**Figure 4-2.** Thermal ellipsoid plots of **2** shown at the 50% probability level.....72

**Figure 4-3.** Thermal ellipsoid plots of **3** shown at the 50% probability level.....72

**Figure 4-4.** Thermal ellipsoid plots of **4** shown at the 50% probability level.....73

**Figure 4-5.** Thermal ellipsoid plots of **5** shown at the 50% probability level.....73

**Figure A-1**. Reaction scheme of $(C_5Me_5)_2ThCl_2$ with $KP(Mes)_2$ in $Et_2O$ .....85

**Figure A-2**. Reaction scheme of $(C_5Me_5)_2ThCl_2$ with $KP(Mes)(CH_3)$ in toluene .....85

**Figure A-3.** Reaction scheme of $(C_5Me_5)_2Th(CH_3)Cl$ with $KP(Mes)_2$ and with $KP(Mes)(SiMe_3)$.....86

**Figure A-4.** Reaction scheme of $(C_5Me_5)_2ThCl_2$ with 2 equivalents of $K[P(Mes)(SiMe_3)]$ .....87

**Figure A-5.** Thermal ellipsoid plots of **1** and **4** shown at the 50% probability level. The hydrogen atoms have been omitted for clarity.....88

**Figure A-6.** Thermal ellipsoid plot of **2** shown at the 50% probability level. The hydrogen atoms have been omitted for clarity .....88

**Figure A-7.** Thermal ellipsoid plot of **6** shown at the 50% probability level. The hydrogen atoms have been omitted for clarity .....89

**Figure A-8.** Thermal ellipsoid plot of **7** shown at the 50% probability level. The hydrogen atoms have been omitted for clarity .....89

**Figure A-9.** Molecular orbital (MO) diagram of $(C_5Me_5)_2Th[PH(Mes)]_2$ and $(C_5Me_5)_2Th[P(CH_3)(Mes)]_2$ **2** .....94

**Figure A-10.** MO diagrams of **1**, **5**, and **6**.....95

**Figure A-11.** Comparison between experimental and theoretical spectra when using a GGA functional ..... 97

**Figure A-12.** Comparison of experimental and theoretical absorption spectra for $(C_5Me_5)_2Th[PH(Mes)]_2$ (left) and $(C_5Me_5)_2Th[P(Mes)(SiMe_3)]_2$ **6** ..... 98

**Figure B-1.** First-order perturbation theory equation ..... 102

**Figure B-2.** Reaction scheme of $MCl_4$ with four equivalents of **1** ..... 112

**Figure B-3.** Electronic absorption spectrum of **7** from 600-1000 nm ..... 113

**Figure B-4.** Thermal ellipsoid plots of **4** and **7** shown at the 50% probability level..... 114

## LIST OF TABLES

**Table 1-1.** X-ray crystallography data is shown for complexes **1**, **2**, and **3**.....10

**Table 1-2.** Selected bond distance (Å) and angles (°) for complexes **1**, **2**, and **3**.....12

**Table 1-3.** Magnetic susceptibility results for **3**.....17

**Table 1-4.** EPR fitting parameters (9.08528 GHz) using an effective S = ½ spin Hamiltonian.....18

**Table 1-5.** Spectroscopic splitting factors and magnetic moments of $^{2}F_{5/2}$ substates.....28

**Table 2-1.** X-ray crystallography data is shown for complexes **1**, **2**, **3**, and **4**.....37

**Table 3-1.** X-ray crystallography parameters of complexes **1-3**.....54

**Table 4-1.** X-ray crystallography data is shown for complexes **1-5**.....70

**Table A-1.** X-ray crystallography data is shown for complexes **1-7**.....82

**Table A-2.** Selected bond distances (Å) and angles (deg) for complexes **1**, **2**, and **4**–**7**..87

**Table A-3.** Summary of $^{31}$P NMR chemical shifts (ppm) in $C_6D_6$.....91

**Table A-4.** $^{31}$P NMR Resonances for Metallocene Thorium Phosphido Complexes (Mes = $C_6H_2Me_3$-2,4,6).....92

**Table A-5.** Natural bonding orbitals (NBOs) in **1** and a nitrogen-substituted analog, **N**.96

**Table B-1.** X-ray crystallographic data shown for complex **2-7**.....109

**Table B-2.** $^{1}$H NMR Resonances for the Isopropyl Methyl and Methine Protons for Complexes **1**–**7**.....112

**Table B-3.** Selected bond distances (Å) and angles (deg) for complexes **2**–**7**.....115

**Table B-4.** Comparison of the Experimental and Theoretical M–S Bond Lengths in $M(S_2CN^{i}Pr_2)_4$ (M = Ti, Zr, Hf, Th, U, Np).....115

**Table B-5.** Topological Properties at the M–S BCPs of the PBE0-Derived Electron Densities.....117

**Table B-6.** Integrated QTAIM Properties of the PBE0-Derived Electron Densities .....118

## LIST OF ABBREVIATIONS

Ph ..... Phenyl

$^{t}$Bu …… *tert*-butyl

$^{n}$Bu ……..…… normal-butyl

$^{i}$Pr ……..…… Isopropyl

Me ……. Methyl

Et ……. Ethyl

Pz …….. Pyrazolyl

THF …… Tetrahydrofuran

DME ……... 1,2-dimethoxyethane

$Et_2O$ ……. Diethyl ether

HCl …….. Hydrochloric acid

Mes …….. 1,3,5-trimethylbenzene

$^{Ar}OSeO^{Ar}$ ……... $[(4,6\text{-}^{t}Bu_2C_6H_2O)_2Se]^{2-}$

FOD ……. 6,6,7,7,8,8,8-heptafluoro-2,2-dimethyl-3,5-octanedione

$H_2$salan-$^{t}Bu_2$ …. N,N′-bis(2-hydroxybenzyl-3,5-di-tert-butyl)-1,2-dimethylaminomethane

Tp* ……... Hydrotris(3,5-dimethylpyrazolyl)borate

$L^{Ar\text{-}H}$ ……... $L^{Ar}$ =trans-calix[2]benzene[2]pyrrole

dddt ……. 5,6-dihydro-1,4-dithiine-2,3-dithiolate

DPPH ……... 2,2-diphenyl-1-picrylhydrazyl

DMBA ……... N,N-dimethylbenzylamide

OTf …… Trifluoromethanesulfonate

LHe …… Liquid helium

PTFE …….. Polytetrafluoroethylene

UV/vis/NIR ……... Ultraviolet/visible/near infrared

DFT ……... Density Functional Theory

LMCT ……. Ligand-to-Metal Charge Transfer

SMM ……. Single Molecule Magnet

RS ……. Russell Saunders

CCDC ……...……... The Cambridge Crystallographic Data Centre

SQUID …….. Superconducting Quantum Interference Device

MPMS ……. Magnetic Property Measuring System

EPR ……. Electron paramagnetic resonance

NMR ……. Nuclear Magnetic Resonance

FT-IR ……. Fourier-transform Infrared

HMQC ……. Heteronuclear Multiple-Quantum Correlation

$\chi_{mol}$ ……... Molar Susceptibility

$\chi_{QW}$ ……...… Contribution to the Susceptibility due to the Quartz Wool

$\chi_{dia}$ …….. Diamagnetic Correction of the Ligands

$M_{meas}$ ……. Measured Magnetization

$M_{ferro}$ …… Ferromagnetic Magnetization of the Ferromagnetic Impurity

# Abstract

Chapter 1 reports the synthesis and characterization of U(IV) and Np(IV) selenium bis(phenolate) complexes. The reaction of the U(IV) complex with half an equivalent of *p*-benzoquinone results in the formation of a U(V)–U(V) species with a bridging reduced quinone. This represents a rare example of high-valent uranium chemistry as well as a rare example of a neptunium aryloxide complex.

In Chapters 2 and 3 the synthesis and characterization of a rare U(III) hydrocarbyl complex, $U[\eta^4\text{-}Me_2NC(H)C_6H_5]_3$, and the first structurally characterized transuranic hydrocarbyl complex, $Np[\eta^4\text{-}Me_2NC(H)C_6H_5]_3$, complex, has been generated with four equivalents of the $K[Me_2NC(H)C_6H_5]$ ligand. In the analogous Th(IV) reaction, C–H bond activation of a methyl group of one dimethylamine was observed yielding $Th[\eta^4\text{-}Me_2NC(H)C_6H_5]_2[\eta^5\text{-}(CH_2)MeNC(H)C_6H_5]$ with a dianionic DMBA ligand. The utility of these complexes as starting materials has been analyzed using a bulky dithiocarboxylate ligand to yield tetravalent actinide species for U and Th but Np maintains the trivalent oxidation state.

Chapter 4 describes the on-going synthesis and reactivity of $Np(OAr)_3$ (Ar = 2,6-di-*tert*-butylphenoxide) utilizing $Np[\eta^4\text{-}Me_2NC(H)C_6H_5]_3$ as a Np(III) starting material. The coordination and oxidation chemistry is explored with $[^nBu_4N]N_3$, $(C_6H_5CO)_2O_2$ and $Ph_2S_2$ resulting in a bridged Np(III)/Np(III) azide complex with an outer sphere $^nBu_4N$ and Np(IV) species, respectively.

Appendix A summarizes a systematic approach to comparing the molecular structure and bonding in homoleptic transition-metal and actinide complexes by synthesizing a series of dithiocarbamates, $M(S_2CN^iPr_2)_4$ (M = Ti, Zr, Hf, Th, U, Np). These complexes have

been characterized through spectroscopic and X-ray crystallographic analysis, and their bonding has been examined using DFT calculations. Computational results indicate that the covalent character associated with the M−S bonds shows the trend of Hf < Zr < Th < Ti < U ≈ Np.

Appendix B outlines a series of metallocene thorium complexes with mono- and bis(phosphido) ligands with varying hues from dark red-purple to pale yellow. While all of these complexes bear a mesityl group on phosphorus, the electronic structure observed differs depending on the other substituent (Mes, Me, $SiMe_3$, or H). This sparked an investigation of the electronic structure of these complexes using $^{31}P$ NMR and electronic absorption spectroscopy in concert with time-dependent DFT calculations.

# Introduction

The United States is currently the world's leading producer of nuclear energy. The U.S. operates 65 pressurized water reactors and 33 boiling water reactors to produce over 800 billion kWh a year of electricity.[1] Both types of water reactors use enriched uranium as their fuel source and have produced over 80,000 metric tons of spent nuclear fuel.[2] As a byproduct from the irradiation of U-235 and U-238, there are large quantities of Np-237 commonly present in used nuclear waste. The long half-life of Np-237 ($t_{1/2}$ = 2.14 million years), via alpha decay (4.7 MeV),[3] makes Np-237 a long-term hazard that will be one of the most significant contributors to the radioactivity found in nuclear waste 10,000 years from now.[4] With over 3 metric tons of Np-237 produced every year,[5] a comprehensive understanding of the chemical properties and speciation is necessary for the development of advanced separation techniques and disposal. Applications of Np-237 are limited; Np-237 can be used for the production of Pu-238, which is used as a thermoelectric generator for NASA spacecraft,[6] but the main focus is on storage and disposal.

Disposal of nuclear waste is a major and growing public health threat. A large portion of our waste is held in storage pools on site at the nuclear power plants where it was generated.[7] These pools are supposed to be used to hold the waste for a short period of time because the isotopes with a short half-life contribute to: 1) the immediate high radioactivity of the waste until the short-lived isotopes decay, and 2) once decayed the radiological properties of the short-term isotopes are no longer an issue when selecting a suitable waste container. However, we do not have a permanent solution for the long-term storage of our nuclear waste, and we are currently dealing with the repercussions.

The Hanford site, for example, used for the production of plutonium during WWII, built 149 waste storage tanks prior to 1965, for the disposal of chemicals used to dissolve fuel rods so plutonium could be recovered.[8] These tanks were designed as a temporary measure with a lifetime up to 25 years, but a longer-term solution has not been implemented. Now, over 60 tanks are leaking nuclear waste, damaging the surrounding environment and ecology.[9] Designing containers based on specific chemical and radiological properties of the waste contained is a start towards storage with a longer-term solution in mind. In order to best understand the properties of the nuclear waste, it is advantageous to separate the individual isotopes and elements to simplify reactivity. Despite the prevalence of Np-237 in nuclear waste, the chemistry of neptunium is largely unexplored, especially compared to the lighter actinides, thorium and uranium. This discrepancy is exemplified by the number of crystal structures in the *Cambridge Crystallographic Data Centre* (*CCDC*) for Th: 1087, U: 6816, and Np: 244.[10] Most neptunium chemistry has been conducted using aqueous and atmospheric conditions, which is dominated by the trans-oxo neptunyl motif, to better elucidate the reactivity and mobility under environmental conditions.

The inert atmosphere chemistry of neptunium has largely been neglected for a number of reasons, such as a lack of starting materials, the cost of infrastructure required to safely handle transuranic elements and the required safety support staff. However, conducting chemistry under inert atmosphere allows access to low-valent oxidations states and bonding motifs not accessible under oxygen; for example, Gaunt, Evans and co-workers recently synthesized a molecule with a +2 formal oxidation state for neptunium.[11] This allowed for a density functional theory (DFT) investigation into the electronic

configuration across the series (Th-Pu, excluding Pa) of the divalent actinides. This study showed that ground state electron configuration changes from $5f^0 6d^2$ to $5f^6 6d^0$ between $Th^{2+}$ and $Pu^{2+}$. The study of low-valent metals in nuclear waste is particularly relevant to the Hanford site. A previously unknown Tc(I) complex was discovered in the waste tanks due to the highly reducing conditions generated from radiolysis products.[12,13] This complex was not able to be removed by ion-exchange, which is effective for the removal of $TcO_4^-$, and was found to be difficult to oxidize.[14] Examining these complexes with unique oxidation states can help elucidate the chemistry of elements in nuclear waste, allowing for further methods to be developed for effective separation.

One of the methods for utilizing new ligands for separation of fission products in nuclear waste is to capitalize on the differences in covalency between the metals and extractor ligands.

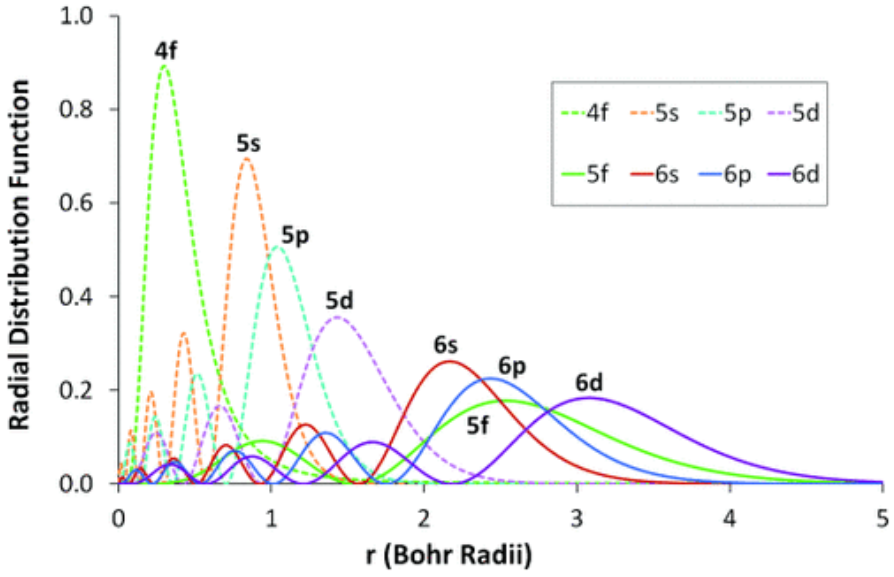


**Figure 1.** Radial Distribution Plot.[15]

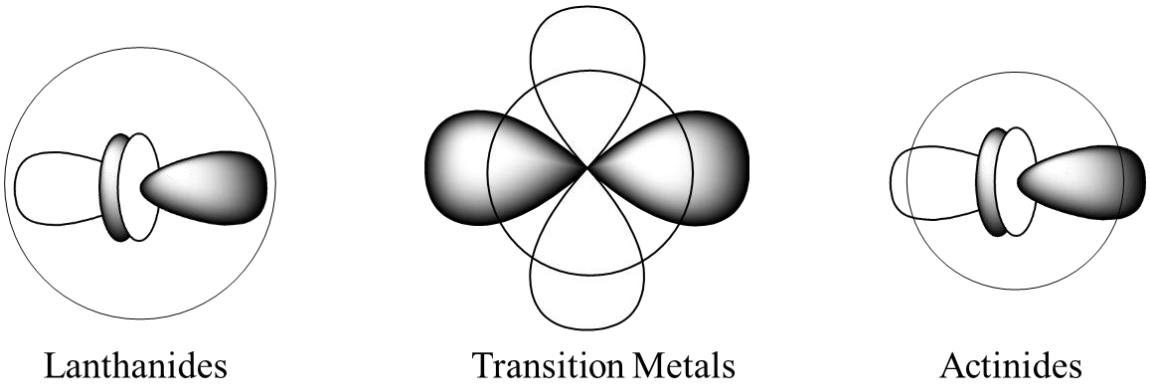


**Figure 2.** Graphical representation of orbital extensions.[16]

The ability for the actinides to participate in covalent bonding may be why there is a better selectively in extractor ligands that employ softer donor atoms. The radial extension of the 5f-orbitals (Figure 1 and 2) allows the actinides to participate in bonding with a higher degree of covalency than the more contracted 4f-orbitals of the lanthanides, where the bonding is primarily ionic in nature. An approach to understanding the differences in covalency between different metals is to investigate a series of complexes where the metal varies but the ligand environment stays the same.

One of the goals of this research is to describe how to synthesize actinide complexes that can be compared to the other complexes utilizing elements found in nuclear waste. This has proved challenging for neptunium, in particular the +4 oxidation state, due to the lack of starting materials. In 2014, Gaunt reported the procedure for $NpCl_4(DME)_2$;[17] this new starting material allowed entry into neptunium chemistry that bypasses the need for neptunium metal, which was necessary for the previous starting material $NpI_3(THF)_4$. Utilizing the new $NpCl_4(DME)_2$, this research primarily explores the divergent chemistry of low-valent Np and U conducted under inert atmosphere and allows for the study of

respective structure and bonding between transition metals, lanthanides and actinide complexes.

# Chapter 1: Structure and Properties of $[(4,6\text{-}^{t}Bu_2C_6H_2O)_2Se]_2An(THF)_2$, An = U, Np, and Their Reaction with *p*-Benzoquinone†

† This chapter is based on a manuscript that was submitted to and accepted by Chemical Communications and can be cited as: **Myers, A. J.**; Rungthanaphatsophon, P.; Behrle, A. C.; Vilanova, S. P.; Kelley, S. P.; Lukens, W. W.; Walensky, J. R. Structure and Properties of $[(4,6\text{-}^{t}Bu_2C_6H_2O)_2Se]_2An(THF)_2$, An = U, Np, and Their Reaction with *p*-Benzoquinone, *Chem. Commun.* **2018**, *54*, 10435.

## Introduction

The coordination chemistry and reactivity of the actinides offer insight into their structure and bonding, which in turn improves our understanding of the behavior of these elements especially with regard to the nuclear fuel cycle. Transuranic actinides are particularly understudied even compared with lighter actinides due to the difficulty in obtaining these elements and the infrastructure required to handle them safely.

Alkoxide and aryloxide ligands have served a significant role in advancing our understanding of actinide chemistry. The highly electronegative oxygen atoms provide a more ionic interaction with the actinide, which enhances the stability of the resulting complexes. Oxygen-based ligands have demonstrated the ability to isolate complexes with U(II),[18] U(III),[19–21] U(V),[22] and U(VI),[23] but especially with respect to tetravalent actinides.[24–29]

We recently examined the structures of diamagnetic complexes with the selenium bis(phenolate) ligand, $[(4,6\text{-}^{t}Bu_2C_6H_2O)_2Se]^{2-}$, $^{Ar}OSeO^{Ar}$.[30] This dianionic, chelating ligand effectively stabilizes tetravalent metal complexes of Ti, Zr, Hf, Ce, and Th, and we endeavored to extend this study to uranium and neptunium. Herein, we report the

synthesis of the U(IV) and Np(IV) complexes. The reactivity of these complexes with *p*-benzoquinone has been explored. With U(IV), this reaction affords a dinuclear U(V)–U(V) compound bridged by *p*-hydroquinone dianion. However, the addition of *p*-benzoquinone to the Np(IV) species produces no reaction. The magnetic, spectroscopic, and structural properties of these complexes are detailed.

**General considerations**

The syntheses and manipulations described below were conducted using standard Schlenk and glove box techniques. Reactions were conducted in a Vacuum Atmospheres inert atmosphere ($N_2$) glove box. [$UCl_4$],[31] and [$NpCl_4(DME)_2$][17] were synthesized as previously described. $K_2[^{Ar}OSeO^{Ar}]$ was synthesized following the previously published procedures using $KN(SiMe_3)_2$ instead of $NaN(SiMe_3)_2$.[30] *p*-Benzoquinone was used as received (Sigma-Aldrich). All solvents were dried by passing through a solvent purification system, MBRAUN, USA and stored over activated 4 Å molecular sieves. Benzene-$d_6$ (Cambridge Isotope Laboratories) was degassed by three freeze-pump-thaw cycles and stored over activated 4 Å molecular sieves. All $^1$H NMR data were obtained on a 600 MHz or 300 MHz DRX Bruker spectrometer. $^1$H NMR shifts given were referenced internally to the residual solvent peak at δ 7.16 ppm ($C_6D_5H$) or δ 2.08 ppm ($C_7D_7H$). Infrared spectra were recorded as KBr pellets on a Perkin-Elmer Spectrum One FT-IR spectrometer. Elemental analyses were performed at the University of California, Berkeley Microanalytical Facility using a Perkin-Elmer Series II 2400 CHNS analyzer. Single X-ray crystal structure determinations were performed at the University of Missouri-Columbia.

**General considerations for $^{237}$Np**.

Caution! $^{237}$Np is an α-emitting radionuclide (4.958 MeV, $t_{1/2}$ = 2.14 x$10^6$ years, a = 0.7 mCi $g^{-1}$). This research was conducted in a radiological laboratory with appropriate counting equipment and analysis of hazards for the safe handling and manipulation of radioactive materials. Reactions were performed in a Vacuum Atmospheres inert atmosphere (Ar) glove box operated at negative pressure relative to the laboratory atmosphere. Electronic absorption measurements were recorded on a sealed 1 cm quartz cuvette with a Varian Cary 5000 UV/vis/NIR spectrophotometer.

**Synthesis of U[$^{Ar}$OSeO$^{Ar}$]$_2$(THF)$_x$, 1**. A 20 mL scintillation vial was charged with $UCl_4$ (94 mg, 0.25 mmol), $K_2$[$^{Ar}$OSeO$^{Ar}$] (280 mg, 0.49 mmol), and THF (10 mL). The solution was stirred overnight at room temperature. THF was removed in vacuo, replaced with toluene and stirred an additional 30 minutes. After filtering through Celite the toluene was removed in vacuo (2 hours) to yield a green power (290 mg, 86%). Depending on the extent of vacuum treatment, products with varying degrees of THF were isolated. After exposing to vacuum overnight (>12 hours), the solvent free product was isolated as confirmed by elemental analysis. X-ray quality crystals were grown from a concentrated toluene solution at -20 °C. $^1$H NMR ($C_6D_6$, 600 MHz, 298 K): δ 15.2 (br s, 4H, Ar*H*), 9.62 (br s, 4H, Ar*H*), 6.07 (br s, 36H, $^t$Bu), 3.45 (br s, 44H, $^t$Bu and THF), -10.3 (br s, 8H, THF). IR ($cm^{-1}$): 2960 (vs), 2904 (s), 2868 (s), 1460 (s), 1429 (vs), 1398 (m), 1360 (m), 1282 (vs), 1256 (vs), 1225 (m), 1203 (m), 1137 (w), 1095 (m), 1028 (m), 914 (m), 867 (m), 847 (w), 835 (s), 763 (m), 733 (s), 696 (w), 620 (w), 527 (m), 440 (m). Anal. calcd for $C_{56}H_{80}O_4Se_2U_1$: C, 55.44; H, 6.65. Found C, 55.50; H, 6.65.

**Synthesis of Np[$^{Ar}$OSeO$^{Ar}$]$_2$(THF)$_2$, 2**. A 20 mL scintillation vial was charged with $NpCl_4(DME)_2$ (21.4 mg, 0.038 mmol), $K_2[^{Ar}OSeO^{Ar}]$ (43.3 mg, 0.077 mmol), and THF (2.5 mL). The solution was stirred for 18 h at room temperature and the THF removed in vacuo. The residue was extracted into toluene (2x2 mL) and filtered through Celite. The toluene was removed in vacuo to yield a yellow power (54 mg). X-ray quality crystals were grown from a concentrated toluene solution at -35 °C. $^1$H NMR ($C_7D_8$, 300 MHz, 298 K): δ14.3 (br s, Ar*H*), 11.2 (br s, Ar*H*), 3.6 (br s, $^t$Bu), -5.7 (br s, $^t$Bu), -10.8 (br s, THF).

**Synthesis of {U[$^{Ar}$OSeO$^{Ar}$]$_2$(THF)}$_2$(μ$_2$-OC$_6$H$_4$O), 3.** A 20 mL scintillation vial was charged with $U[^{Ar}OSeO^{Ar}]_2(THF)_2$ (200 mg, 0.15 mmol), *p*-benzoquinone (8 mg, 0.074 mmol), toluene (5 mL), and a stir bar. The solution was stirred overnight at room temperature and then concentrated to ca. 1 mL before being placed in the freezer (-20 °C) for several days. The precipitate was collected and dried to yield a black crystalline powder (90 mg, 46%). X-ray quality crystals were grown from a concentrated toluene solution at -20 °C. $^1$H NMR ($C_6D_6$, 600 MHz, 298 K): δ 9.73 (br s, 8H, Ar*H*), 8.87 (br s, 8H, Ar*H*), 1.50 (s, 72H, $^t$Bu), 1.25 (s, 72H, $^t$Bu). THF resonances were not observed. IR ($cm^{-1}$): 2960 (vs), 2904 (m), 2868 (m), 1488 (m), 1461 (m), 1430 (vs), 1398 (m), 1361 (m), 1281 (s), 1244 (s), 1222 (m), 1203 (m), 1137 (w), 1094 (m), 1029 (w), 914 (m), 878 (m), 846 (m), 835 (vs), 759 (w), 734 (m), 695 (w), 618 (w), 533 (m), 446 (m). Anal. calcd for $C_{126}H_{180}O_{12}Se_4U_2$: C, 56.50; H, 6.77. Found C, 56.65; 6.56.

**Attempted Synthesis of {Np[$^{Ar}$OSeO$^{Ar}$]$_2$(THF)}$_2$(μ$_2$-OC$_6$H$_4$O).** A 1 mL aliquot of a $7.2x10^{-3}$ M stock solution of *p*-benzoquinone in toluene was added to

$Np[^{Ar}OSeO^{Ar}]_2(THF)_2$ (19.7 mg, 0.015 mmol) and stirred for 15 h. The only product that could be isolated was $Np[^{Ar}OSeO^{Ar}]_2(THF)_2$.

**Crystallographic Data Collection and Structure Determination**

The selected single crystals for the uranium complexes were mounted on nylon cryoloops using viscous hydrocarbon oil. The selected single neptunium crystal was coated with viscous hydrocarbon oil inside the glove box before being mounted on a nylon cryoloop using Devcon 2 Ton epoxy. The X-ray data were collected on a Bruker CCD diffractometer with monochromated Mo-Kα radiation (λ= 0.71073 Å). The data collection and processing utilized the Bruker Apex2 suite of programs.[32] The structures were solved using direct methods and refined by full-matrix least-squares methods on $F^2$ using Bruker SHELX-2014/7 program.[33] All non-hydrogen atoms were refined with anisotropic displacement parameters. All hydrogen atoms were placed at calculated positions and included in the refinement using a riding model. Thermal ellipsoid plots were prepared by using Olex2[34] with 50% of probability displacements for non-hydrogen atoms.

**Table 1-1.** X-ray crystallography data is shown for complexes **1**, **2**, and **3**.

| | **1** | **2** | **3** |
|---|---|---|---|
| CCDC deposit number | 1851817 | 1851819 | 1851820 |
| Empirical formula | $C_{64}H_{96}O_6Se_2U•(C_7H_8)_2$ | $C_{64}H_{96}O_6Se_2Np•(C_7H_8)_2$ | $C_{132}H_{186}O_{12}Se_4U_2$ |
| Formula weight (g/mol) | 1541.63 | 1540.59 | 2756.70 |

| Crystal habit, color | Prism, green | Plate, yellow | Prism, black |
|---|---|---|---|
| Temperature (K) | 173(2) | 296(2) | 100(2) |
| Space group | $P2_1$ | $P2_1$ | $P$-1 |
| Crystal system | Monoclinic | Monoclinic | Triclinic |
| Volume (Å$^3$) | 3742.5(7) | 7351.8(9) | 3812.7(5) |
| $a$ (Å) | 10.6644(11) | 17.5780(12) | 14.3383(9) |
| $b$ (Å) | 20.483(2) | 20.5093(15) | 14.4734(9) |
| $c$ (Å) | 17.7085(18) | 21.1111(15) | 21.5834(19) |
| $\alpha$ (˚) | 90.00 | 90.00 | 102.642(1) |
| $\beta$ (˚) | 104.649(1) | 104.991(1) | 98.558(1) |
| $\gamma$ (˚) | 90.00 | 90.00 | 114.946(1) |
| $Z$ | 2 | 4 | 1 |
| Calculated density (Mg/m$^3$) | 1.368 | 1.392 | 1.201 |
| Absorption coefficient (mm$^{-1}$) | 3.189 | 2.453 | 3.123 |
| Final R indices [I > 2σ(I)] | R = 0.0298 $R_W$ = 0.0609 | R = 0.0722 $R_W$ = 0.1193 | R = 0.0360 $R_W$ = 0.0931 |

**Table 1-2.** Selected bond distance (Å) and angles (°) for complexes **1**, **2**, and **3**.

| | **1** | **2** | **3** |
|---|---|---|---|
| M1-O1 | 2.189(3) | 2.207(11) | 2.163(3) |
| M1-O2 | 2.185(4) | 2.228(11) | 2.149(3) |
| M1-O3 | 2.214(4) | 2.168(9) | 2.145(3) |
| M1-O4 | 2.223(4) | 2.214(10) | 2.140(3) |
| M1-O5 | 2.530(4) | 2.490(9) | 2.097(3) |
| M1-O6 (THF) | 2.512(4) | 2.488(11) | 2.508(3) |
| M1-Se1 | 3.2606(6) | 3.1289(15) | 3.1475(5) |
| M1-Se2 | 3.1642(6) | 3.2287(17) | 3.1995(5) |
| O1-M1-O2 | 105.86(15) | 103.2(4) | 100.46(11) |
| O3-M1-O4 | 102.52(13) | 107.4(4) | 93.11(11) |
| O5-M1-O6 | 144.82(14) | 144.1(4) | 74.64(10) |

**Magnetic Measurements**

In an argon filled glovebox, **1** (28.8 mg), **2** (11.2 mg) and **3a-c** (9.6 mg, 16.5 mg, and 9.8 mg, respectively) and were loaded into 3 mm OD quartz tubes by sandwiching them between two plugs of oven-dried quartz wool (**1**, 8.7 mg; **2**, 13.3 mg; **3a-c**, 9.7 mg, 4.4 mg, and 6.0 mg, respectively) (Hereaus, semiconductor grade). The samples were compressed into a pellet by squeezing them between two quartz rods. The quartz rods were removed, and the ends of the tube were capped by inserting them into septa for 7 mm tubing. The capped tube was removed from the glovebox and decontaminated. The center of the tube was wrapped with a Kimwipe, saturated with liquid nitrogen, and

sealed with a propane/oxygen or hydrogen/oxygen torch. Sample **2** was additionally contained in a He-filled, 3.5 mm polypropylene straw and heat sealed on both ends. Variable temperature magnetization data were recorded at 0.1 T, 0.5 T, 1 T, (**1-3**) and 2 T (**2**) using a Quantum Designs MPMS SQUID magnetometer. Variable temperature magnetization was corrected for the diamagnetism of the quartz wool using Pascal's constants for covalent compounds, $\chi_{QW} = 3.7 \times 10^{-7}$ emu $g^{-1}$ (no correction for the diamagnetism of the quartz tube or polypropylene straw is needed as they never leave the SQUID coils). Molar susceptibility was calculated using the following equation:

$$\chi_{mol} = \frac{(\text{molecular weight})}{(\text{sample mass})}\left[\frac{(M_{meas} - M_{ferro})}{H} - \chi_{QW}\right] - \chi_{dia}$$

**Figure 1-1.** Equation used to calculate molar susceptibility.

Where $\chi_{mol}$ is the molar susceptibility, $M_{meas}$ is the measured magnetization, $M_{ferro}$ is the ferromagnetic magnetization of the ferromagnetic impurity, which is temperature independent; its field dependence, f, is 1 at fields greater than 0.2 T and is 0.64 at 0.1 T, $\chi_{QW}$ is the contribution to the susceptibility due to the quartz wool, $\chi_{dia}$ is the diamagnetic correction of the ligands, uranium and neptunium using Pascal's constants, and H is the applied field. Two ferromagnetic impurities are commonly encountered in laboratory samples, steel or iron metal and magnetite or other ferrites from oxide coating on stainless steel lab equipment. Of these, magnetite is far more likely to be encountered. In general, the magnetization of ferromagnets is temperature independent below the Curie temperature, which is 860 K for magnetite, so magnetization of the impurity is temperature independent for this experiment. The magnetization of magnetite reaches saturation at approximately 0.2 T, above which the magnetization is ~90 emu/g.[35] Below

this field, the magnetization of magnetite is roughly linear with applied field. Based on the assumption that the impurity is magnetite or a related ferrite resulting from the abrasion of stainless-steel lab equipment, the data were corrected for a temperature and field independent ferromagnetic impurity. $M_{ferro}$ was allowed to vary to minimize the least squares difference between $\chi_{mol}$ at different fields, which produced a saturation of magnetization of $M_{ferro} = 4.61x10^{-5}$ emu (~0.43 μg of magnetite) for **1**, $M_{ferro} = 3.64x10^{-5}$ emu (~0.31 μg of magnetite) for **2**, $M_{ferro} = 3.8x10^{-5}$ emu (~0.35 μg of magnetite) for **3a**, $M_{ferro} = 8.8x10^{-6}$ emu (~0.08 μg of magnetite) for **3b**, and $M_{ferro} = 3.3x10^{-5}$ emu (~0.31 μg of magnetite) for **3c**. Variable field magnetization of **2** was collected at 2 K and 3 K from -4 T to 4 T then back to -4 T to determine whether the sample displayed hysteresis. The raw, variable temperature susceptibility data for **1** and **3a-c** are shown in Figure 1-2 and Figure 1-4. The susceptibility of **3** was repeated using three independently prepared samples. Information about the samples of **3** is given in Table 1-3 along with the results. The discrepancy between the data at different fields is consistent with the presence of a ferromagnetic impurity, typically magnetite or other ferrites from the surface of stainless-steel laboratory equipment as noted above. The data were corrected for the presence of a ferromagnetic impurity. After correction for the ferromagnetic impurities of **1** and **3**, the data obtained at 0.5 T and 1.0 T are in good agreement, Figure 1-7, but the data at 0.1 T were in poor agreement for **3**. In addition, the 0.1 T data has high uncertainty largely due to the small signal at this field. Consequently, only the 0.5 T and 1.0 T data were used. The raw, variable temperature susceptibility data for **2** was also consistent with a ferromagnetic impurity, Figure 1-3. The data were corrected for the presence of the impurity and after correction, the data obtained are in good agreement, Figure 1-9.

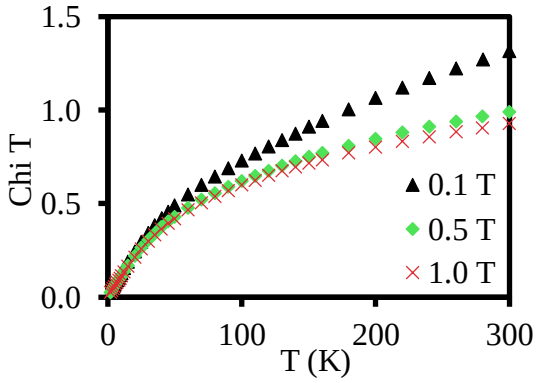


**Figure 1-2.** Variable temperature magnetic susceptibility of **1** without ferromagnetic correction.

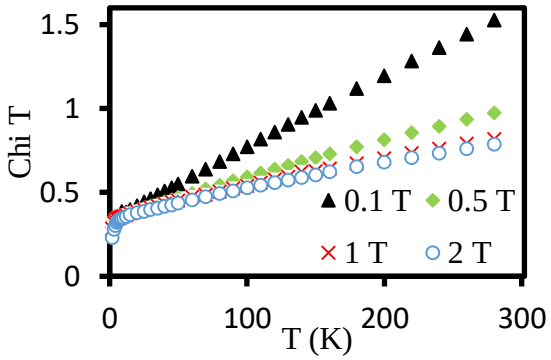


**Figure 1-3.** Variable temperature magnetic susceptibility of **2** without ferromagnetic correction.

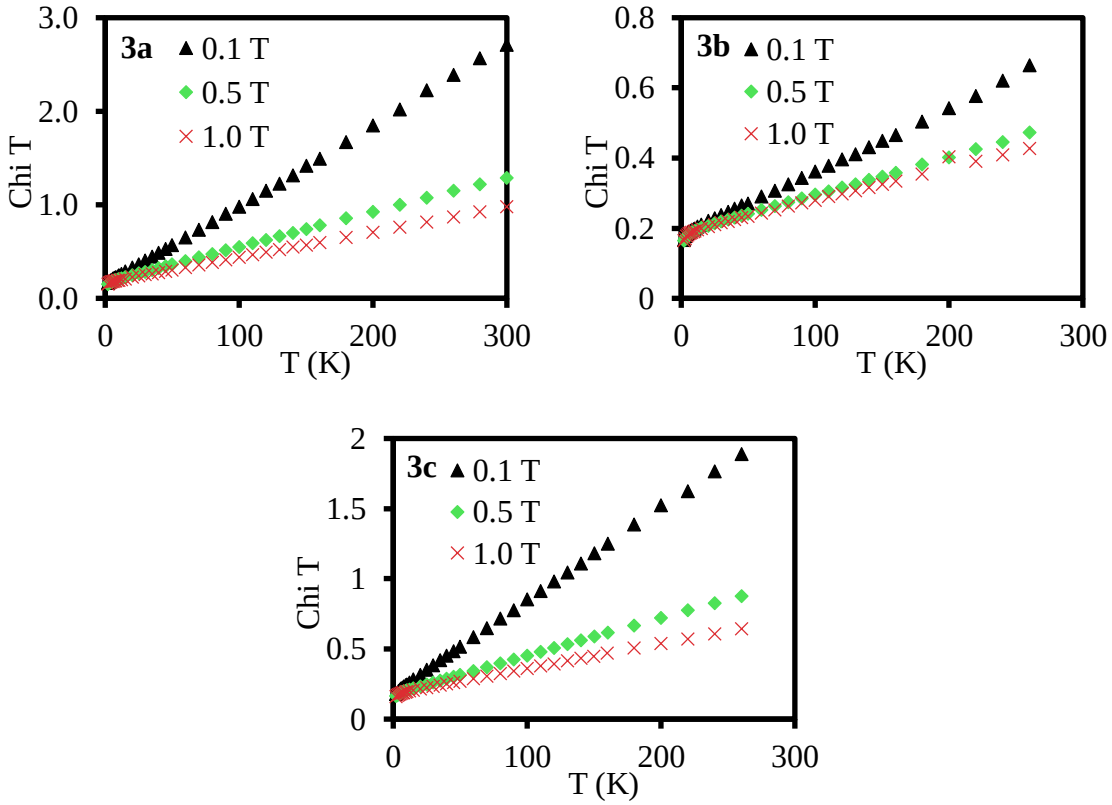


**Figure 1-4.** Variable temperature magnetic susceptibility of **3a-c** without ferromagnetic correction.

**Table 1-3.** Magnetic Susceptibility results for **3**

| | Sample **A** | Sample **B** | Sample **C** |
|---|---|---|---|
| Mass (mg) | 9.6 | 16.5 | 9.8 |
| Quartz wool (mg) | 9.7 | 4.4 | 6.0 |
| $M_{Ferro}$ (emu) | $3.8\times10^{-5}$ | $8.8\times10^{-6}$ | $3.3\times10^{-5}$ |
| $m_{eff}$ per U ($m_B$)[a] | 0.82 | 0.86 | 0.86 |
| TIP (emu)[a] | $1.6\times10^{-3}$ | $7.9\times10^{-4}$ | $8.8\times10^{-4}$ |
| 2J (K)[b] | -0.8 | -1.0 | -0.9 |

a) Average of the values determined at 0.5 T and 1 T from 10 K to 300 K.

b) Determined from 2 K to 300 K at 1 T.

**EPR Experimental**

The sample was loaded inside a 5 mm PTFE NMR tube liner inside an inert atmosphere glovebox. The liner was flame sealed inside a 5 mm quartz NMR tube, which had been filled with He gas. Electron paramagnetic resonance (EPR) spectra were obtained at 3 K with a Varian E-12 spectrometer equipped with a LHe cryostat, an EIP-547 microwave frequency counter, and a Varian E-500 gaussmeter, which was calibrated using 2,2-diphenyl-1-picrylhydrazyl (DPPH, g = 2.0036). The spectrum was simulated and fit using EasySpin by matrix diagonalization.[36] The spectrum was initially fit by Monte Carlo search using axial parameters with $A_i$ constrained to equal 1820 $g_i$. Once a set of parameters were identified that crudely fit the experimental spectrum, the constraints on the fit were removed by allowing $A_i$ to vary independently of $g_i$, relaxing the g and A to rhombic, allowing the A matrix to have a different origin from the g matrix, and finally allowing A-strain in addition to normal line broadening. The experimental spectrum was

fit alternately using downhill simplex minimization and Monte Carlo searches until the fit to the experimental spectrum no longer improved. The final parameters are in Table 1-4.

**Table 1-4.** EPR fitting parameters (9.08528 GHz) using an effective S = ½ spin Hamiltonian

| | | | |
|---|---|---|---|
| g | 0.446 | 1.632 | 2.846 |
| A (MHz) | 793.3 | 3256.5 | 5136.6 |
| A-Frame (rad) | -0.112 | 0.182 | -0.365 |
| A-Strain (MHz) | 267 | 277.8 | 277.8 |
| Linewidth (mT) | 17.2 | | |

**Results and Discussion**

The salt metathesis reaction of $UCl_4$ with two equivalents of $K_2[^{Ar}OSeO^{Ar}]$ in THF resulted in an emerald green solution, Figure 1-5. The $^1H$ NMR spectrum showed paramagnetically shifted resonances between 15.2 and −10.3 ppm. X-ray quality crystals were grown from a saturated toluene solution at −20 °C. Analysis of a single crystal revealed the U(IV) complex, $U[^{Ar}OSeO^{Ar}]_2(THF)_2$, **1**, Figure 1-6. The THF molecules in complex **1** are labile, and when exposed to vacuum for extended periods of time, the unsolvated complex is observed by $^1H$ NMR spectroscopy.

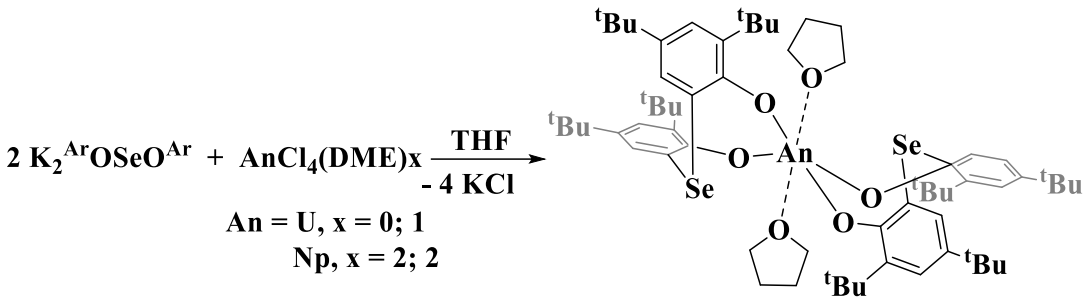


**Figure 1-5.** Reaction scheme of $AnCl_4(DME)_x$ with two equivalents of $K_2[^{Ar}OSeO^{Ar}]$ in THF.

Similar to the previously reported thorium analogue, **1** displays a highly distorted octahedral geometry where the phenolic oxygen atoms are *cis* to one another.[30] Additionally, one selenium atom is above the aromatic rings while the other is below. The $U–O_{phenoxide}$ bond distances range from 2.185(4)–2.223(4) Å and compare well with other uranium aryloxide complexes. For example, $U(O\text{-}2,6\text{-}^{t}Bu\text{-}C_6H_3)_4$[37] and $[U(salan\text{-}^{t}Bu_2)_2]$[27] have U–O bond distances of 2.135(4) Å and 2.219(2)–2.263(2) Å, respectively. The U–Se distances are 3.2606(6) and 3.1642(6) Å, which are longer than the sum of the covalent radii ($\Sigma$ = 2.86 Å)[38] suggesting no interaction exists between the selenium atom and the uranium center.

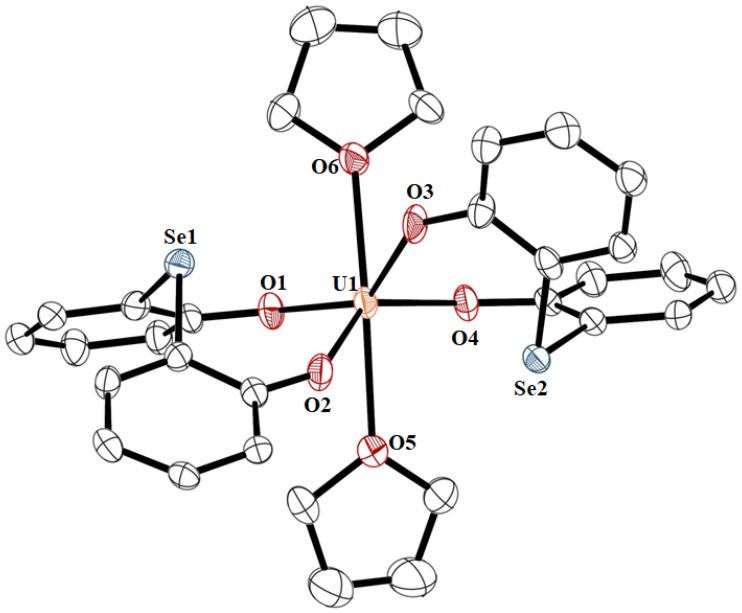


**Figure 1-6.** Thermal ellipsoid plot of **1** shown at the 50% probability level. The *tert*-butyl groups and hydrogen atoms have been omitted for clarity.

The magnetic susceptibility of **1** is typical of U(IV). The magnetic moment of the ground state can be determined from the value of $\chi T$ *vs.* $T$ extrapolated to 0 K. For **1**, $\chi T$ is zero at 0 K, so the ground state is a singlet and only displays temperature independent magnetism, which is typical for U(IV) in low symmetry. $\chi T$ is linear in $T$ to 20 K, which indicates that the first excited state is approximately 40 to 60 K (27 to 40 $cm^{-1}$) above the ground state.

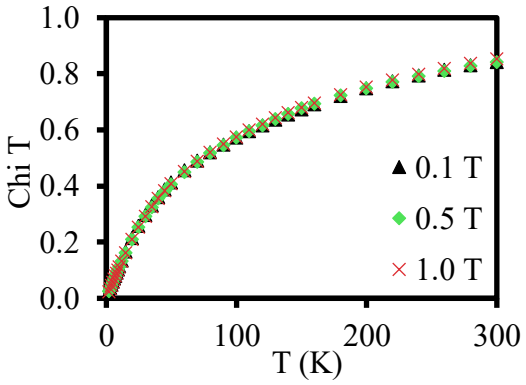


**Figure 1-7.** Variable temperature magnetic susceptibility of **1** corrected for the presence of a ferromagnetic impurity.

The nominal ground state of U(IV) is $^3H_4$ in Russell–Saunders coupling. Bonding in U(IV) is expected to be largely ionic due to the poor energy match between the metal and ligand orbitals. The Russell–Saunders ground state of U(IV), $^3H_4$, is split by the ligand field into 9 substates characterized by $m_J = 4, 3, 2, \ldots, -4$, which will be mixed by the crystal field due to the ligands. The free ion moment of $^3H_4$ when all the $m_J$ substates are equally thermally populated, is 3.6 $\mu_B$, which is considerably greater than that of **1** at room temperature, 2.5 $\mu_B$. The low value of $\mu_{eff}$ for **1** indicates that the total splitting of $^3H_4$ ground state by the crystal field is greater than $kT$ at room temperature (200 $cm^{-1}$). The synthesis of $Np[^{Ar}OSeO^{Ar}]_2(THF)_2$, **2**, as a yellow powder, was achieved using a similar route as for **1**, Figure 1-5. Crystallization from a concentrated toluene solution at −35 °C gave X-ray quality crystals, Figure 1-8. The structural characterization of **2** revealed a six-coordinate, highly distorted octahedral $Np^{4+}$ metal center nearly isomorphous with **1**. Like **1**, the selenium bis(phenolate) ligands are arranged with the phenolic oxygen atoms *cis* to one another. The $Np–O_{phenoxide}$ bonds range from 2.168(9) to 2.228(11) Å and are shorter than the Np–O bonds found in the β-diketonate $Np(FOD)_4$,

(FOD = 6,6,7,7,8,8,8-heptafluoro-2,2-dimethyl-3,5-octanedione), 2.290(7)–2.347(5) Å[39] and slightly longer than the Np–O bond distance in $(C_5H_5)_3Np(OPh)$, 2.136(7) Å.[40] The $Np–O_{phenoxide}$ bond lengths in **2** are also much shorter compared to Np(IV) glutaroimide–dioxime complexes recently reported at 2.355(2) and 2.350(2) Å and between 2.389(2)–2.405(2) Å.[41] The Np–Se distances of 3.1289(15) and 3.2287(17) Å are larger than the sum of the covalent radii of 2.87 Å[38] as observed for **1**. Despite the prevalence of actinide aryloxide complexes,[24] the only other structurally characterized neptunium alkoxide or aryloxide is $(C_5H_5)_3Np(OPh)$.

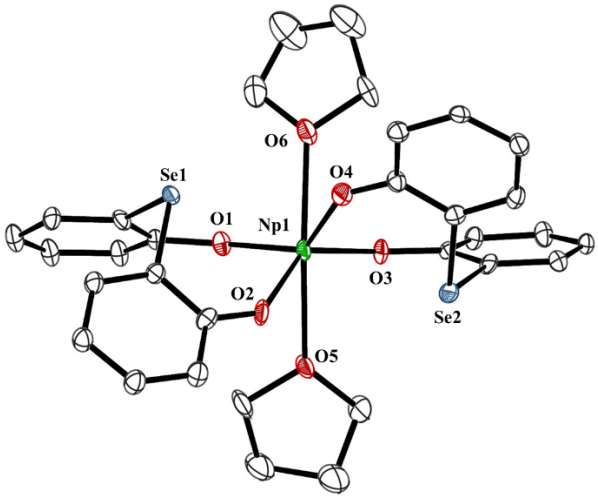


**Figure 1-8.** Thermal ellipsoid plot of one of the two independent molecules of **2** shown at the 50% probability level; the other molecular is very similar. The O2–Np–O4 angles are 81.8(4)° in each molecule. The *tert*-butyl groups, hydrogen atoms, and solvent toluene molecules have been omitted for clarity.

The magnetization of **2** decreases sharply at low temperatures, as illustrated in Figure 1-9. However, the field dependence at low temperature indicates that the decrease is due to saturation rather than coupling. The data of **2** from 25 K to 150 K at magnetic fields 0.1

T, 0.5 T, 1 T and 2 T were used to determine the magnetic susceptibility of 1.67 $\mu_B$ at 0 K. The Russell–Saunders coupling ground state of Np(IV), $^4I_{9/2}$, is split by the ligand field into 10 substates characterized by $m_J$ = 9/2, 7/2, 5/2,…,−9/2, which will be mixed by the crystal field due to the ligands. Once the ligand field is considered, the $^4I_{9/2}$ state will split into 5 Kramers doublets. In **2**, the first energy of the first excited doublet state is approximately 200–300 $cm^{-1}$ above the ground state as determined from the temperature at which the plot of $\chi T$ *vs.* $T$ deviates from linearity. Interestingly, the first excited state in the Np(IV) compound is much higher in energy than the first excited state in U(IV).

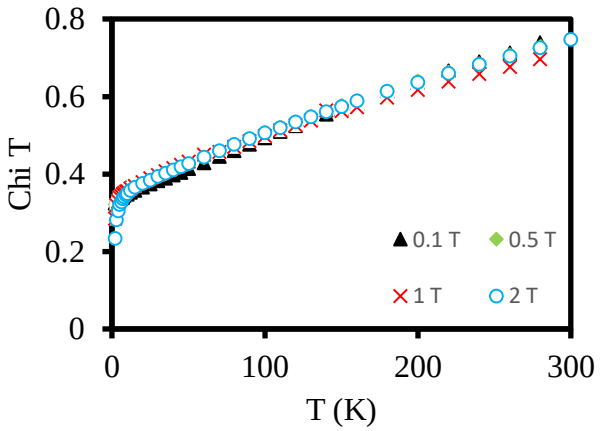


**Figure 1-9.** Variable temperature magnetic susceptibility of **2** from 10 K to 300 K.

Although Np(IV) complexes have the potential to exhibit single molecule magnet behavior,[42,43] **2** does not display a hysteresis in the magnetization *vs.* field measurements at 2 K, Figure 1-10.

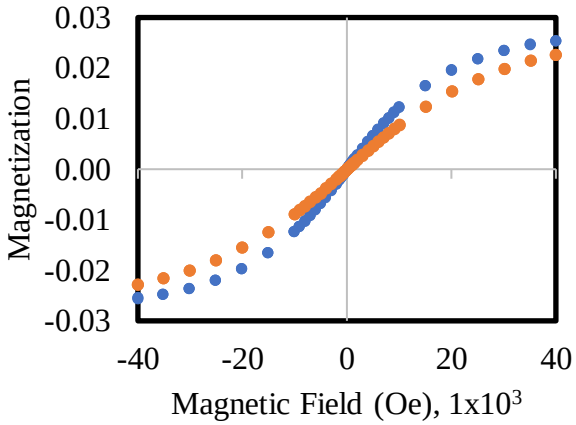


**Figure 1-10.** Variable field magnetization of **2** at 2 K (blue) and 3 K (orange) illustrating a lack of hysteresis. Data were obtained as a full hysteresis curve from -4 T to 4 T and back to -4 T.

The EPR spectrum of **2** is shown in Figure 1-11 along with a spectrum simulated using EasySpin[36] and the parameters given in Table 1-4. The sharp feature at 300 mT ($g$ = 2) is due to a minor contribution from organic radical impurities. The simulated spectrum is in general agreement with the experimental spectrum. The largest discrepancy is the position of the two peaks at ~175 mT and ~190 mT. In addition, the linewidths of the features above 400 mT are too narrow in the simulation. Given these differences, it is possible that the simulation represents a local minimum rather than the best fit; however, the largest $g$ and $A$ values, 2.85 and 5134 MHz must be close to the correct values due to the position of the low field peaks. The $g$-values are related to $\mu_{eff}$ of the ground state by $4\mu_{eff}^2 = g_1^2 + g_2^2 + g_3^3$ for effective spin = 1/2. In **2**, the EPR spectrum is consistent with a ground state magnetic moment of 1.65 $\mu_B$, which is in excellent agreement with the value determined by magnetic susceptibility, 1.67 $\mu_B$.

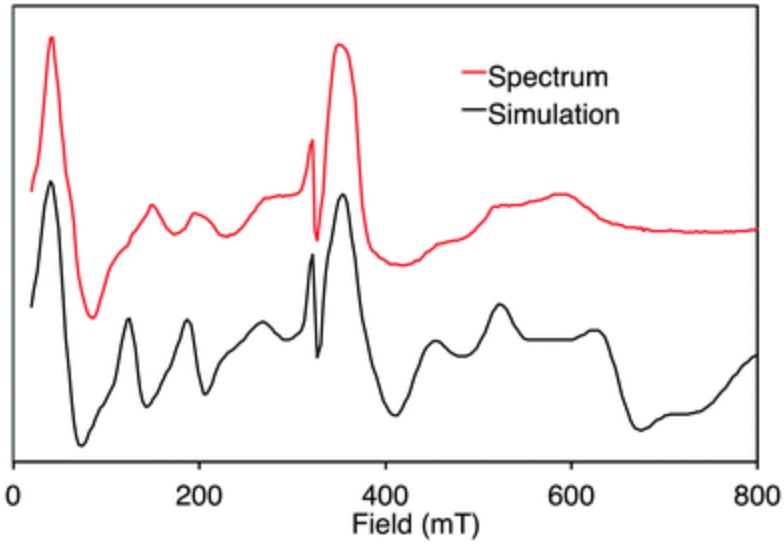


**Figure 1-11.** EPR spectrum and simulation for **2**. The 300 mT ($g$ = 2) signal has 0.04% of the intensity of the Np-237 signal.

While Np(IV) is generally EPR active, EPR studies of Np(IV) compounds are rare.[44–53] The paucity of EPR studies is due in part to the very strong hyperfine coupling between the unpaired electron and the large nuclear moment of Np. Accurate determination of the spin Hamiltonian parameters $g$ and $A$ from the fields of spin transitions requires use of the Breit–Rabi formula.[47] For simulation of the spectrum, diagonalization of the full spin Hamiltonian is required, which was accomplished here using EasySpin.[36] As noted by Poirot *et al.*,[45] the values of $A_i/g_i$ are relatively constant for Np(IV) and vary from 1807 MHz to 1869 MHz. In **2**, these values are 1779 MHz, 1995 MHz, and 1805 MHz. The first and last are in the range expected for Np(IV) although the value of 1995 MHz is slightly greater than expected. The discrepancy likely indicates the uncertainty in the $g$ and $A$ values for this component, 1.632 and 3256.5 MHz, respectively. Attempting to change either $g$ or $A$ for this component resulted in a much poorer simulation of the experimental spectrum. While the $g$-values can reveal details of the electronic structures

of Np complexes,[45,46,47,50,53–55] this typically requires at least axial symmetry for meaningful discussion. The low symmetry of the Np(IV) site in **2** precludes such an analysis.

Inspired by the use of *p*-benzoquinone to oxidize Ce(III) to Ce(IV),[56,57] as well as uranium bridging quinone structures,[58] the reaction of **1** with 0.5 equivalents of *p*-benzoquinone was examined. It resulted in a color change from green to black. The $^{1}$H NMR spectrum showed four resonances ranging from 9.73–1.25 ppm. Black, X-ray quality crystals were grown from a concentrated solution of toluene to reveal the structure as $\{U[^{Ar}OSeO^{Ar}]_2(THF)\}_2(\mu_2\text{-}OC_6H_4O)$, **3**, Figure 1-13. The structure of **3** has the same coordination as **1** except for the addition of the bridging benzoquinone and loss of one THF molecule. To confirm the uranium oxidation state, electronic absorption spectroscopy was employed. A weak, sharp f–f transition was observed at 1488 nm ($\varepsilon$ = 136.6 $M^{-1}$ $cm^{-1}$) indicative of U(V), Figure 1-12.

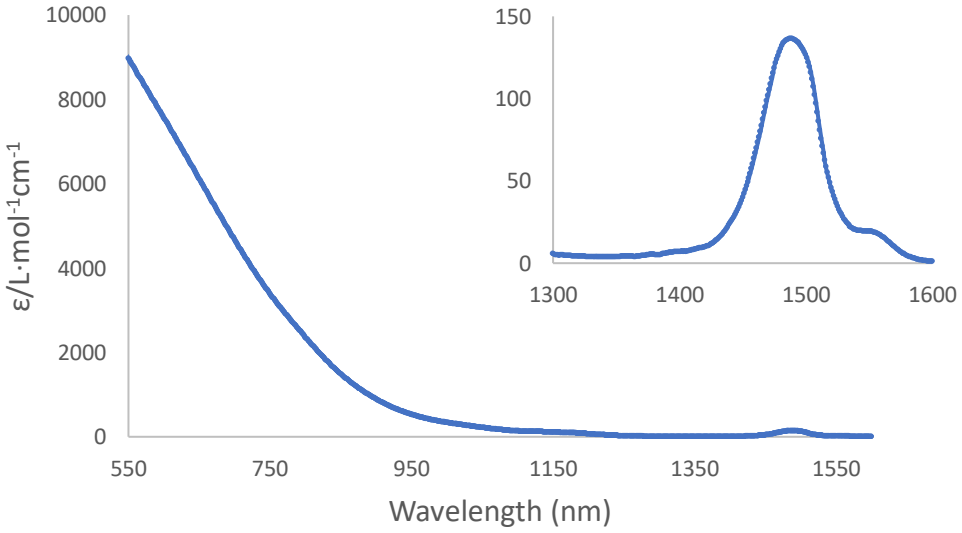


**Figure 1-12.** Electronic absorption spectra of **3** in toluene with NIR region of interest in the inset.

The U–$O_{phenoxide}$ bond distances of **1**, 2.185(4)–2.223(4) Å, contract upon oxidation to **3**, 2.163(3)–2.140(3) Å. The U–$O_{phenoxide}$ distances in **3** are longer than the 2.02–2.03(1) Å found for the terminal U–O$^i$Pr distances in the U(V/V) dimer, $U_2(O^iPr)_{10}$, and shorter than the 2.28–2.29(1) Å of the bridging U–O$^i$Pr bonds.[59] These distances are similar to those of U(V) aryloxide, $[U(O^tBu)_6]^{1-}$, 2.05(1)–2.24(1) Å.[60]

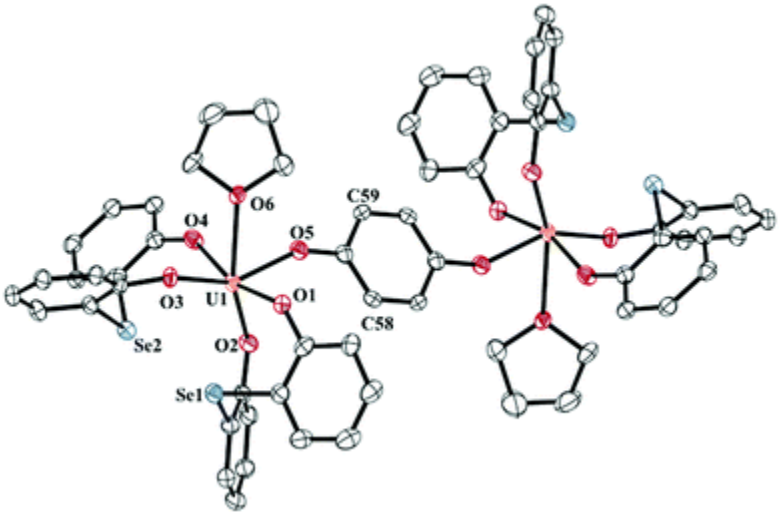


**Figure 1-13**. Thermal ellipsoid plot of **3** shown at the 50% probability level. The *tert*-butyl groups and hydrogen atoms have been omitted for clarity. The ($\mu^2$-$OC_6H_4O$) moiety lies about an inversion center.

The magnetic susceptibility of **3** is surprising. As illustrated in Figure 1-14, $\chi T$ is linear from 10 K to 300 K, which indicates that only a single state is occupied or that multiple states are occupied, but their splitting is very small, <2 K (1.2 $cm^{-1}$).

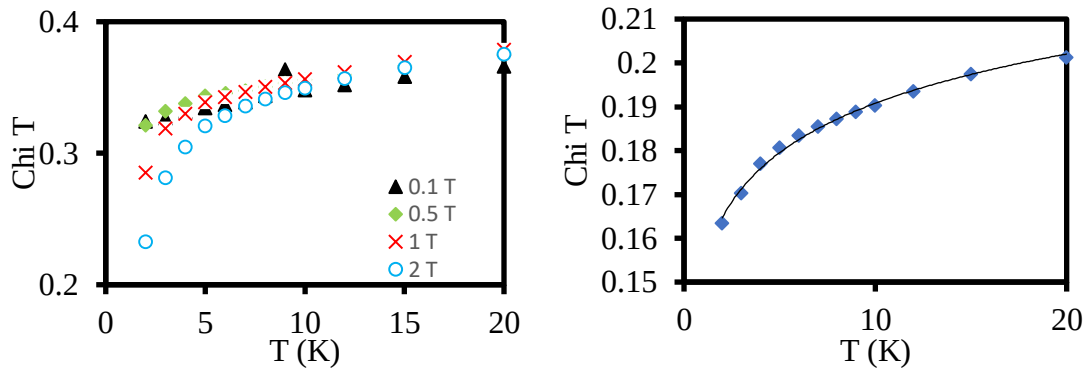


**Figure 1-14.** Variable temperature magnetic susceptibility of **2** from 2 K to 20 K (left) and **3b** at 1 T from 2 K to 20 K (right).

Bonding in U(V) is expected to be more covalent than in U(IV) due to a better energy match between the metal and ligand orbitals; consequently, the ligand field in **3** expected to be strong relative to **1**. The ground state of U(V) is $^2F_{5/2}$, which consists of 6 substates with $m_J = -5/2, -3/2, \ldots, 5/2$. The ligand field will mix with these substates based on the site symmetry of the U ion. In this case, the uranium center has low symmetry, and the $^2F_{5/2}$ state will split into 3 Kramers doublets. The magnetic moment of each Kramer's doublet is directly related to $m_J$ as shown in Table 1-5.

**Table 1-5.** Spectroscopic splitting factors and magnetic moments of $^2F_{5/2}$ substates.

| $m_J$ | $g_{\parallel}$ | $g_{\perp}$ | $\mu_{eff}$ ($\mu_B$) |
|---|---|---|---|
| 1/2 | 0.86 | 2.57 | 1.87 |
| 3/2 | 2.57 | 0.00 | 1.29 |
| 5/2 | 4.29 | 0.00 | 2.14 |

The measured ground state moment of **3** is ~0.85 $\mu_B$ per U center, which is not in agreement with any of the "pure" $m_J$ states. Given the low symmetry at the U center and the fact that the relatively strong crystal field of U(V) will strongly mix the $m_J$ states, this result is not particularly surprising.

The most interesting aspect of the magnetic susceptibility of **3** is that only a single crystal field state is significantly occupied below 300 K, which is unusual for an actinide or lanthanide complex. In addition, the unpaired electrons on the two uranium centers are weakly exchange-coupled with $2J = -0.9$ K/$k_B$ ($-0.6$ cm$^{-1}$).[61–63] This could be the reason why **3** was found to be EPR silent. The U1–O5–C57(quat) bond angle is 151.3(2)° deviates greatly from linearity, so this weak coupling is not surprising.

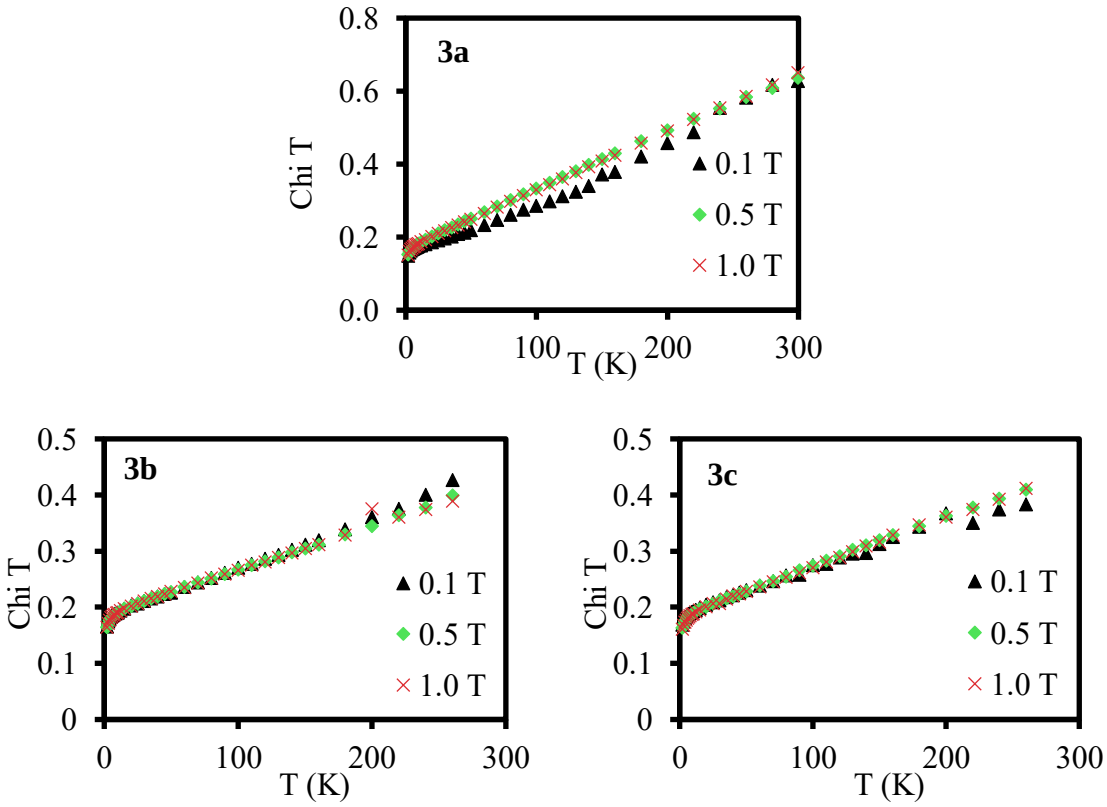


**Figure 1-15.** Variable temperature magnetic susceptibility of **3a** (top right), **3b** (bottom left) and **3c** (bottom right) corrected for the presence of a ferromagnetic impurity.

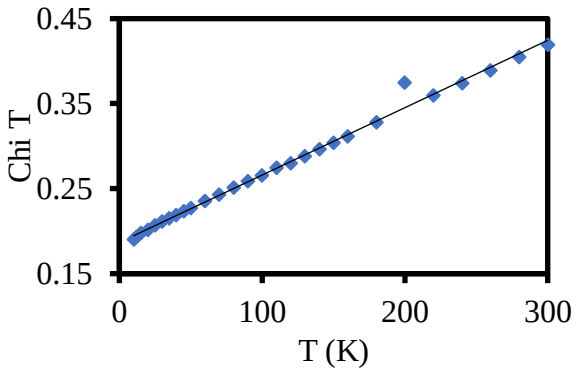


**Figure 1-16.** Variable temperature magnetic susceptibility of **3** at 1T from 10 K to 300 K.

When the reaction of **2** with *p*-benzoquinone was attempted, no change was observed. The standard reduction potentials of *p*-benzoquinone, $UO_2^+$ and $NpO_2^+$ are 0.7 V, 0.45 V and 0.60 V, respectively.[64] Since Np(IV) is more difficult to oxidize than is U(IV), the potentials of *p*-benzoquinone and Np(V) are similar, and Np(V) aryloxide have been reported as being unstable,[29] this reaction between **2** and *p*-benzoquinone is not favorable.

**Conclusion**

The synthesis and spectroscopic characterization of U(IV) and Np(IV) aryloxides as well as their magnetism has been accomplished. This is the first Np(IV) EPR spectrum reported since 2004, and only the second Np(IV) aryloxide complex structure published to date. The reactivity of these complexes with *p*-benzoquinone has been studied. The U(IV) complex affords a rare dinuclear U(V)–U(V) compound, while the Np(IV) complex does not react. Overall, this represents a rare comparison of the reactivity of uranium and an element to the right of it in the periodic table.

## Chapter 2: U(III) and Th(IV) Alkyl Complexes as Potential Starting Materials †

† This chapter is based on a manuscript that was submitted to and accepted by Chemical Communications and can be cited as: Behrle, A. C.; **Myers, A. J. (co-first author)**; Rungthanaphatsophon, P.; Lukens, W. W.; Barnes, C. L.; Walensky, J. R. U(III) and Th(IV) Alkyl Complexes as Potential Starting Materials, *Chem. Commun.* **2016**, *52*, 14373.

### Introduction

During the Manhattan project, actinide alkyl complexes were desirable for their potential as volatile compounds for separations, especially uranium enrichment.[65] More recently, organoactinide chemistry has experienced increased attention as exemplified by the Hayton and Bart groups. For example, Hayton has reported homoleptic U(IV),[66] U(V), and U(VI) alkyl[67] complexes as well as Th(IV) alkyl[65] and aryl[68] complexes, while Bart has produced a series of U(IV) benzyl compounds.[69,70] Nevertheless, Th(IV) and U(III) alkyl complexes[71–75] remain scarce.

Recently, the Hayton group has used the lithium salt of dimethylbenzylamine (DMBA) to synthesize Th(IV) and U(IV) complexes.[76,77] The lithiation of dimethylbenzylamine produces an ortho-metalated phenyl anion. This salt may be converted to the benzyl anion by reaction with potassium *tert*-butoxide,[78,30] which is accompanied by a proton migration from the alpha-position of the benzyl methylene to the *ortho*-position of the phenyl. The only known complexes using this ligand transfer agent as a starting material are a zirconium complex[79] as well as most of the lanthanide series.[30] Since the Ln(III) complexes are stabilized by this ligand, we surmised that U(III) would be stabilized in a similar fashion.

**General considerations.**

The syntheses and manipulations described below were conducted using standard Schlenk and glovebox techniques. All reactions were conducted in a Vacuum Atmospheres inert atmosphere ($N_2$) glovebox or a double-manifold Schlenk line. Anhydrous toluene, 1,2-dimethoxyethane, tetrahydrofuran, diethyl ether and hexanes were purchased, stored over activated 4 Å molecular sieves, and sparged with nitrogen prior to use. All available reactants were purchased from suppliers and used without further purification. $[ThCl_4(DME)_2]$,[80] $[UI_3(THF)_4]$,[81,82] $K[Me_2NC(H)C_6H_5]$,[83] and $(Et_2O)_2Li[CS_2(2,6\text{-}(Mes)_2C_6H_3)]$ (Mes = 1,3,5-trimethylbenzene),[84] were synthesized following the previously published procedures. Benzene-$d_6$ and toluene-$d_8$ (Cambridge Isotope Laboratories) were dried over molecular sieves and degassed with three freeze-evacuate-thaw cycles. All $^1H$ and $^{13}C$ NMR spectra were obtained on a 300, 500 or 600 MHz DRX Bruker spectrometer. $^1H$ NMR shifts given were referenced internally to the residual solvent peaks at δ 7.16 ppm ($C_6D_5H$) and 2.08 ppm ($C_7D_7H$). $^{13}C$ NMR shifts given were referenced internally to the residual peak at δ 128.0 ppm ($C_6D_6$) and 138.0 ppm ($C_7D_8$). Infrared spectra were recorded as KBr pellets on a Perkin-Elmer Spectrum One FT-IR spectrometer. Elemental analyses were performed at the University of California, Berkeley Microanalytical Facility using a Perkin-Elmer Series II 2400 CHNS analyzer.

**Synthesis of MesterphCS$_2$H**. A 50 mL Schlenk flask was charged with $(Et_2O)_2Li[CS_2(2,6\text{-}(Mes)_2C_6H_3)]$ (600 mg, 1.10 mmol) and 20 mL of $Et_2O$. 4 M HCl in dioxane (0.3 mL) was added dropwise via syringe to a stirred solution of $(Et_2O)_2Li[CS_2(2,6\text{-}(Mes)_2C_6H_3)]$ at 0 °C. The resulting cloudy red solution was allowed

to warm to room temperature and stirred overnight. The volatiles were removed under vacuum and the solid washed with hexanes and extracted with toluene. The cloudy red solution was filtered through Celite and dried under vacuum to obtain Mesterph$CS_2H$ as a pink crystalline powder (260 mg, 51%). $^1$H NMR ($C_6D_6$): δ 7.07 (t, 1H, $^3J_{H-H}$ = 7.8 Hz, p-$C_6H_3$), 6.89 (d, 2H, $^3J_{H-H}$ = 7.8 Hz, m-$C_6H_3$), 6.83 (s, 4H, m-Mes), 5.61 (s, 1H, $CS_2$*H*), 2.21 (s, 12H, o-Mes), 2.16 (s, 6H, p-Mes). $^{13}C\{^1H\}$ NMR ($C_6D_6$, 298K): 229.2, 145.4, 138.2, 137.2, 137.0, 136.6, 129.6, 129.3, 128.5, 21.5, 21.2. IR (KBr, cm-1): 3046 (w), 2969 (w), 2941 (w), 2911 (m), 2852 (w), 2501 (vs, v(S-H)), 1611 (m), 1569 (w), 1449 (m), 1374 (m), 1266 (w), 1243 (w), 1184 (w), 1101 (s), 1056 (s), 934 (s), 851 (s), 783 (w), 751 (vs), 688 (m), 617 (w), 585 (w). Anal. Calcd for $C_{25}H_{26}S_2$: C, 76.87; H, 6.71; S, 16.47. Found: C, 76.66; H, 6.63; S, 16.08.

**Synthesis of U[$\eta^4$-$Me_2NC(H)C_6H_5]_3$, 1**. A 20 mL scintillation vial was charged with $UI_3(THF)_4$ (363 mg, 0.4 mmol), diethyl ether (10 mL) and placed in a −25ºC freezer for 30 minutes. A second 20 mL scintillation vial was charged with K[$Me_2NC(H)C_6H_5$] (215 mg, 1.2 mmol) and added as a solid to the $UI_3(THF)_4$ mixture. The reaction was allowed to stir for three hours at room temperature and the solvent was removed under vacuum to yield a black solid. The solid was extracted with toluene (2 x 10 mL), filtered over Celite, concentrated and placed in a −25°C freezer for 48 h. The product was recovered as a black crystalline material (197 mg, 77%). X-ray quality crystals were grown from a concentrated toluene solution at −25°C. $^1$H NMR ($C_7D_8$, −78°C): δ 46.86 (s, 9H, N(C$H_3$)$_2$), 39.65 (s, 3H, Ar*H*), 24.50 (s, 3H, Ar*H*), −9.39(s, 3H, Ar*H*), −44.24(s, 3H, Ar*H*), −53.39 (s, 3H, Ar*H*), −71.63(s, 9H, N(C$H_3$)$_2$), −94.42(s, 3H, C*H*). IR (KBr, $cm^{-1}$): 3034 (m), 2959 (m), 2855

8(s), 2773 (s), 1912 (w), 1785 (w), 1696 (w), 1654 (w), 1588 (s), 1525 (m), 1462 (s), 1326 (m),1220 (m), 1164 (s), 1028 (s), 968 (m), 851 (m), 734 (s), 634 (m). UV-vis (0.5 mM, C7H8): 401 nm ($\varepsilon$ = 5600 $M^{-1}cm^{-1}$). Anal. Calcd for $C_{27}H_{36}N_3U$: C, 50.62; H, 5.66; N, 6.65. Found: C, 50.51; H, 5.42; N, 6.56.

**Synthesis of Th[$\eta^4$-$Me_2NC(H)C_6H_5$]$_2$[$\eta^5$-$(CH_2)MeNC(H)C_6H_5$], 2**. An oven dried 100 mL Schlenk flask was charged with $ThCl_4(DME)_2$ (639 mg, 1.2 mmol) and 20 mL oftetrahydrofuran and cooled to −78°C. An oven dried 250 mL Schlenk flask was charged with $K[Me_2NC(H)C_6H_5]$ (799 mg, 4.6 mmol) and cooled to −78 °C. The solution of $ThCl_4(DME)_2$ was added to $K[Me_2NC(H)C_6H_5]$ by cannula and stirred for 2.5 h at 0 °C. The volatiles were removed *in vacuo*, extracted with 30 mL of toluene and filtered through Celite. X-ray quality crystals were grown at −25°C from a concentrated toluene solution. Yield: 620 mg, 73%. $^1$H NMR ($C_7D_8$, -78 °C): δ 7.36 (d, J = 6.3 Hz, 1H, Ar*H*), 7.10 (br s, 1H, Ar*H*), 6.98 (br s, 1H, Ar*H*), 6.90-6.84 (m, 2H, Ar*H*), 6.80-6.73 (m, 2H, Ar*H*), 6.54-6.49 (m, 2H, Ar*H*), 6.46-6.38 (m, 2H, Ar*H*), 6.27 (d, J = 7.8 Hz, 1H, Ar*H*), 3.83 (s, 1H, C*H*), 3.59 (d, J = 6.3 Hz, 1H, o-*H*), 3.17 (d, J = 5.7 Hz, 1H, o-*H*), 3.21 (s, 1H, C*H*), 3.18 (s, 1H, C*H*), 2.98 (d, J = 6.3 Hz, 1H, o-*H*), 2.43 (s, 3H, C$H_3$), 2.19 (s, 6H, N(C$H_3$)$_2$), 1.94 (s, 2H, C$H_2$), 1.92 (s, 3H, C$H_3$), 1.70 (s, 3H, C$H_3$). $^{13}$C{$^1$H} ($C_7D_8$, -78 °C): δ 138.95, 138.61, 136.89, 135.31, 131.09, 130.40, 129.85, 128.92, 127.38, 124.44, 121.08, 120.77, 120.52, 114.24, 113.51, 108.76, 98.72, 98.27, 91.78, 90.84, 90.43, 72.08, 44.02, 43.41, 41.65, 40.29, 40.01. IR (KBr, $cm^{-1}$): 3035 (m), 2959 (m), 2910 (m), 2863 (m), 2785 (m), 1599 (m), 1531 (m), 1479 (s), 1449 (m), 1332 (m), 1306 (m), 1259 (m), 1205 (m), 1171 (m), 1075 (m), 1028 (m), 1012 (m), 977 (m), 859 (m), 811 (m), 743 (s),

708 (m), 666 (m). Anal. Calcd for $C_{27}H_{35}N_3Th$: C, 51.18; H, 5.57; N, 6.63. Found: C, 51.10; H, 5.53; N, 6.61.

**Synthesis of U[$S_2C(2,6-Mes_2C_6H_3)]_4$(THF), 3**. A 20 mL scintillation vial was charged with **1** (126 mg, 0.20 mmol) and 5 mL THF. A second 20 mL scintillation vial was charged with Mesterph$CS_2H$ (237 mg, 0.61 mmol) and 5 mL of THF. The solutions were combined and stirred for 48 h. The brown suspension was centrifuged and the pellet washed with pentane (2 x 2 mL). The pellet was extracted with toluene, filtered through Celite and volatiles removed *in vacuo* resulting in a dark red solid (64 mg, 17%). X-ray quality crystals were grown from a concentrated toluene solution layered with pentane at −25°C. $^1$H NMR ($C_6D_6$): δ 6.83 (br s, 16H, m-$C_6H_3$), 6.76 (t, 4H, $^3J_{H-H}$ = 7.2 Hz, p-$C_6H_3$), 6.33 (d, 8H, $^3J_{H-H}$ = 7.2 Hz, m-$C_6H_3$), 6.87 (s, 8H, m-Mes), 2.55 (s, 24H, p-$CH_3$). Due to the paramagnetism of uranium, we were unable to unambiguously identify the o-$CH_3$ and THF chemical shifts. IR (KBr, $cm^{-1}$): 2950 (s), 2917 (s), 2856 (m), 1612 (m), 1568 (w), 1484 (w), 1450 (s), 1376 (m), 1208 (m), 1185 (w), 1101 (m), 1011 (s), 998 (s), 936 (w), 918 (m), 848 (s), 808 (m), 779 (w), 760 (m), 742 (m), 698 (w), 585 (w). Anal. Calcd for $C_{104}H_{108}OS_8U$: C, 66.86; H, 5.61. Found: C, 66.53; H, 5.35.

**Synthesis of Th[$S_2C(2,6-Mes_2C_6H_3)]_4$(THF), 4**. A 20 mL scintillation vial was charged with **2** (104 mg, 0.17 mmol) and 7 mL of THF. A second 20 mL scintillation vial was charged with Mesterph$CS_2H$ (260 mg, 0.67 mmol) and 10 mL of THF. The solutions were combined and stirred for 18 hours at room temperature. The resulting orange suspension was centrifuged and the precipitate washed with pentane (2 x 2 mL). The precipitate was dried under vacuum resulting in an orange powder (159 mg, 52%). X-ray quality crystals were grown from a concentrated toluene solution at −25°C. $^1$H NMR

($C_6D_6$): δ 7.03 (t, 4H, $^3J_{H-H}$ = 7.2 Hz, p-$C_6H_3$), 6.93 (s, 8H, m-$C_6H_3$), 6.87 (s, 8H, m-Mes), 6.86 (s, 8H, m-Mes), 3.44 (s, 4H, THF), 2.45 (s, 24H, C*H*$_3$), 2.33 (s, 24H, C*H*$_3$), 2.00 (s, 24H, C*H*$_3$), 1.39 (s, 4H, THF). $^{13}C\{^1H\}$ NMR ($C_6D_6$): δ 252.11, 150.60, 139.74, 138.75, 137.66, 136.05, 135.49, 130.69, 129.22, 128.34, 127.90, 68.73, 25.80, 23.31, 22.32, 21.47. IR (KBr, $cm^{-1}$): 2964 (m), 2916 (s), 2856 (m), 1611 (m), 1572 (w), 1450 (m), 1376 (m), 1263 (m), 1207 (m), 1184 (m), 1100 (s), 1009 (vs), 916 (m), 847 (s), 807 (m), 758 (m), 742 (w), 698 (w), 583 (w), 466 (m). Anal. Calcd for $C_{104}H_{108}OS_8Th$: C, 67.07; H, 5.84. Found: C, 67.45; H, 6.05.

**Crystallographic Data Collection and Structure Determination**.

Selected single crystals were mounted on nylon cryoloops using viscous hydrocarbon oil. X-ray data collection was performed at 100(2) K. The X-ray data were collected on a Bruker CCD diffractometer with monochromated Mo-Kα radiation (λ = 0.71073 Å). The data collection and processing utilized Bruker Apex2 suite of programs.[32] The structures were solved using direct methods and refined by full-matrix least-squares methods on F2 using the Bruker SHELX-2014/7 program.[33] All non-hydrogen atoms were refined with anisotropic displacement parameters. All hydrogen atoms were placed at calculated positions and included in the refinement using a riding model. Thermal ellipsoid plots were prepared by using Olex2[34] with 50% of probability displacements for non-hydrogen atoms. Crystal data and details for data collection for complexes **1**, **2**, **3**, and **4** are also provided in Table 2-1.

**Table 2-1.** X-ray crystallography data is shown for complexes **1**, **2**, **3**, and **4**.

| | **1** | **2** | **3** | **4** |
|---|---|---|---|---|
| CCDC deposit number | 1507960 | 1507961 | 1507963 | 1507962 |
| Empirical formula | $C_{27}H_{36}N_3U$ | $C_{27}H_{35}N_3Th$ | $C_{104}H_{108}OS_8U$ | $C_{104}H_{108}OS_8Th$ |
| Formula weight (g/mol) | 640.63 | 633.62 | 1868.51 | 1862.52 |
| Crystal habit, color | Prism, black | Prism, yellow | Prism, red | Prism, orange |
| Temperature (K) | 100(2) | 100(2) | 100(2) | 100(2) |
| Space group | $P2_1/c$ | $P$ -1 | $P2_1/c$ | $P2_1/c$ |
| Crystal system | Monoclinic | Triclinic | Monoclinic | Monoclinic |
| Volume ($Å^3$) | 2469.6(6) | 1211.2(4) | 10248.6(14) | 10384.7(16) |
| *a* (Å) | 14.318(2) | 9.590(2) | 15.0040(12) | 15.0263(13) |
| *b* (Å) | 11.5400(17) | 11.143(2) | 25.0884(19) | 25.217(2) |

| | | | | |
|---|---|---|---|---|
| $c$ (Å) | 14.975(2) | 11.619(2) | 27.253(2) | 27.433(2) |
| $\alpha$ (˚) | 90.00 | 88.275(2) | 90.00 | 90.00 |
| $\beta$ (˚) | 93.520(2) | 77.613(2) | 92.527(10) | 92.5570(10) |
| $\gamma$ (˚) | 90.00 | 87.316(2) | 90.00 | 90.00 |
| $Z$ | 4 | 2 | 4 | 4 |
| Calculated density ($Mg/m^3$) | 1.723 | 1.737 | 1.330 | 1.343 |
| Absorption coefficient ($mm^{-1}$) | 6.591 | 6.174 | 1.796 | 1.644 |
| Final R indices [$I > 2\sigma(I)$] | $R = 0.0233$ $R_W = 0.0496$ | $R = 0.0262$ $R_W = 0.0648$ | $R = 0.0611$ $R_W = 0.1276$ | $R = 0.0517$ $R_W = 0.1264$ |

**Magnetism Measurements.**

In an inert atmosphere glovebox, uranium complex **1** (9.1 mg) was powdered using an agate mortar and pestle, sandwiched between two plugs of quartz wool (Hereaus, 12.0 mg) within a 4 mm OD quartz tube, which was flame sealed on both ends. Variable temperature magnetization data were recorded at 0.1 T, 0.5 T, and 1 T using a Quantum Designs MPMS SQUID magnetometer. Variable temperature magnetization was corrected for the diamagnetism of the quartz wool using Pascal's constants (no correction for the diamagnetism of the quartz tube is needed as the quartz tube never leaves the

SQUID coils). Molar susceptibility was corrected for the presence of a small amount of ferromagnetic impurity ($M_{ferro}$), the diamagnetism of the quart wool ($\chi_{QW}$), ligands and uranium ($\chi_{dia}$) using Pascal's constants, and calculated using the following equation:

$$\chi_{mol} = \frac{(\text{molecular weight})}{(\text{sample mass})}\left[\frac{(M_{meas} - M_{ferro})}{H} - \chi_{QW}\right] - \chi_{dia}$$

**Figure 2-1.** Equation used to calculate molar susceptibility.

where $\chi_{mol}$ is the molar susceptibility, $M_{meas}$ is the measured magnetization, $M_{ferro}$ is the magnetization of the ferromagnetic impurity, which is temperature independent and assumed to be identical at all fields, $\chi_{QW}$ is the contribution to the susceptibility due to the quartz wool, $\chi_{dia}$ is the diamagnetic correction, and H is the applied field. For **1**, this equation was applied to the 0.5 T and 1 T data to determine, $M_{ferro}$, which were $1.6\times10^{-5}$ emu and $2.92\times10^{-5}$ emu, respectively. The 0.1 T data was fit to the other data using $M_{ferro}$, 0.1 T = 0.63 $M_{ferro}$ because the 0.1 T data is below the anisotropy field of the ferromagnetic impurity (see below); the value of 0.63 was determined by fitting the 0.1 T data to the 0.5 T and 1 T data. For **1**, the amount of ferromagnetic impurity was determined using the 0.1 T, 0.5 T and 1 T data and $M_{ferro}$, 0.1 T = 0.63 $M_{ferro}$; $M_{ferro}$ = $2.7\times10^{-5}$ emu.

Two ferromagnetic impurities are commonly encountered in laboratory samples, steel or iron metal and magnetite or other ferrites from oxide coating on stainless steel lab equipment. Of these, magnetite is far more likely to be encountered. In general, the magnetization of ferromagnets is temperature independent below the Curie temperature, which is 860 K for magnetite, so magnetization of the impurity is temperature independent for this experiment. The magnetization of ferromagnets is also largely field-

independent above the anisotropy field, which is approximately 0.2 T for magnetite, above which the magnetization is ~90 emu/g.[35] Below the anisotropy field, the magnetization of a magnet is roughly linear with the applied field. Based on the assumption that the impurity is magnetite or some other ferrite resulting from the abrasion of stainless-steel lab equipment, the data were corrected for a temperature and field independent ferromagnetic impurity. $M_{ferro}$ was allowed to vary to minimize least squares difference between $\chi$mol at different fields, and produced a saturation magnetization of $M_{ferro}$ of $2.7\times10^{-5}$ emu, which corresponds to ~0.25 μg of magnetite. Variable field magnetization data were collected at 2 K, 3 K, 5 K, and 298 K from -4 T to 4 T then back to -4 T to determine whether the sample displayed hysteresis. The data at 2 K, 3 K, and 5 K and low field were used to determine the magnetic susceptibility at 0 K.

**Results and Discussion**

Reaction of $UI_3(THF)_4$ with three equivalents of $K[Me_2NC(H)C_6H_5]$ in $Et_2O$ for 3 h at −25 °C (Figure 2-2) results in a dark colored solution. X-ray quality crystals were grown from a saturated toluene solution at −25 °C, and diffraction revealed the U(III) complex, $U[\eta^4\text{-}Me_2NC(H)C_6H_5]_3$, **1** (Figure 2-3). Reaction with $UCl_4$ also produced **1** along with half an equivalent of 1,2-bis(dimethylamino)-1,2-diphenylethane. The $^1$H NMR spectrum of **1** is fluxional at room temperature but cooling to −78 °C made the spectrum assignable. The $^1$H NMR spectrum is paramagnetically shifted, and the amine methyl resonances are inequivalent at 47 ppm and −71 ppm. The methine proton is located at −94 ppm. Complex **1** is thermally unstable above room temperature but stable when stored cold in the solid-state. As mentioned previously, this compound represents a rare U(III) hydrocarbyl complex.

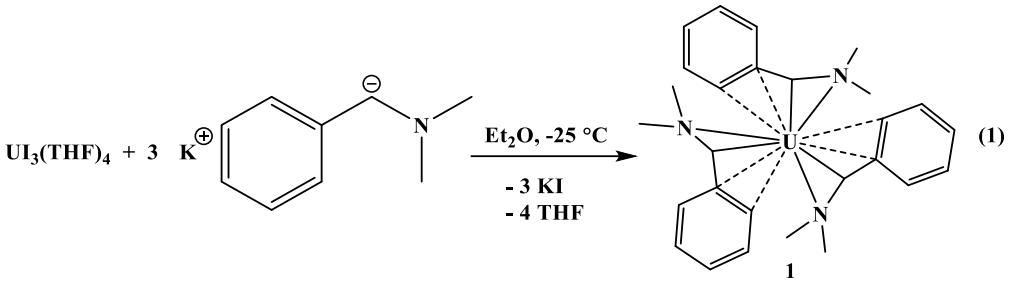


**Figure 2-2.** Reaction Scheme of $UI_3(THF)_4$ with three equivalents of $K[Me_2NC(H)C_6H_5]$ in $Et_2O$.

The $U–C_{ipso}$ distances are 2.766(3), 2.784(3), and 2.804(3) Å while the $U–C_{ortho}$ distances are 2.818(3), 2.813(3), and 2.816(3) Å. These distances are far shorter than the closest U–C interactions in $U[CH(SiMe_3)_2]_3$ but are similar to those found in $[U(dddt)_3]^{2-}$, dddt = 5,6-dihydro-1,4-dithiine-2,3-dithiolate.[85] Therefore, the best description of the coordination of the DMBA ligand to uranium is $\eta^4$-(*N*,*C*,*C*,*C*) instead of the $k^2$-(*N*,*C*) form resulting from the lithium salt. The uranium-methine carbon bond distances of 2.540(4), 2.521(4), and 2.550(3) Å are between the 2.57(2) Å observed in $Tp^*_2U(CH_2C_6H_5)$, Tp* = hydrotris(3,5-dimethylpyrazolyl)borate, and 2.48(2) Å in $U[CH(SiMe_3)_2]_3$.

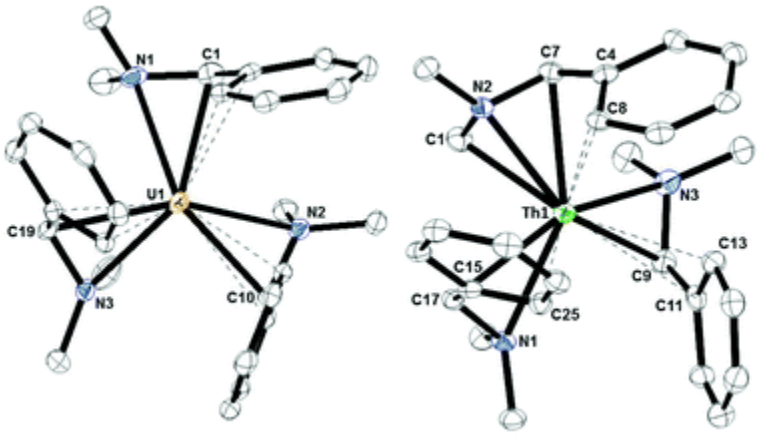


**Figure 2-3.** Thermal ellipsoid plot of **1** (left) and **2** (right) shown at the 50% probability level. The hydrogen atoms have been omitted for clarity.

The magnetization of **1** was studied by variable temperature and variable field experiments. The effective magnetic moment of **1** is shown in Figure 2-5. Under Russell–Saunders coupling, U(III) has a $^4I_{9/2}$ ground multiplet, which is split by the ligand field into substates characterized by $m_J$. The measured ground state moment of **1** is 1.11 $\mu_B$, which is in excellent agreement with that of them J = 3/2 substate (1.09 $\mu_B$). Assignment of this ground state to **1** is supported by a failure to observe an EPR spectrum at 2 K as the J = 3/2 substate is not EPR active. The first excited state of **1** is ~100 $cm^{-1}$ above the ground state as determined from the temperature at which the plot of $\chi T$ vs. T deviates from linearity. Although U(III) complexes frequently exhibit single molecule magnet (SMM) behavior,[86] **1** does not display a hysteresis in the magnetization vs. field measurements at 2 K.

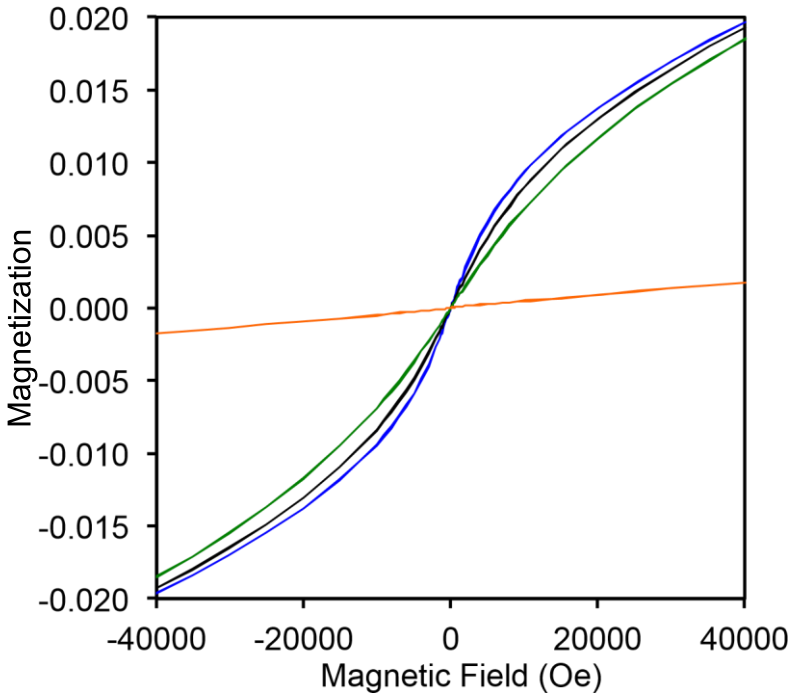


**Figure 2-4.** Variable field magnetization data at 2 K (blue), 3 K (black), 5 K (green), and 300 K (orange). Data were obtained as a full hysteresis curve from -4 T to 4 T and back to -4 T.

The lack of single molecular magnet (SSM) behavior is surprising given the ~100 $cm^{-1}$ energy of the first excited state. We believe the mechanism for relaxation is tunneling due to dipole–dipole coupling in analogy to the behavior of $U(H_2BPz_2)_3$.[87] The U–U distance in **1** is 8.0 Å, which is shorter than the 8.2 Å distance in $U(H_2BPz_2)_3$,which does not display SMM behavior, and is much shorter than that of $U(Ph_2BPz_2)_3$ (10.8 Å), which does display SMM behavior.[88]

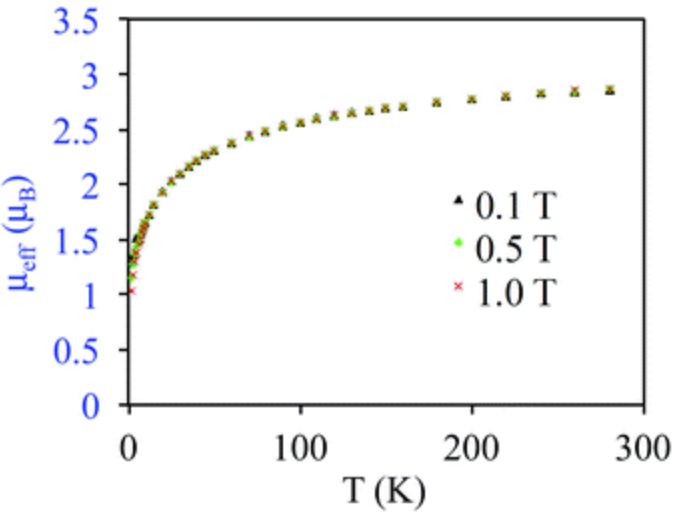


**Figure 2-5.** Variable temperature magnetic moment of **1**.

Thorium presented an interesting comparison since Th(III) is only accessible using strong reducing agents,[89] and since all previously reported compounds of the DMBA ligand needed only three ligands to saturate the coordination sphere. The reaction of $ThCl_4(DME)_2$ with four equivalents of $K[Me_2NC(H)C_6H_5]$ at -78 °C (Figure 2-6) produced an orange solution. The $^1H$ NMR spectrum revealed an asymmetric coordination environment as well as a protonated ligand. Orange crystals suitable for X-ray diffraction analysis were obtained from a saturated toluene solution at -25 °C. The structure (Figure 2-3) is similar to previous complexes with three DMBA ligands; however, one of the methyl groups has undergone C–H bond activation to afford a dianionic DMBA ligand, $Th[\eta^4\text{-}Me_2NC(H)C_6H_5]_2[\eta^5\text{-}(CH_2)MeNC(H)C_6H_5]$, **2**. Similar systems in which U(IV) yields a U(III) product and Th(IV) results in C–H bond activation have been observed previously.[90,91]

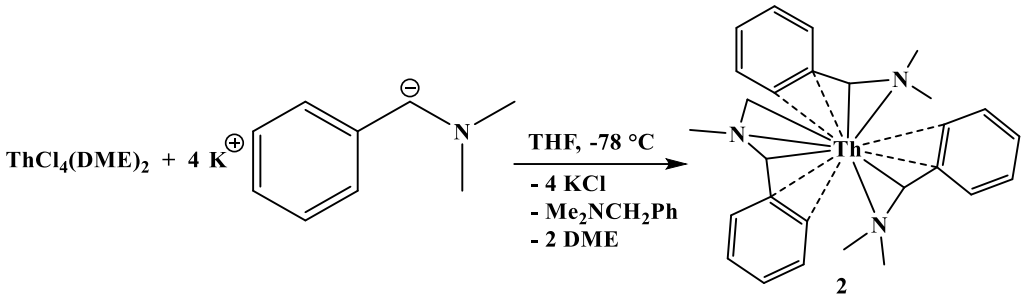


**Figure 2-6.** Reaction Scheme of $ThCl_4(DME)_2$ with four equivalents of $K[Me_2NC(H)C_6H_5]$ in THF.

The Th1–C1, Th1–N2, Th1–C7, Th1–C4, and Th1–C8 bond distances are 2.545(4), 2.453(3), 2.578(4), 2.606(3), and 2.866(3) Å, respectively, so the ligand with the C–H bond activated methyl group is a dianionic, $\eta^5$-ligand. The Th–$C_{methine}$ bond distances in **2** (2.578(4), 2.608(4), and 2.620(3) Å) are slightly longer than the Th–$C_{benzyl}$ bond length of 2.551(7) Å in $(C_5Me_5)_2Th(CH_2C_6H_5)_2$.[92] However, the Th–$C_{ipso}$ bond distances of 2.850(4), 2.908(4), and 2.851(4) Å are significantly shorter than the Th–$C_{ipso}$ bond distance of 2.979(6) Å in $(C_5Me_5)_2Th(CH_2C_6H_5)_2$, but are similar to the 2.700(8)–2.842(4) Å observed for U–$C_{ipso}$ interactions in $U(CH_2C_6H_4R)_4$, R = H, 2-*p*-$^i$Pr; 2-*p*-$^t$Bu; 2-*m*-OMe; 2-*o*-picolyl, complexes,[69] when the difference in ionic radii are taken into account.

To demonstrate the utility of **1** and **2** as potential starting materials for further substitution, both were treated with three and four equivalents of $HS_2C[2,6\text{-}(Mes)_2C_6H_3]$, Mes = 2,4,6-$Me_3C_6H_2$ (Figure 2-7). In both cases, the product is a tetravalent species, $An[S_2C(2,6\text{-}(Mes)_2C_6H_3)]_4(THF)$, An = U, **3**; Th, **4**. Both **3** and **4** were characterized by X-ray crystallography and were found to be structurally analogous (**3** is shown in Figure 2-8). Both are nine-coordinate with eight sulfur atoms and one THF molecule completing

the coordination sphere in a monocapped square antiprismatic geometry. It is surprising that both thorium(IV) and uranium(IV) are large enough to accommodate four ligands as well as a THF molecule since dithiocarbamate,[93] dithiophosphinate,[94] and dithiolene[85] actinide(IV) complexes are typically eight-coordinate. Our rationale for the presence of the THF molecule is that it may be bound to the metal center prior to or during the addition of the $[S_2C(2,6\text{-}(Mes)_2C_6H_3)]^{1-}$ ligands, and upon coordination of the dithiocarboxylate ligands, the THF is captured in the inner coordination sphere. The THF molecule cannot be removed by heat or vacuum. The space filling model of the compound is consistent with this explanation as is the observation that both complexes precipitate from the reaction mixture when the reaction is performed in THF. Another interesting feature of complexes **3** and **4** is that homoleptic sulfur-based complexes are not typically produced by protonation reactions. For example, reaction of $[\{(Me_3Si)_2N\}_2U(CH_2SiMe_2NSiMe_3)]$ with one equivalent of $2,6\text{-}Me_2C_6H_3SH$ yields $[(Me_3Si)_2N]_3U[S(2,6\text{-}Me_2C_6H_3)]$, but using four equivalents results in intractable products.[95] In our case, reaction of **1** or **2** with four equivalents of $HS_2C[2,6\text{-}(Mes)_2C_6H_3]$ produced isolable compounds. Both compounds are viable starting materials, which may be useful alternatives to the widely used $U[N(SiMe_3)_2]_3$.[96,97]

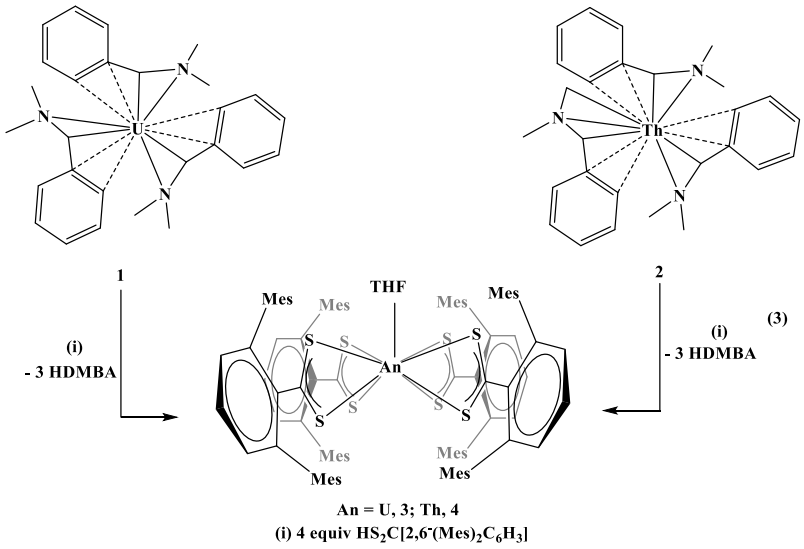


**Figure 2-7.** Reaction scheme of **1** and **2** with four equivalents of $HS_2C[2,6\text{-}(Mes)_2C_6H_3]$ in THF.

The average U–S bond distances in **3** of 2.8775(17) Å are longer than those seen in $[U(dddt)_3]$, which range from 2.717–2.760 Å. This increase is attributed to the greater steric properties of the terphenyl-based ligand. The average Th-S bond distances in **4** of 2.934(3) Å is similar to the 2.932(2) Å distance in the sterically crowded dithiophosphinate complex $Th(S_2P^tBu_2)_4$.

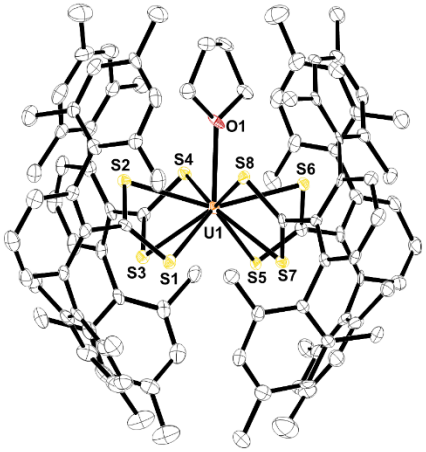


**Figure 2-8.** Thermal ellipsoid plot of **3** shown at the 50% probability level. The hydrogen atoms have been omitted for clarity.

These distances are significantly longer than the 2.9075(5) Å and 2.911(4) Å distances in the less crowded complexes $Th(S_2P^iPr_2)_4$[98] and $Th[S_2P(C_6H_{11})_2]_4$,[99] respectively. The difference in bond distances of **3** and **4** (~0.057 Å) is consistent with the Shannon radii of nine-coordinate $U^{4+}$ (1.19 Å) vs. $Th^{4+}$ (1.23 Å).[100]

**Conclusion**

In summary, using the potassium salt of dimethylbenzylamine, we have synthesized and characterized a rare U(III) hydrocarbyl complex. When the analogous reaction is attempted with a uranium(IV) starting material, ligand coupling is observed along with reduction to U(III). The thorium complex featured C–H bond activation of one of the methyl groups on the dimethylamine moiety. The synthetic utility of these complexes was evaluated using a sterically demanding dithio-carboxylate ligand, $HS_2C(C_6H_3Mes_2)$, which produced analogous products, $An[S_2C(2,6\text{-}(Mes)_2C_6H_3)]_4(THF)$, An = U; Th.

## Chapter 3: Synthesis and Utility of a Neptunium(III) Hydrocarbyl Complex†

† This chapter is based on a manuscript that was submitted to and accepted by Angewandte Chemie and can be cited as: **Myers, A. J.**; Tarlton, M. L.; Kelley, S. P.; Lukens, W. W.; Walensky, J. R. Synthesis and Utility of a Neptunium(III) Hydrocarbyl Complex, *Angew. Chem. Int. Ed.* **2019**, 58, 14891.

### Introduction

Since the synthesis of $Ni(CO)_4$[101] and ferrocene,[102] significant advances in organometallic chemistry continue to be made with respect to metal-based catalysis,[103,104] materials chemistry,[105] and biomimetic studies.[106] Historically, the Manhattan Project drove the progress of organoactinide chemistry for the potential use of actinide alkyl complexes in separation,[65] and although the focus has changed, organometallic chemistry of the actinides in particular has experienced a renaissance in the past 30 years.[107-110] This renaissance is especially true of recent advances in low-valent actinide chemistry, that is, divalent and trivalent organoactinide complexes. For example, $Th^{2+}$,[111] $U^{2+}$,[112-114] $Np^{2+}$,[11,115] and $Pu^{2+}$,[116] complexes have all been isolated, along with an organometallic americium complex, $(C_5Me_4H)_3Am$.[117] However, because of their lack of thermal stability, actinide alkyls,[118-122] especially low-valent actinides, are rare.[123-132] These complexes are of interest for their small-molecule activation,[133,134] spectroscopic and magnetic properties,[135] and as starting materials for advancing the fundamental coordination chemistry and reactivity of low valent actinides.[136] To date, the organometallic chemistry of the actinides, particularly transuranic chemistry, has been dominated by π-ligands such as cyclopentadienyl and other derivatives.[137]

The coordination chemistry of transuranic elements has lagged behind that of thorium and uranium because of the lack of easily accessible starting materials, as well as the associated cost and infrastructure required to obtain and handle these elements. Since transuranic elements are byproducts of irradiating uranium with neutrons, exploring the chemistry of these elements is necessary to better understand how to separate the minor actinides from complex matrices when recycling spent nuclear fuel. Despite its relevance in the fuel cycle, the chemistry of neptunium has been largely neglected compared to its neighboring elements, uranium and plutonium.[138]

The organometallic chemistry of neptunium has recently been thoroughly reviewed by Arnold.[139] There are only a few examples of hydrocarbyl complexes with neptunium and all of them tetravalent. For example, only one neptunium(III) alkyl complex, $Np[CH(SiMe_3)_2]_3$, has been claimed, but only characterized by a color change and IR spectroscopy as the compound decomposes rapidly in solution.[140] The reactivity of $(C_5H_5)_3NpCl$ with alkyl lithium reagents has been reported but characterized based on percent Np obtained as well as Mössbauer spectroscopy.[141] Additionally, the group of Arnold has suggested these studies warrant further investigation.[139,142] Further reactivity of $(C_5H_5)_3NpCl$ has been reported to produce alkyl species, $(C_5H_5)_3NpX$ (X= Me, Et, CCH and Ph), and characterized by UV-vis-nIR, IR, EPR spectroscopy and magnetic measurements.[143] But, to our knowledge, these studies have not been published. It should be noted that the reactivity of $(C_5H_5)_3NpCl$ with alkyl lithium reagents does form a significant amount of $(C_5H_5)_3Np^{III}$, which is not unexpected given the Np(IV/III) redox couple.[142] Recently, Gaunt and co-workers reported $NpCl_4(DME)_2$,[17] $NpCl_4(THF)_3$, and $NpCl_3(pyridine)_4$,[144] which have replaced $NpI_3(THF)_4$,[81] as a useful neptunium starting

materials since neptunium metal is required to prepare $NpI_3(THF)_4$. Here, we report the synthesis of a stable transuranic hydrocarbyl complex, $Np[\eta^4\text{-}Me_2NC(H)C_6H_5]_3$, directly from $NpCl_4(DME)_2$, circumventing the need for an alkali-metal reducing agent.[144] This work is analogous to our recent synthesis of a uranium(III) hydrocarbyl complex, $U[\eta^4\text{-}Me_2NC(H)C_6H_5]_3$, from reaction with $UCl_4$.[125] We demonstrate the utility of the Np complex and show that, unlike the uranium analogue, the products maintain the trivalent oxidation state after protonolysis reactions.

**General considerations**

The syntheses and manipulations described below were conducted using standard Schlenk and glove box techniques. Reactions were performed in a Vacuum Atmospheres inert atmosphere (Ar) glove box operated at negative pressure relative to the laboratory atmosphere. $[NpCl_4(DME)_2]$,[17] $K[Me_2NC(H)C_6H_5]$,[83] $HS_2C(2,6\text{-}Mes_2C_6H_3)$,[125] and $HO_2C(2,6\text{-}Mes_2C_6H_3)$,[145] were synthesized as previously described. All solvents were dried by passing through a solvent purification system, MBRAUN, USA and stored over activated 4 Å molecular sieves. Toluene-$d_8$ (Cambridge Isotope Laboratories) was degassed by three freeze-pump-thaw cycles and stored over activated 4 Å molecular sieves. All NMR data was obtained on a 300 or 600 MHz DRX Bruker spectrometer. $^1$H NMR shifts given were referenced internally to the residual solvent peak at δ 2.08 ppm ($C_7D_7H$). $^{13}$C NMR shifts given were referenced internally to the solvent peak at δ 20.43 ppm ($C_7D_8$). HMQC experiments were conducted to correlate the mesityl methyl protons with their respective carbons. Single X-ray crystal structure determinations were performed at the University of Missouri-Columbia.

**General considerations for $^{237}$Np.**

Caution! $^{237}$Np is an α-emitting radionuclide (4.958 MeV, $t_{1/2}$ = 2.14 x$10^6$ years, a= 0.7 mCi $g^{-1}$). This research was conducted in a radiological laboratory with appropriate counting equipment and analysis of hazards for the safe handling and manipulation of radioactive materials. Electronic absorption measurements were recorded on a sealed 1 cm quartz cuvette with a Varian Cary 5000 UV/vis/NIR spectrophotometer

**Synthesis of Np[$\eta^4$-$Me_2NC(H)C_6H_5$]$_3$, 1**. A 20 mL scintillation vial was charged with $NpCl_4(DME)_2$ (27.0 mg, 0.048 mmol) and THF (2 mL). The solution was placed in a -35 °C freezer for 30 min before adding it to K[$Me_2NC(H)C_6H_5$] (33.3 mg, 0.192 mmol). The solution was stirred for 2.5 h and the volatiles removed *in vacuo*. The residue was extracted with toluene (2x2 mL), filtered through Celite and the volatiles were removed *in vacuo* to give a black solid. X-ray quality crystals were grown from a concentrated toluene solution layered with pentane at -35°C. (Yield = 13.7 mg, 44%). $^1$H NMR ($C_7D_8$, 300 MHz, 233 K): δ 20.45(s, 3H, C*H*), 9.19 (s, 3H, C*H*), 7.99(s, 3H, C*H*), 7.70 (br s, 9H, C$H_3$), 0.04 (s, 9H, C$H_3$), -2.21 (s, 3H, C*H*), -15.01 (br s, 1H, C*H*), -62.53 (br s, 1H, C*H*).

**Synthesis of [(2,6-$Mes_2$-$C_6H_3$)$CO_2$]$_3$Np(THF)$_2$, 2**. A 20 mL scintillation vial was charged with Np[$\eta^4$-$Me_2NC(H)C_6H_5$]$_3$ (19.8 mg, 0.031 mmol) and THF (2 mL). A second 20 mL scintillation vial was charged with $HO_2C$(2,6-$Mes_2C_6H_3$) (33.3 mg, 0.093 mmol) and THF (2 mL). The vials were placed in a -35 °C freezer for 10 minutes and then the solutions were combined and stirred at room temperature for 4 h. The volatiles were removed *in vacuo* resulting in a pale-yellow solid. X-ray quality crystals were grown from a concentrated toluene solution layered with pentane at -35°C. (Yield = 7.8 mg, 17%). $^1$H NMR ($C_7D_8$, 600 MHz, 273 K): The 12H peak for ArCH is buried under the

solvent peaks, δ 6.43 (d, 6H, C*H*), 2.56 (s, 18H, C$H_3$), 1.79 (s, 36H, C$H_3$), unable to definitively assign the (3H, CH) or coordinated THF peaks. $^{13}$C NMR: 21.83 (Mes-$CH_3$), 20.59 (Mes-$CH_3$).

**Synthesis of [(2,6-$Mes_2$-$C_6H_3$)$CS_2$]$_3$Np(THF)$_2$, 3**. A 20 mL scintillation vial was charged with Np[$\eta^4$-$Me_2NC(H)C_6H_5$]$_3$ (11.4 mg, 0.018 mmol) and THF (1 mL). A second 20 mL scintillation vial was charged with $HS_2C$(2,6-$Mes_2C_6H_3$) (20.9 mg, 0.053 mmol) and THF (1 mL). The vials were placed in a -35 °C freezer for 15 minutes and then the solutions were combined and stirred at room temperature for 4 h. The volatiles were removed *in vacuo* resulting in a dark green solid. X-ray quality crystals were grown from a pentane solution at -35°C. (Yield = 9.7 mg, 35%). $^1$H NMR ($C_7D_8$, 300 MHz, 253 K): δ 6.75 (t, 3H, C*H*), 6.62 (s, 12H, C*H*), 6.24 (d, 6H, C*H*), 2.41 (s, 36H, C$H_3$), 2.14 (s, 18H, C$H_3$), 1.93 (br s, 8H, THF), 1.16 (br s, 8H, THF). $^{13}$C NMR: 23.89 (Mes-$CH_3$), 21.29 (Mes-$CH_3$).

**Crystallographic Data Collection and Structure Determination**.

The selected single crystal was coated with viscous hydrocarbon oil inside the glove box before being mounted on a nylon cryoloop using Devcon 2 Ton epoxy. The X-ray data were collected on a Bruker CCD diffractometer with monochromated Mo-Kα radiation (λ = 0.71073 Å). The data collection and processing utilized Bruker Apex2 suite of programs.[32] The structures were solved using direct methods and refined by full-matrix least-squares methods on F2 using Bruker SHELX-2014/7 program.[33] All non-hydrogen atoms were refined with anisotropic displacement parameters. All hydrogen atoms were placed at calculated positions and included in the refinement using a riding model.

Thermal ellipsoid plots were prepared by using Olex2[34] with 50% of probability displacements for non-hydrogen atoms.

**Table 3-1.** X-ray crystallography parameters of complexes **1-3**.

| | **1** | **2** | **3** |
|---|---|---|---|
| CCDC deposit number | 1910635 | 1910634 | 1910633 |
| Empirical formula | $C_{27}H_{36}N_3Np$ | $C_{83}H_{91}O_8Np$ | $C_{83}H_{91}O_2S_6Np$ |
| Formula weight (g/mol) | 639.59 | 1453.60 | 1549.91 |
| Crystal habit, color | Prism, black | Block, orange | Plate, brown |
| Temperature (K) | 100 | 100 | 253(2) |
| Space group | $P2_1/c$ | C2/c | *Cmcm* |
| Crystal system | Monoclinic | Monoclinic | Orthorhombic |
| Volume ($Å^3$) | 2463.2(4) | 15785.6(18) | 8398.6(11) |
| *a* (Å) | 14.2807(13) | 20.4620(14) | 26.036(2) |
| *b* (Å) | 11.5458(10) | 21.0845(14) | 18.8814(13) |
| *c* (Å) | 14.9662(13) | 36.609(2) | 17.0846(13) |
| $\alpha$ (˚) | 90.00 | 90.00 | 90.00 |
| $\beta$ (˚) | 93.4450(10) | 91.879(2) | 90.00 |
| $\gamma$ (˚) | 90.00 | 90.00 | 90.00 |
| *Z* | 4 | 8 | 4 |

| | | | |
|---|---|---|---|
| Calculated density ($Mg/m^3$) | 1.725 | 1.346 | 1.226 |
| Absorption coefficient ($mm^{-1}$) | 4.237 | 1.374 | 1.427 |
| Final R indices [$I > 2\sigma(I)$] | R = 0.0418<br>$R_W$ = 0.0560 | R = 0.0570<br>$R_W$ = 0.1110 | R = 0.0276<br>$R_W$ = 0.0697 |

**Magnetic Measurements**

In an argon filled glovebox, **2** (7.79 mg) and **3** (9.66 mg) were loaded into 3 mm OD quartz tubes by sandwiching them between two plugs of oven-dried quartz wool (**2**, 16.5 mg; **3**, 9.8 mg;) (Hereaus, semiconductor grade). The samples were compressed into a pellet by squeezing them between two quartz rods. The quartz rods were removed, and the ends of the tube were capped by inserting them into septa for 7 mm tubing. The capped tube was removed from the glovebox and decontaminated. The center of the tube was wrapped with a Kimwipe, saturated with liquid nitrogen, and sealed with a propane/oxygen torch. The samples were additionally contained in a He-filled, 3.5 mm polypropylene straw and heat sealed on both ends. Variable temperature magnetization data were recorded at 0.1 T, 0.5 T, 1 T and 4 T (**2-3**) using a Quantum Designs MPMS SQUID magnetometer. Variable temperature magnetization was corrected for the diamagnetism of the quartz wool using Pascal's constants for covalent compounds, $\chi_{QW} = 3.7 \times 10^{-7}$ emu $g^{-1}$ (no correction for the diamagnetism of the quartz tube or polypropylene straw is needed as they never leave the SQUID coils). Molar susceptibility was calculated using the following equation:

$$\chi_{mol} = \frac{(\text{molecular weight})}{(\text{sample mass})}\left[\frac{(M_{meas} - M_{ferro})}{H} - \chi_{QW}\right] - \chi_{dia}$$

**Figure 3-1.** Equation used to calculate molar susceptibility.

Where $\chi_{mol}$ is the molar susceptibility, $M_{meas}$ is the measured magnetization, $M_{ferro}$ is the ferromagnetic magnetization of the ferromagnetic impurity, which is temperature independent; its field dependence, f, is 1 at fields greater than 0.2 T and is f is ~0.65 at 0.1 T, $\chi_{QW}$ is the contribution to the susceptibility due to the quartz wool, $\chi_{dia}$ is the diamagnetic correction of the ligands and neptunium using Pascal's constants, and H is the applied field. Two ferromagnetic impurities are commonly encountered in laboratory samples, steel or iron metal and magnetite or other ferrites from oxide coating on stainless steel lab equipment. Of these, magnetite is far more likely to be encountered. In general, the magnetization of ferromagnets is temperature independent below the Curie temperature, which is 860 K for magnetite, so magnetization of the impurity is temperature independent for this experiment. The magnetization of magnetite reaches saturation at approximately 0.2 T, above which the magnetization is ~90 emu/g.[35] Below this field, the magnetization of magnetite is roughly linear with applied field. Based on the assumption that the impurity is magnetite or a related ferrite resulting from the abrasion of stainless-steel lab equipment, the data were corrected for a temperature and field independent ferromagnetic impurity. $M_{ferro}$ was allowed to vary to minimize the least squares difference between $\chi_{mol}$ at different fields, which produced a saturation of magnetization of $M_{ferro} = 7.57 \times 10^{-5}$ emu (~0.69 μg of magnetite) for **2**, $M_{ferro} = 4.99 \times 10^{-5}$ emu (~0.45 μg of magnetite) for **3**.

**Results and Discussion**

The reaction of $NpCl_4(DME)_2$ with four equivalents of $K[Me_2NC(H)C_6H_5]$ produced an immediate color change from pink to black (Figur**e** 3-2).The reaction was conducted in THF at -35 °C since the potassium salt will react with THF at room temperature.[83]After 2.5 hours, the solution was filtered through Celite, and the volatiles were removed under vacuum leaving a black powder.

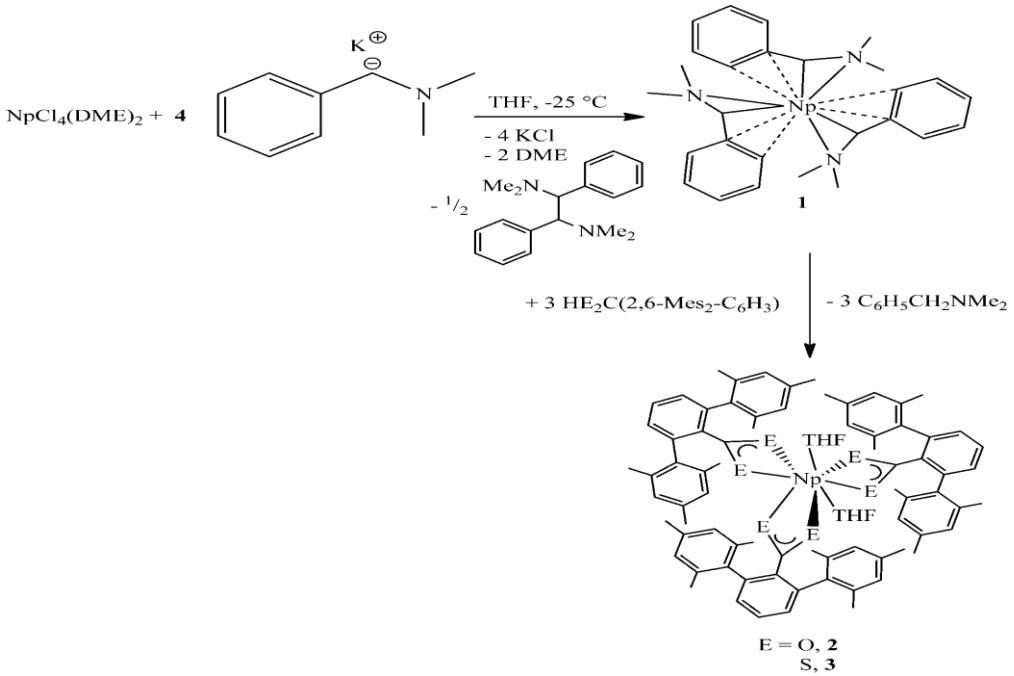


**Figure 3-2.** Reaction scheme of the synthesis of complexes **1**, **2**, and **3**.

The resonances for the Np product in the $^1$H NMR spectrum in toluene-$d_8$ range from δ = 20.45 to 62.53 ppm with features in the nIR spectrum consistent with $Np^{III}$ ions having weak 5f–5f transitions.[143] The $^1$H NMR spectrum also contained the reductive coupling of two ligands which, because of similar solubilities, could not be separated from the neptunium complex. The reduction of $Np^{IV}$ to $Np^{III}$ is not unexpected given the relative stability of $Np^{III}$ compared to $U^{III}$. A variety of elements undergo similar reductions with

alkali metal substrates.[146,147] Crystals suitable for X-ray crystallographic analysis were obtained from a concentrated toluene solution layered with pentane at -35 °C. The crystalline yield was approximately 44%. The structure (Figure 3-3) revealed Np[$\eta^4$-Me2NC(H)$C_6H_5$]$_3$, **1**, which is c previously reported. Complex **1** is the first structurally characterized neptunium(III) hydrocarbyl complex. Similar $^1$H NMR resonances are observed in both THF-$d_8$ and toluene-$d_8$, and no decomposition was observed by heating **1** to -50 °C in THF overnight, demonstrating its thermal stability.

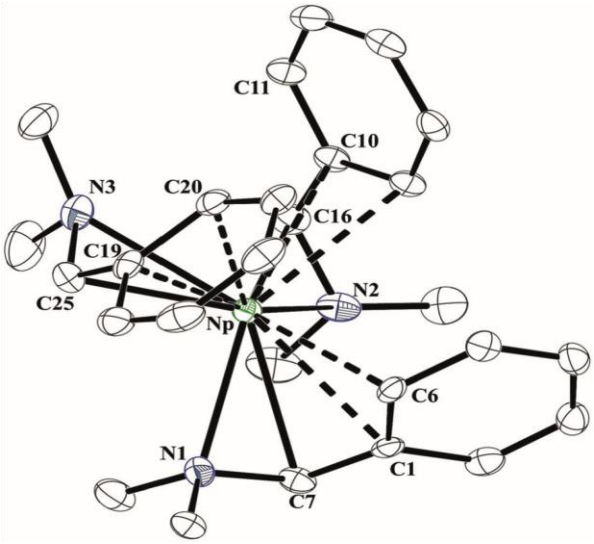


**Figure 3-3.** Thermal ellipsoid plot of **1** shown at the 50% probability level.[40] The hydrogen atoms have been omitted for clarity.

In **1**, the NpC(methine) bond distances are 2.592(4) Å (NpC7), 2.581(4) Å (NpC16), and 2.574(4) Å (NpC25), while the NpN1, NpN2, and NpN3 distances are 2.552(3), 2.605(3), and 2.626(3) Å, respectively. The NpC bond lengths are shorter than those found in Np($C_5H_4SiMe_3$)$_3$ which all range from 2.734(6)–2.786(4) Å, but longer compared to the Np-centroid distances of 2.485(2), 2.481(2), and 2.479(2) Å.[142] The NpN bond distances in **1** are similar to those observed in Np($C_5H_5$)$_3$(NCMe)$_2$ of 2.665(4) Å.[142] Additionally,

NpC(ipso) distances in **1** are 2.787(4) Å (NpC1), 2.766(4) Å (NpC10), and 2.769(4) Å (NpC19), while the NpC(ortho) distances are 2.802(4) Å (NpC6), 2.813(4) Å (NpC11), and 2.805(4) Å (NpC20). These distances are similar to those observed in the uranium analogue,[125] and much shorter than the agostic interactions seen in $Pu[N(SiMe_3)_2]_3$ of 2.968(9) Å.[148] Therefore, we consider this ligand having an $\eta^4$ coordination mode with the agostic interactions being a reasonable explanation for the stability of **1**.

As a final comparison, the ionic radii of six-coordinate $Np^{III}$ and $Ce^{III}$ are both 1.01 Å,[100] hence we can compare the distances in **1** to the $Ce^{III}$ analogue,[83] which sits on a pseudo threefold axis of symmetry. However, the CeC(methine) bond distances are 2.617(3) Å, which are Δ=0.025(3) Å (Np C7), 0.036(3) Å (NpC16), and 0.043(3) Å (NpC25) longer than the NpC(methine) distances in **1**. The closest lanthanide with similar bond distances to **1** is the Nd analogue which has an ionic radius of 0.953 Å. The analogous Nd complex has NdC(methine) distances of 2.588(3) Å,[83] with the average NpC(methine) distance in **1** being 2.582(4) Å. This comparison demonstrates the enhanced actinide–ligand bonding that is well-established in 4f versus 5f complexes.[149-154]

To demonstrate that **1** can be used as a starting material to obtain other trivalent neptunium complexes, the reaction of **1** with three equivalents of $HO_2C(2,6\text{-}Mes_2\text{-}C_6H_3)$[145] was performed (Figure 3-2). A pale-yellow solution was afforded. Upon crystallization from a concentrated pentane solution at -35° C, X-ray crystallography revealed the structure of the trivalent product, $[(2,6\text{-}MesC_6H_3)CO_2]_3Np(THF)_2$ (Figure 3-5). The crystalline yield was approximately 17%. The UV-vis-nIR spectrum shows an absorption at 400 nm. In addition, features around 1350 nm in the nIR region are indicative of $Np^{III}$.

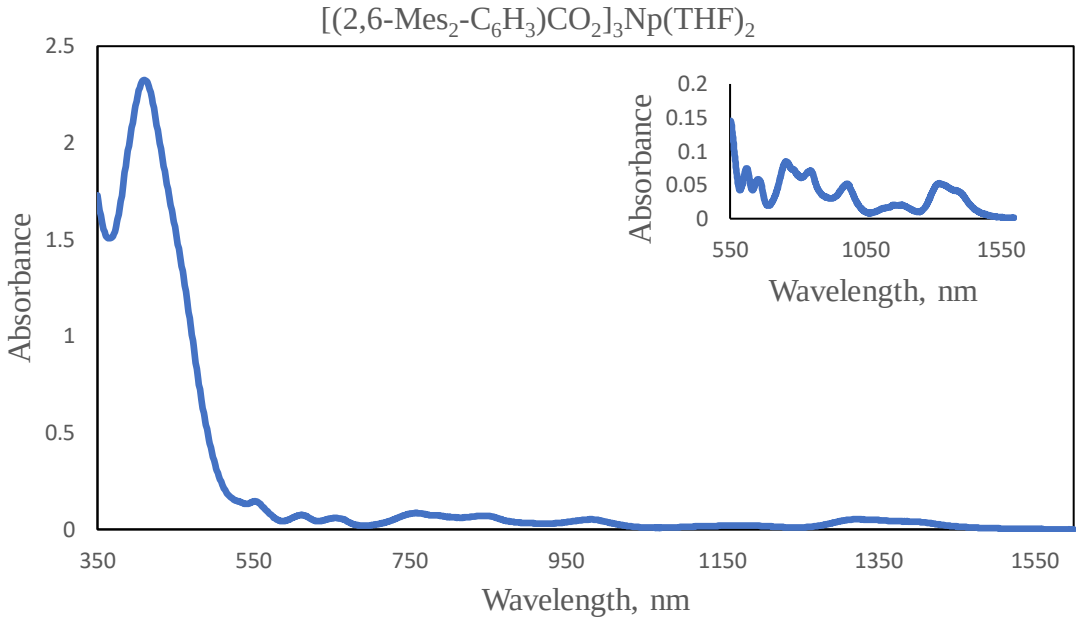


**Figure 3-4.** Electronic absorption spectrum of **2** in toluene.

The three carboxylate ligands are situated in the equatorial plane while the two THF adducts are in an axial position. The NpO(carboxylate) bond distances range from 2.435(3)–2.552(3) Å and are longer than the only other $Np^{III}$-alkoxide, $K(DME)_n\{(L^{Ar\text{-}H})Np(OCH_3)\}_2$ ($L^{Ar}$ =*trans*-calix[2]benzene[2]pyrrole), reported at 2.288(9) Å.[115] The elongation of the NpO bond distances in **2** are presumably a result of the steric encumbrance and chelating ability of the carboxylate ligand. The NpO(THF) bond distances of 2.469(3) and 2.479(3) Å are similar to those NpO(THF) of 2.487(4), 2.513(5) and 2.538(6) Å in $(LAr)Np_2Cl_4(THF)_3$.[115]

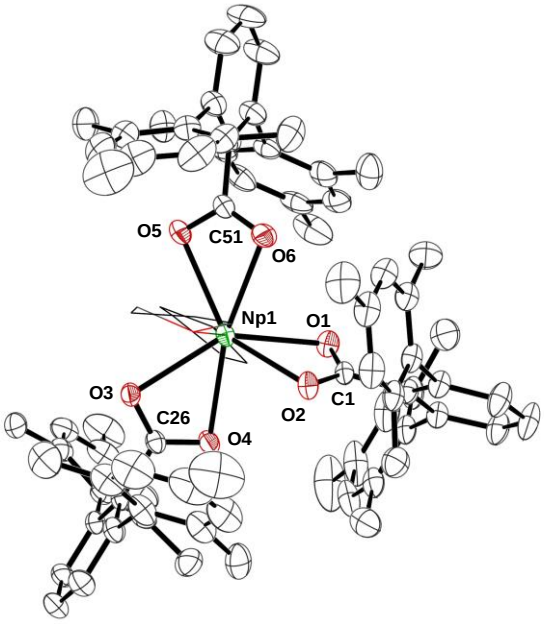


**Figure 3-5.** Thermal ellipsoid plot of **2** shown at the 50% probability level. The hydrogen atoms have been removed as well as the THF molecules shown in wireframe for clarity.

To observe whether $Np^{III}$ would oxidize upon reaction with a dithiocarboxylate in a similar manner as its uranium analogue, the reaction of **1** with $HS_2C(2,6\text{-}Mes_2C_6H_3)$ was attempted (Figure 3-2). The color instantly turned from black to dark green. The product, $[(2,6\text{-}MesC_6H_3)CS_2]_3Np(THF)_2$, **3**, was characterized by X-ray crystallography (Figure 3-6) and obtained in 35% crystalline yield. Complex **3** has a mirror plane on a $C_2$-axis of symmetry, which results in two of the dithiocarboxylate ligands being equivalent. The NpS distances in **3** range from 2.9286(10)–2.9550(10) Å with the Np-O(THF) distances similar to those in **2** at 2.467(3) Å. Only one other $Np^{III}$ complex has been reported with sulfur-based ligands, $[NEt_4][Np(S_2CNEt_2)_4]$. For comparison, its NpS distances range from 2.86(3)–2.91(3) Å.[155]

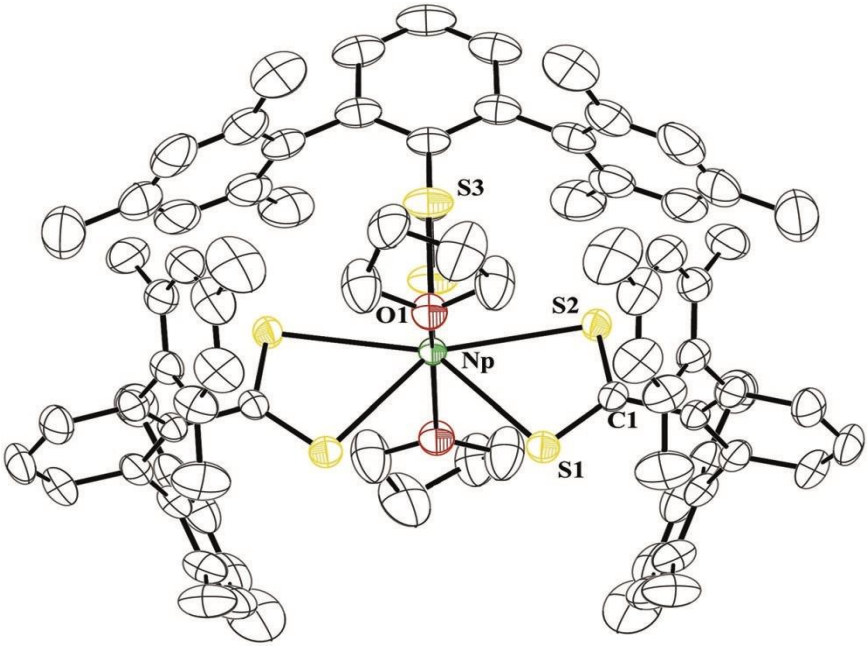


**Figure 3-6.** Thermal ellipsoid of **3** shown at the 50% probability level.[40] The hydrogen atoms have been omitted for clarity.

The magnetism of **2** and **3** were measured to corroborate the assignment of a trivalent oxidation state. Given similar solubilities, the coupled ligand could not be removed from **1** satisfactorily, therefore the magnetism of **1** was not measured. The ground state of $Np^{III}$ is $^5I_4$ under Russell Saunders (RS) coupling, and its free ion moment is 2.68 $\mu_B$. Under intermediate coupling, the ground state of $Np^{III}$ is primarily (80%) $^5I_4$ and the free ion moment is larger 2.88 $\mu_B$ as determined using $\mu_B = g_J[J(J+1)]^{1/2}$ and $g_J$, for intermediate coupling, 0.644.[156] Unlike $U^{III}$ and $U^{IV}$, $Np^{III}$ and $Np^{IV}$ have quite different moments in the ground state, 2.88 $\mu_B$ and 3.82 $\mu_B$, respectively, for intermediate coupling. This large difference allows the oxidation states to be determined from the magnetic moments at room temperature if the splitting of the ground-state multiplets is small (less than 200

$cm^{-1}$, the value of kT at 300 K). Since the splitting is often larger, especially for tetravalent actinide ions, which experience a larger crystal field, the room-temperature magnetic moments do not allow differentiation between $Np^{III}$ and $Np^{IV}$.

For **3**, the value of χT approaches zero as the temperature approaches zero, which indicates that the ground state is a singlet state (Figure 3-7). This result is common for a $5f^4$ configuration as illustrated by $PuO_2$, which also has a singlet ground state.[157,158] This situation is also common among $U^{IV}$, $f^2$, complexes. The ground states of both $UCl_6^{2-}$ and $UBr_6^{2-}$ are singlets,[159,160] as is the ground state of $(1,3\text{-}^tBu_2C_5H_3)_2UCl_2$.[161] At high temperature, the magnetic moment of 2.7 $\mu_B$ approaches the free ion moment and indicates that the splitting of the $^5I_4$ state by the ligands is relatively small. The magnetic susceptibility results support a $Np^{III}$ ground state for **3**.

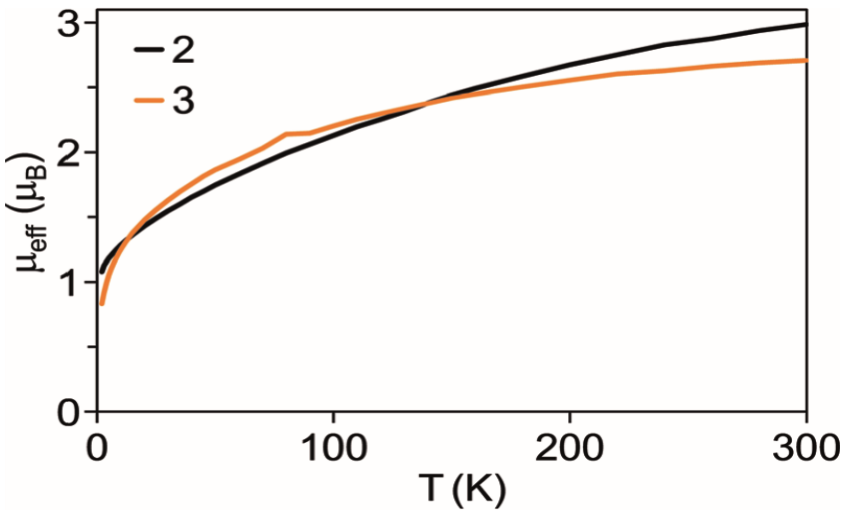


**Figure 3-7.** Variable-temperature magnetic moment of **2** and **3** at 0.1 T.

For **2**, the value of χT decreases as T approaches zero, but it does not approach zero. Instead, the low-temperature moment of **2** is 1.1 $\mu_B$. The magnetic moment at room

temperature is **3** $\mu_B$, which is slightly greater than the free-ion moment of the lowest state of $Np^{III}$, but considerably less than the free-ion moment for $Np^{IV}$ in intermediate coupling, 3.82 $\mu_B$. The $^1$H NMR spectra of **2** and **3** support a greater magnetic moment for **3**. The chemical shifts of the mesityl methyl protons are $\delta$ = 1.99 ppm and 2.36 ppm for the *ortho* and *para* methyl groups, respectively. In **3**, these resonances are found at $\delta$ = 2.41 ppm and 2.14 ppm, respectively. In **2**, the chemical shifts are further from their diamagnetic values at $\delta$ = 2.56 ppm and 1.79 ppm. A potential explanation of the difference between the magnetic susceptibilities of **2** and **3**, especially the greater moment of **2**, is the difference in the crystal fields of sulfur- and oxygen-based ligands. As illustrated with chromium halides by Burdett,[144] destabilization of metal orbitals is proportional to the ligand ionization potential as well as to the overlap between the metal and ligand orbitals. Because the carboxylate orbitals involved in bonding with Np are more stable than the corresponding dithiocarboxylate orbitals, the crystal field of the carboxylate ligand is expected to be greater than that of the dithiocarboxylate ligand even if the overlap is similar in both complexes. The obvious effect of this difference is to change the energies of the low-lying excited states created by splitting ground multiplet ($^5I_4$ in RS coupling). As a result, the shapes of the $\mu_{eff}$ vs. T curves of **2** and **3** are different. However, the crystal field also mixes excited multiplets (e.g., $^5I_5$ in RS coupling) into the ground state, which can increase the magnetic moment of the complex (the moment of $^5I_5$ state is 4.93 $\mu_B$ in RS coupling). The larger magnetic moment of **2** relative to **3** is consistent with the larger crystal field expected for the carboxylate ligand relative to the dithiocarboxylate.

## Conclusion

In summary, the synthesis and characterization of a neptunium(III) hydrocarbyl complex is reported. This compound is the first structurally and thoroughly characterized hydrocarbyl complex beyond uranium and has been demonstrated to be a starting material to form further $Np^{III}$ complexes. Given the stability of **1**, it is plausible that this moiety could be applied to other transuranic elements such as plutonium and americium, which have even greater stability of the trivalent oxidation state and for which the starting materials already exist.[17,162] These also represent rare examples of $Np^{III}$ complexes for which further chemistry can be explored by utilizing the Np(IV/III) or potentially the Np(V/III) redox couple.

# Chapter 4: Formation of Np(IV)-Chalcogenido Bonds from E-E Bond Cleavage with a Np(III) Aryloxide Complex

This chapter is based on a manuscript that is currently in progress.

Alexander J. Myers, Michael L. Tarlton, Steven P. Kelley, and Justin R. Walensky*

## Introduction

The chemistry of low-valent actinide has been of great interest due to the isolation of actinides in rare divalent oxidation states,[111-116] small molecule activation,[133,134] and examining metal-ligand bonding.[149,163-169] This is especially true of U(III), a powerful reducing agent.[170] However, when one traverses the actinide series, there is a propensity to favor the trivalent oxidation state, much like their lanthanide counterparts.

Our group has an interest in low-valent actinide complexes, especially of neptunium, since this is rarely studied.[10] It is important to understand the fundamental chemistry of neptunium due to its formation after irradiating uranium with neutrons, as well as the need for neptunium, and other byproducts, to be removed when reprocessing spent nuclear fuel. Furthermore, under highly reducing conditions, like the ones found in storage tanks, it is conceivable that Np(III) and Np(IV) species may persist.[12] Hence, the coordination chemistry and redox properties of $Np^{IV/III}$ complexes can provide valuable insight into advanced separation techniques, in addition to advancing our understanding of this understudied element.

Actinide-chalcogen bonds have been extensively studied since extractants with sulfur-based donor atoms such as Cyanex 301 show higher affinity for actinides over their lanthanide counterparts.[171] The reduction of E-E bonds is a common method for the installation of f-element-chalcogenide bonds. Recently, we described the synthesis of a

Np(III) hydrocarbyl complex, Np[$\eta^4$-$Me_2NC(H)C_6H_5]_3$,[172] and its ability to produce other Np(III) complexes through protonolysis reactions. Here, we demonstrate that Np[$\eta^4$-$Me_2NC(H)C_6H_5]_3$ with three equivalents of 2,6-$^tBu_2C_6H_3OH$ forms the previously reported, Np(O-2,6-$^tBu_2C_6H_3)_3$, **1**, which can reductively cleave the chalcogen-chalcogen bond in benzoyl peroxide and PhSSPh, to form (2,6-$^tBu_2C_6H_3O)_3$Np($\kappa^2$-$O_2CC_6H_5$), **3**, and (2,6-$^tBu_2C_6H_3O)_3$Np(SPh), **4**. Similar oxidation chemistry with uranium was explored by Burns.[173]

Additionally, the weaker redox properties of Np(III) compared to U(III) was demonstrated. The uranium(III) tris(anilide) complex (THF)U(N[*t*-Bu]Ar)$_3$, (Ar = 3,5-$Me_2C_6H_3$) reported by Cummins reduces [N($^n$Bu)$_4$]$N_3$ to form a bridging nitride.[174] However, attempting a similar reaction with Np(O-2,6-$^tBu_2C_6H_3)_3$, **1**, and half an equivalent of [N($^n$Bu)$_4$]$N_3$, forms the bridging azide complex [(Np(O-2,6-$^tBu_2$-$C_6H_3)_3)_2$-$\mu$-$N_3$][N($^n$Bu)$_4$], **5**. This represents one of the first studies of Np(III) redox chemistry.

**General Considerations for Np-237**

Caution! $^{237}$Np is an α-emitting radionuclide (4.958 MeV, $t_{1/2} = 2.14 \times 10^6$ years, and a = 0.7 mCi g$^{-1}$). This research was conducted in a radiological laboratory with appropriate counting equipment and analysis of hazards for the safe handling and manipulation of radioactive materials. Reactions were performed in a Vacuum Atmospheres inert-atmosphere (Ar) glovebox operated at negative pressure relative to the laboratory atmosphere. [$NpCl_4(DME)_2$][17] and Np[$\eta^4$-$Me_2NC(H)C_6H_5]_3$[172] were synthesized as previously described. Benzoyl peroxide was dried over magnesium sulfate before use. 2,6-di-tert-butylphenol was recrystallized out of pentane and dried before use. All other reagents were used as received

**Synthesis of Np(O-2,6-$^t$Bu$_2$-C$_6$H$_3$)$_3$(THF)$_2$, 1**. A 20 mL scintillation vial was charged with Np[$\eta^4$-Me$_2$NC(H)C$_6$H$_5$]$_3$ (11.5 mg, 0.018 mmol) and pentane (2 mL). A second 20 mL scintillation vial was charged with HO-2,6-$^t$Bu$_2$C$_6$H$_3$ (11.5 mg, 0.056 mmol) and pentane (1 mL). The solutions were combined and stirred for 1 hour at room temperature before 3 drops of THF were added. The solution was filtered through Celite and concentrated. X-ray quality crystals were grown from a concentrated pentane solution at -35°C.

**Synthesis of Np(O-2,6-$^t$Bu$_2$-C$_6$H$_3$)$_4$, 2**. A 20 mL scintillation vial was charged with NpCl$_4$(DME)$_2$ (12.5 mg, 0.022 mmol) and THF (1 mL). A second 20 mL scintillation vial was charged with KO-2,6-$^t$Bu$_2$C$_6$H$_3$ (22.0 mg, 0.089 mmol) and THF (1 mL). The solutions were combined and stirred for 2 hours at room temperature. The volatiles removed *in vacuo*, extracted into Et$_2$O and filtered through Celite. X-ray quality crystals were grown from a slow evaporation of Et$_2$O at -35°C.

**Synthesis of Np(O-2,6-$^t$Bu2-C$_6$H$_3$)$_3$(O$_2$C(C$_6$H$_5$)), 3**. A 20 mL scintillation vial was charged with Np[$\eta^4$-Me$_2$NC(H)C$_6$H$_5$]$_3$ (22.8 mg, 0.036 mmol) and toluene (2 mL). A second 20 mL scintillation vial was charged with HO-2,6-$^t$Bu$_2$C$_6$H$_3$ (22.1 mg, 0.11 mmol) and toluene (1 mL). The solutions were combined and stirred at room temperature for 30 minutes at room temperature before a precooled solution of (C$_6$H$_5$CO)$_2$O$_2$ (4.3 mg, 0.018 mmol) in toluene (1 mL) was added. The solution was stirred for an additional 2 hours at room temperature and the volatiles removed *in vacuo*. The resulting dark-red residue was extracted into pentane, filtered through Celite, and concentrated. X-ray quality crystals were grown from a concentrated pentane solution at -35°C.

**Synthesis of Np(O-2,6-$^{t}$Bu$_2$-C$_6$H$_3$)$_3$(S(C$_6$H$_5$)), 4**. A 20 mL scintillation vial was charged with Np[$\eta^4$-Me$_2$NC(H)C$_6$H$_5$]$_3$ (24.8 mg, 0.039 mmol) and toluene (3 mL). A second 20 mL scintillation vial was charged with HO-2,6-tBu$_2$C$_6$H$_3$ (24.1 mg, 0.12 mmol) and toluene (1 mL). The solutions were combined and stirred for 30 minutes at room temperature before a precooled solution of $Ph_2S_2$ (4.2 mg, 0.019 mmol) in toluene (1 mL) was added. The solution was stirred for an additional 2 hours and the volatiles removed *in vacuo*. The resulting dark-red residue was extracted into pentane, filtered through Celite, and concentrated. X-ray quality crystals were grown from a concentrated pentane solution at -35°C.

**Synthesis of [(Np(O-2,6-$^{t}$Bu$_2$-C$_6$H$_3$)$_3$)$_2$-μ-N$_3$][N($^{n}$Bu)$_4$], 5**. A 20 mL scintillation vial was charged with Np[$\eta^4$-Me$_2$NC(H)C$_6$H$_5$]$_3$ (17.8 mg, 0.028 mmol) and toluene (2 mL). A second 20 mL scintillation vial was charged with HO-2,6-$^{t}$Bu$_2$C$_6$H$_3$ (17.3 mg, 0.084 mmol) and toluene (1 mL). The solutions were combined and stirred for 30 minutes at room temperature before a precooled solution of [N($^{n}$Bu)$_4$]N$_3$ (4.0 mg, 0.014 mmol) in toluene (1 mL) was added. The solution was stirred for an additional 2 hours and the volatiles removed *in vacuo*. The resulting yellow residue was extracted into THF, filtered through Celite, concentrated and layered with pentane. X-ray quality crystals were grown from a concentrated THF solution layered with pentane at -35°C.

**Crystallographic Data Collection and Structure Determination**.

Selected single crystals were mounted on nylon cryoloops using using Devcon 2 Ton epoxy. X-ray data collection was performed at 100(2) K. The X-ray data were collected on a Bruker CCD diffractometer with monochromated Mo-Kα radiation (λ = 0.71073 Å). The data collection and processing utilized Bruker Apex2 suite of programs.[32] The

structures were solved using direct methods and refined by full-matrix least-squares methods on F2 using Bruker SHELX-2014/7 program.[33] All non-hydrogen atoms were refined with anisotropic displacement parameters. All hydrogen atoms were placed at calculated positions and included in the refinement using a riding model. Thermal ellipsoid plots were prepared by using Olex2[34] with 50% of probability displacements for non-hydrogen atoms. Crystal data and details for data collection for complexes **1-5** are also provided in Table 4-1.

**Table 4-1.** X-ray crystallography data is shown for complexes **1-5**.

| | **1** | **2** | **3** | **4** | **5** |
|---|---|---|---|---|---|
| Empirical formula | $C_{50}H_{79}O_5Np$ | $C_{56}H_{84}O_4Np$ | $C_{49}H_{68}O_5Np$ | $C_{48}H_{68}O_3S_1Np$ | $C_{100}H_{162}O_6N_4Np_2$ |
| Formula weight (g/mol) | 997.13 | 1058.23 | 974.03 | 962.08 | 1990.37 |
| Crystal habit, color | Prism, yellow | Prism, red | Block, red | Plank, dark violet | Prism, red |
| Temperature (K) | 100(2) | 100(2) | 100(2) | 100(2) | 100(2) |
| Space group | *P 1 21/n 1* | *I -4* | *$P12_1/c1$* | *C12/c1* | *P -1* |
| Crystal system | Monoclinic | Tetragonal | Monoclinic | Monoclinic | Triclinic |
| Volume ($Å^3$) | 4771.1(3) | 2636.79(17) | 4415.3(3) | 17665(2) | 5252.0(4) |
| *a* (Å) | 10.0899(3) | 14.0240(4) | 11.5431(4) | 77.138(6) | 17.2966(8) |
| *b* (Å) | 20.5612(7) | 14.0240(4) | 38.8666(11) | 10.0147(8) | 17.6087(9) |
| *c* (Å) | 23.0086(7) | 13.4070(4) | 10.4800(4) | 23.1937(18) | 18.9127(9) |
| $\alpha$ (˚) | 90.00 | 90.00 | 90.00 | 90.00 | 94.488(2) |
| $\beta$ (˚) | 91.7690(10) | 90.00 | 110.1050(10) | 99.632(2) | 111.421(2) |
| $\gamma$ (˚) | 90.00 | 90.00 | 90.00 | 90.00 | 98.312(2) |
| *Z* | 4 | 2 | 4 | 16 | 4 |

| | | | | | |
|---|---|---|---|---|---|
| Calculated density ($Mg/m^3$) | 1.730 | 1.333 | 1.465 | 1.447 | 6.489 |
| Absorption coefficient ($mm^{-1}$) | 2.221 | 2.012 | 2.398 | 4.173 | 2.018 |
| Final R indices [$I > 2\sigma(I)$] | R = 0.0571 $R_W$ = 0.0368 | R = 0.0129 $R_W$ = 0.0129 | R = 0.0813 $R_W$ = 0.0648 | R = 0.0218 $R_W$ = 0.0427 | R = 0.0877 $R_W$ = 0.0599 |

## Results

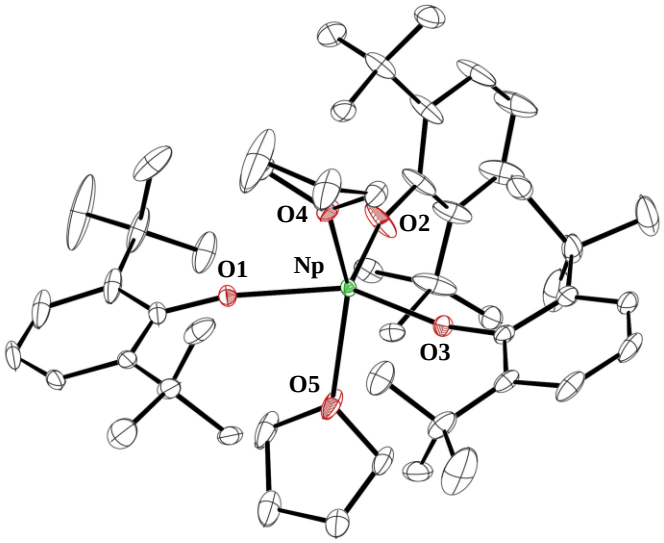


**Figure 4-1.** Thermal ellipsoid plots of **1** shown at the 50% probability level. The hydrogen atoms been omitted for clarity.

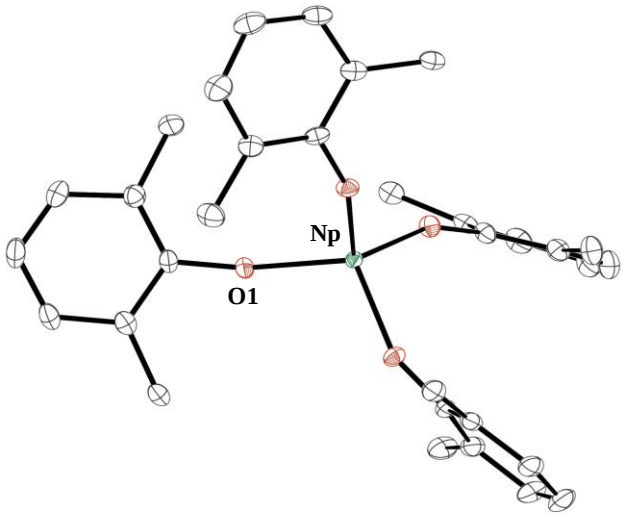


**Figure 4-2.** Thermal ellipsoid plots of **2** shown at the 50% probability level. The hydrogen atoms and *tert*-butyl groups have been omitted for clarity.

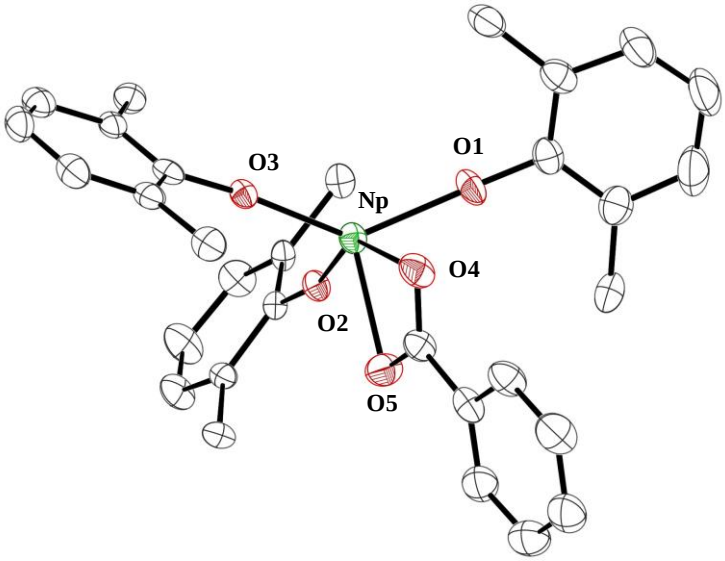


**Figure 4-3.** Thermal ellipsoid plots of **3** shown at the 50% probability level. The hydrogen atoms and *tert*-butyl groups have been omitted for clarity.

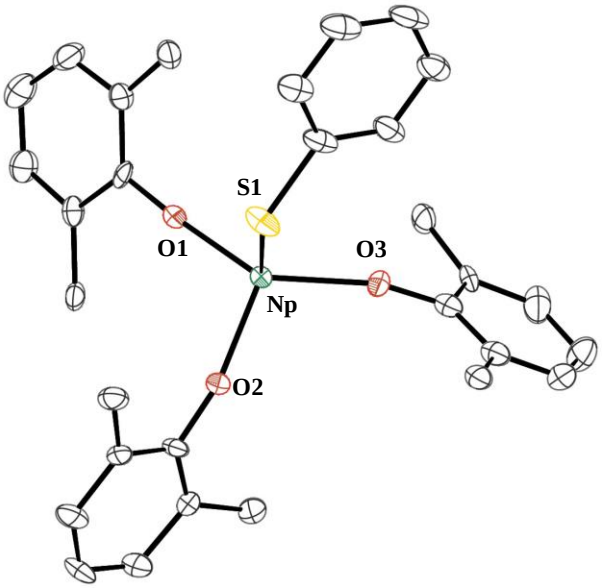


**Figure 4-4.** Thermal ellipsoid plots of **4** shown at the 50% probability level. The hydrogen atoms and *tert*-butyl groups have been omitted for clarity.

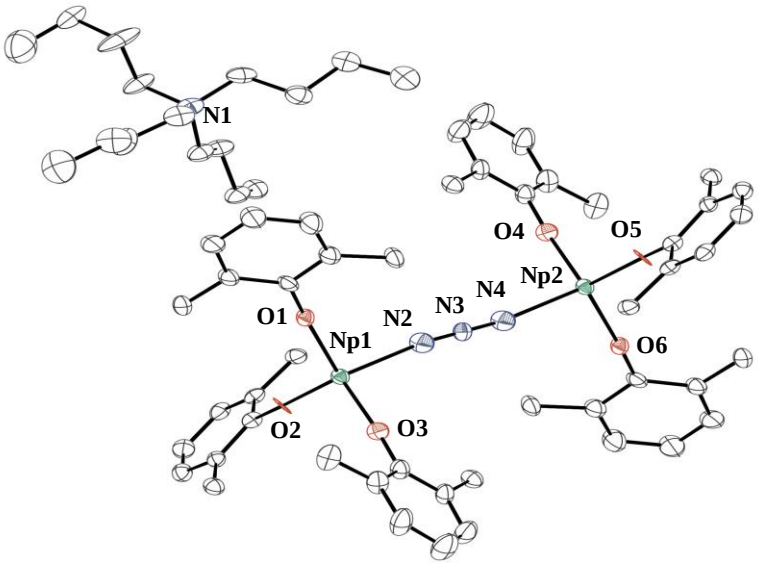


**Figure 4-5.** Thermal ellipsoid plots of **5** shown at the 50% probability level. The hydrogen atoms and *tert*-butyl groups have been omitted for clarity.

# Appendix A: Influence of Substituents on the Electronic Structure of Mono- and Bis(Phosphido) Thorium(IV) Complexes †

† This chapter is based on a manuscript that was submitted to and accepted by Inorganic Chemistry and can be cited as: Rungthanaphatsophon, P.; Duignan, T. J.; **Myers, A. J.**; Vilanova, S. P.; Barnes, C. L.; Autschbach, J.; Batista, E. R.; Yang, P.; Walensky, J. R. Influence of Substituents on the Electronic Structure of Mono- and Bis(Phosphido) Thorium(IV) Complexes, *Inorg. Chem.* **2018**, *57*, 7270.

Note: My contribution to this project was the synthesis and characterization of complexes **1** and **4**.

## Introduction

While actinides prefer harder Lewis bases such as oxygen and nitrogen, the lower congeners of these elements, such as phosphorus, have been understudied. Interest in the heavier main-group elements stems from the observation that metal ligand orbital mixing in the actinide−ligand bond increases[149,165,175] going down a group. Hence, while the actinides typically show a preference for 2p elements, the energy between the 5f and np orbitals decreases with increasing n,[166,167,176] thus presenting the paradox that covalent bonding does not necessarily translate into strong covalent bonds. This concept is not shared in transition-metal and main-group elements[168] because the overlap between nd orbitals and np orbitals is significantly greater than the overlap between 5f and np orbitals.

While changing the steric properties of ligands is the typical focus for altering the reactivity of actinide complexes, electronic effects can have a profound influence on the chemical properties of the molecule. In the initial report of actinide− phosphorus bonds,

the reaction of $(C_5Me_5)_2ThCl_2$ with 2 equivalents of $KPPh_2$ produced a dark purple complex, $(C_5Me_5)_2Th(PPh_2)_2$.[177] A similar result was obtained for $(C_5Me_5)_2Th(PEt_2)_2$. While purple is an expected color for a paramagnetic species such as Th(III)[178] or a radical-based ligand,[179,180] the $^1H$ NMR spectrum of this complex appeared diamagnetic, suggesting the presence of a ligand-to-metal charge transfer (LMCT) in the ground state. Previously, we have reported bis(phosphido) complexes of thorium, $(C_5Me_5)_2Th[PH(C_6H_2R_3\text{-}2,4,6)]_2$ (R = $CH_3$,[181] $^iPr$[182]), but these complexes were pale yellow, similar to $(C_5Me_5)_2Th(Cl)[P(SiMe_3)_2]$.[183] This indicates that the ligand-to-metal charge transfer can be manipulated with respect to secondary versus primary phosphido ligands as well as a change in the substituents associated with secondary phosphidos. Curiously, the zirconium analogue $(C_5Me_5)_2Zr[PH(Mes)]_2$[184] is described as having a red wine color; thus, not all metallocene bis(phosphido) metal complexes are the same. Finally, metallocene complexes of thorium bis(amides) are pale in color.[185] For example, $(C_5Me_5)_2Th(NMe_2)_2$ is light yellow.[186] Again, phosphorus seems to be playing a significant role in the electronic structure of organothorium complexes.

Herein, we report a series of thorium phosphido complexes with the metallocene ligand framework. The colors of these complexes range from pale yellow to dark purple depending on the phosphorus substituents. The electronic structure has been investigated using UV−vis spectroscopy as well as time-dependent density functional theory calculations to show that the LMCT band originates from the donating properties of the phosphorus substituents. We correlate the donating strength of the substituents associated with phosphorus with the $^{31}P$ NMR

chemical shift but show that this does not translate into a convenient pattern for the UV−vis spectrum, indicating that there are additional factors contributing to the thorium−phosphorus bond.

**General Considerations**

All syntheses were carried out under a $N_2$ atmosphere using glovebox and Schlenk techniques. All solvents used were dried by passing through a solvent purification system (MBraun, USA). AgOTf and $KN(SiMe_3)_2$ were obtained from Sigma-Aldrich. $HP(Mes)_2$,[187] $HP(Mes)(SiMe_3)$,[188] $HP(Mes)(CH_3)$,[189] $(C_5Me_5)_2ThCl_2$,[190] $(C_5Me_5)_2ThMe_2$,[190] $(C_5Me_5)_2Th(CH_3)Cl$,[189] $(C_5Me_5)_2Th[PH(Mes)]_2$,[181] $(C_5Me_5)_2Th(Cl)[P(SiMe_3)_2]$,[183] $(C_5Me_5)_2Th(CH_3)[P(SiMe_3)_2]$,[183] and benzylpotassium[191] were synthesized as previously described. $K[P(Mes)_2]$ was prepared from $HP(Mes)_2$ and $KN(SiMe_3)_2$ in toluene.[191] $KP(Mes)(CH_3)$ was prepared from $HP(Mes)(CH_3)$ and $KN(SiMe_3)_2$ in toluene. Benzene-$d_6$ (Cambridge Isotope Laboratories) was degassed by three freeze–pump–thaw cycles and stored over activated 4 Å molecular sieves. All $^1H$ and $^{13}C\{^1H\}$ spectra were taken on either 500 or 600 MHz Bruker spectrometers. All $^{31}P\{^1H\}$, $^{29}Si$ INEPT, and $^{19}F$ spectra were taken on a 300 MHz Bruker spectrometer. All NMR chemical shifts are reported in ppm. $^1H$ NMR shifts are referenced internally to the residual solvent peak of $C_6D_5H$ at 7.16 ppm. $^{13}C$ NMR shifts were referenced internally to $^{13}C_6D_6$ at 128.06 ppm. $^{31}P\{^1H\}$ NMR shifts were referenced externally to 85% $H_3PO_4$ at 0 ppm. $^{29}Si$ NMR shifts were referenced externally to TMS at 0 ppm. $^{19}F$ NMR shifts were referenced externally to hexafluorobenzene at −164.9 ppm. All infrared spectra were taken on a PerkinElmer Spectrum One FT-IR spectrometer, recorded as KBr pellets.

Elemental analyses were performed at the University of California, Berkeley Microanalytical Facility, using a PerkinElmer Series II 2400 CHNS analyzer.

**Synthesis of KP(Mes)(SiMe$_3$).** In a scintillation vial charged with benzylpotassium (182 mg, 1.4 mmol), toluene (5 mL), and a magnetic stir bar, HP(Mes)(SiMe$_3$) (313 mg, 1.4 mmol) was added at room temperature. The suspension was stirred at room temperature for 48 hours. The solution was then filtered through Celite to yield a yellow solution. The solvent was removed in vacuo to yield KP(C$_6$H$_2$Me$_3$-2,4,6)(SiMe$_3$) as a yellow powder (196 mg, 54%). $^1$H NMR (C$_6$D$_6$, 600 MHz, 298 K): δ 6.92 (s, 2H, *m*-Mes), 2.57 (s, 6H, C*H*$_3$-*o*-Mes), 2.14 (s, 3H, C*H*$_3$-*p*-Mes), 0.29 (d, 9H, $^3J_{H–P}$ = 4.2 Hz, -Si(C*H*$_3$)$_3$). $^{13}$C{$^1$H} NMR (C$_6$D$_6$, 150 MHz): δ 145.1 (d, $^2J_{C–P}$ = 4.5 Hz, *o*-Mes), 143.0 (d, $^2J_{C–P}$ = 45 Hz, *ipso*-Mes), 132.9 (*p*-Mes), 128.8 (*m*-Mes), 27.9 (d, $^2J_{C–P}$ = 10.5 Hz, *C*H$_3$-*o*-Mes), 20.9 (*p*-Mes), 5.5 (d, $^2J_{C–P}$ = 12 Hz, -Si(*C*H$_3$)$_3$). $^{31}$P{$^1$H} NMR (C$_6$D$_6$, 121 MHz): δ −180.2. $^{29}$Si INEPT NMR (C$_6$D$_6$, 60 MHz): δ 2.14 (d, $^1J_{Si–P}$ = 47.9 Hz, -*Si*(CH$_3$)$_3$).

**Synthesis of (C$_5$Me$_5$)$_2$Th(Cl)[P(Mes)$_2$], 1.** In a scintillation vial, K[P(Mes)$_2$] (118 mg, 0.38 mmol) in Et$_2$O (10 mL) was added to (C$_5$Me$_5$)$_2$ThCl$_2$ (220 mg, 0.38 mmol) in Et$_2$O (10 mL) and the mixture stirred for 2 hours at room temperature. The resulting red-purple solution was filtered over a plug of Celite, and the volatiles were removed in vacuo to yield a red-purple solid (172 mg, 56%). X-ray-quality crystals were grown from a concentrated diethyl ether solution at −35 °C. $^1$H NMR (C$_6$D$_6$, 500 MHz, 298 K): δ 6.93 (s, 4H, m-Mes), 2.63 (s, 12H, o-Mes), 2.18 (s, 6H, p-Mes), 2.01 (s, 30H, C$_5$Me$_5$). $^{13}$C{$^1$H} NMR (C$_6$D$_6$, 125 Hz, 298 K): 144.1 (d, $^2$J$_{P–C}$ = 7.9 Hz), 139.7, 136.1, 129.3 (d, $^3$J$_{P–C}$ = 5.2 Hz), 128.7, 25.8 (d, $^3$J$_{P–C}$ = 10.4 Hz), 21.0, 11.9. $^{31}$P{$^1$H} NMR (C$_6$D$_6$, 120 MHz): δ 114.8. IR (KBr, cm$^{-1}$): 2965 (s), 2917 (s), 2856 (s), 1606 (m), 1445 (s), 1378

(m), 1262 (m), 1085 (s), 1031 (s), 952 (w), 848 (s), 802 (m), 654 (w). UV−vis (0.25 mM, toluene): 534 nm, ε = 375 $M^{-1}$ $cm^{-1}$. Despite multiple attempts, a satisfactory elemental analysis could not be obtained due to the similar solubilities of **1** and $HPMes_2$.

**Synthesis of $(C_5Me_5)_2Th[P(Mes)(CH_3)]_2$, 2**. In a scintillation vial, $(C_5Me_5)_2ThCl_2$ (140 mg, 0.24 mmol) in toluene was added to $KP(Mes)(CH_3)$ (100 mg, 0.49 mmol) in toluene and the mixture stirred overnight at room temperature. The formation of a precipitate was observed immediately following the addition. The resulting deep red-purple solution was filtered over a plug of Celite, and the volatiles were removed in vacuo to yield a red-purple solid (168 mg, 83%). X-ray-quality crystals were grown from a concentrated diethyl ether solution at −35 °C. $^1$H NMR ($C_6D_6$, 600 MHz, 298 K): δ 7.08 (s, 4H, *m*-Mes), 2.86 (s, 12H, *o*-Mes), 2.33 (d, 6H, $^2J_{H–P}$ = 5.4 Hz, P-*Me*), 2.24 (s, 6H, *p*-Mes), 2.07 (s, 30H, $C_5Me_5$). $^{13}C\{^1H\}$ NMR ($C_6D_6$, 150 Hz, 298 K): 144.1, 142.8, 129.0, 126.0, 25.0 (dd, $J_{P–C}$ = 4.0 Hz, $J_{P–C}$ = 5.2 Hz), 21.2, 15.2 (d, $^1J_{P–C}$ = 6 Hz), 11.6. $^{31}P\{^1H\}$ NMR ($C_6D_6$, 120 MHz): δ 117.5. IR (KBr, $cm^{-1}$): 2972 (m), 2954 (s), 2893 (vs), 2856 (s), 1599 (w), 1484 (w), 1448 (s), 1347 (s), 1289 (w), 1262 (w), 1118 (w), 1053 (w), 1021 (m), 886 (m), 844 (s), 821 (w), 716 (w), 683 (w), 616 (w), 608 (w), 552 (w). UV–vis (0.25 mM, toluene): 533 nm, ε = 260 $M^{-1}$ $cm^{-1}$. Anal. Calcd for $C_{40}H_{58}P_2Th$: C, 57.68; H, 7.02. Found: C, 57.32; H, 7.13.

**Synthesis of $(C_5Me_5)_2Th(CH_3)OTf$, 3**. In the absence of light, AgOTf (117 mg, 0.46 mmol) in THF (5 mL) was added to $(C_5Me_5)_2Th(CH_3)_2$ (243 mg, 0.46 mmol) in THF (5 mL) and stirred overnight. The resulting dark gray suspension was filtered over a plug of Celite, and the volatiles were removed in vacuo to yield a white solid (264 mg, 87%). X-ray-quality crystals were grown from a concentrated toluene solution at −35 °C. $^1$H NMR

($C_6D_6$, 600 MHz, 300 K): δ 2.05 (s, 30H, $C_5Me_5$), 0.52 (s, 3H, Th-*Me*). $^{13}C\{^1H\}$ NMR ($C_6D_6$, 150 MHz, 300 K): δ 125.9, 68.6, 11.6; the *C*$F_3$ resonance could not be located. $^{19}F$ NMR ($C_6D_6$, 283 MHz, 300 K): δ −71.2. IR (KBr, $cm^{-1}$): 2917 (m), 2867 (m), 1440 (w), 1382 (w), 1314 (m), 1252 (s), 1217 (vs), 1122 (w), 1020 (vs), 805 (w), 629 (m). This compound has been previously reported but with triflic acid.[192,193]

**Synthesis of $(C_5Me_5)_2Th(CH_3)[P(Mes)_2]$, 4**. A 20 mL scintillation vial was charged with $(C_5Me_5)_2Th(CH_3)Cl$ (330 mg, 59.8 mmol) and toluene (3 mL) and placed in a −25 °C freezer to cool for 30 min. A second vial was charged with $KPMes_2$ (184 mg, 59.8 mmol). The $KPMes_2$ as a solid was then transferred to the cooled solution of $(C_5Me_5)_2Th(CH_3)Cl$, with about 5 mL of toluene. The reaction mixture was stirred for about 1.5 h, resulting in a cloudy red solution. The volatiles were removed under reduced pressure. The resulting red-purple crude solid was triturated in diethyl ether and filtered over Celite to remove any free phosphine generated. The remaining solid was then washed through the filter using toluene, until the red-purple solution ran clear, leaving a yellow solid behind ($KPMes_2$). The toluene solution was concentrated and layered with pentane. From the layered solution, a red-purple solid (127 mg, 47% yield) deposited out overnight. Through subsequent recrystallizations, more material was able to be isolated. $^1H$ NMR (600 MHz, $C_6D_6$): δ 6.92 (s, 4H, *m*-Mes), 2.54 (s, 12H, *o*-Mes), 2.18 (s, 6H, *p*-Mes), 1.93 (s, 30H, $C_5(CH_3)_5$), 0.41 (s, 3H, Th-$CH_3$). $^{13}C\{^1H\}$ NMR ($C_6D_6$, 150 MHz): δ 143.54 (d, $^1J_{C–P}$ = 9 Hz, P–$C_{–Mes}$), 140.88 (d, $^2J_{C–P}$ = 1.5 Hz, $ArC_{–ortho}$), 135.43 (s, $ArC_{–para}$), 129.18 (d, $^3J_{C–P}$ = 4.5 Hz, $ArC_{–meta}$) 125.13 (s, $C_5(CH_3)_5$), 72.77 (s, Th-$CH_3$), 25.68 (d, $^3J_{C–P}$ = 10.5 Hz, Mes-$CH_{3\text{-ortho}}$), 21.04 (s, Mes-$CH_{3\text{-para}}$), 11.59 (s, $C_5(CH_3)_5$). $^{31}P\{^1H\}$ NMR ($C_6D_6$, 120 MHz): δ 105.3. IR (KBr, $cm^{-1}$): 2971 (s), 2909 (vs), 2861 (s), 1601 (w),

1546 (w), 1462 (w), 1446 (vs), 1396 (w), 1396 (w), 1373 (m), 1290 (w), 1260 (w), 1176 (w), 1108 (m), 1087 (w), 1050 (w), 1030 (m), 1018 (w), 950 (w), 847 (vs), 801 (w), 711 (w), 618 (w), 556 (m), 545 (w), 517 (w). UV–vis (0.6 mM, toluene): 525 nm, ε = 640 $M^{-1}$ $cm^{-1}$. Anal. Calcd for $C_{39}H_{55}PTh$: C, 59.53; H, 7.05. Found: C, 59.40; H, 7.11.

**Synthesis of $(C_5Me_5)_2Th(CH_3)[P(Mes)(SiMe_3)]$, 5**. In a scintillation vial, $KP(Mes)(SiMe_3)$ (79 mg, 0.3 mmol) in toluene (5 mL) was added to $(C_5Me_5)_2Th(CH_3)OTf$ (201 mg, 0.3 mmol) in toluene (5 mL) and the mixture stirred overnight at room temperature. The resulting orange solution was filtered over a plug of Celite, and the volatiles were removed in vacuo to yield an orange solid (169 mg, 76%). X-ray-quality crystals were grown from a concentrated diethyl ether solution at −35 °C. $^1H$ NMR ($C_6D_6$, 600 MHz, 300 K): δ 7.04 (s, 2H, *m*-Mes), 2.80 (s, 6H, *o*-Mes), 2.22 (s, 3H, *p*-Mes), 1.99 (s, 30H, $C_5Me_5$), 0.43 (s, 3H, Th-*Me*), 0.39 (d, 9H, $^2J_{H-P}$ = 4.8 Hz, Si*Me*$_3$). $^{13}C\{^1H\}$ NMR ($C_6D_6$, 150 MHz, 300 K): 144.9 (d, $^2J_{C-P}$ = 5.1 Hz), 137.3 (d, $^1J_{C-P}$ = 9.45 Hz), 135.3, 128.5 (d, $^3J_{P-C}$ = 4.2 Hz), 125.2, 71.3, 27.5 (d, $^3J_{P-C}$ = 9.15 Hz), 21.1, 11.7, 4.57 (d, $^2J_{P-C}$ = 11.4 Hz). $^{31}P\{^1H\}$ NMR ($C_6D_6$, 120 MHz): δ 11.9. $^{29}Si$ INEPT NMR ($C_6D_6$, 60 MHz): δ 6.44 (d, $^1J_{Si-P}$ = 7.8 Hz). IR (KBr, $cm^{-1}$): 2968 (s), 2944 (s), 2909 (vs), 2859 (s), 1488 (w), 1437 (m), 1377 (m), 1237 (s), 1106 (m), 1044 (m), 1022 (m), 948 (w), 836 (vs), 747 (w), 677 (w), 629 (m). UV–vis (0.10 mM, toluene): 455 nm, ε = 285 $M^{-1}$ $cm^{-1}$. Anal. Calcd for $C_{33}H_{53}PSiTh$: C, 53.50; H, 7.21. Found: C, 52.56; H, 7.05.

**Synthesis of $(C_5Me_5)_2Th[P(Mes)(SiMe_3)]_2$, 6 and $(C_5Me_5)_2Th(Cl)[P(Mes)(SiMe_3)]$, 7**. $KP(Mes)(SiMe_3)$ (92 mg, 0.35 mmol) in toluene (5 mL) was added to $(C_5Me_5)_2ThCl_2$ (100 mg, 0.17 mmol) in toluene (5 mL) and the mixture stirred overnight. The resulting

orange solution was filtered over a plug of Celite, and the volatiles were removed in vacuo to yield a tacky orange solid (117 mg). $^{31}$P NMR shows that the crude material contains both $(C_5Me_5)_2Th(Cl)[P(Mes)(SiMe_3)]$ and $(C_5Me_5)_2Th[P(Mes)(SiMe_3)]_2$ (9:1 ratio). Recrystallization from DME yielded a small quantity of X-ray-quality crystals of $(C_5Me_5)_2Th[P(C_6H_2Me_3\text{-}2,4,6)(SiMe_3)]_2$ (**6**). $^1$H NMR ($C_6D_6$, 600 MHz, 298 K): δ 7.11 (s, 4H, *m*-Mes), 2.86 (s, 12H, *o*-Mes), 2.25 (s, 6H, *p*-Mes), 2.09 (s, 30H, $C_5\mathit{Me}_5$), 0.51 (br-s, 18H). $^{13}$C{$^1$H} NMR ($C_6D_6$, 150 Hz, 298 K): 145.4, 138.2 (d, $^1J_{C–P}$ = 7.5 Hz), 135.8, 128.8, 128.1, 27.6, 21.1, 12.3, 4.37 (t, $^2J_{C–P}$ = 6 Hz) . $^{31}$P{$^1$H} NMR ($C_6D_6$, 120 MHz): δ 48.5. $^{29}$Si INEPT NMR ($C_6D_6$, 60 MHz): δ 7.14 (t, $^1J_{Si–P}$ = 1.9 Hz). UV–vis (0.25 mM, toluene): 490 nm, ε = 390 $M^{-1}$ $cm^{-1}$. Recrystallization from $Et_2O$ yielded a small quantity of X-ray-quality crystals of $(C_5Me_5)_2Th(Cl)[P(Mes)(SiMe_3)]$ (**7**). $^1$H NMR ($C_6D_6$, 600 MHz, 298 K): δ 7.04 (s, 2H, *m*-Mes), 2.80 (s, 6H, *o*-Mes), 2.21 (s, 3H, *p*-Mes), 2.06 (s, 30H, $C_5\mathit{Me}_5$), 0.43 (d, 9H, $^2J_{H–P}$ = 4.8 Hz). $^{13}$C{$^1$H} NMR ($C_6D_6$, 150 Hz, 298 K): 145.0 (d, $^1J_{C–P}$ = 4.5 Hz), 137.3 (d, $^2J_{C–P}$ = 4.5 Hz), 135.69, 128.6 (d, $^3J_{C–P}$ = 4.5 Hz), 128.2, 24.5, 21.1, 12.0, 4.6 (d, $^2J_{C–P}$ = 10.5 Hz). $^{31}$P{$^1$H} NMR ($C_6D_6$, 120 MHz): δ 24.8. $^{29}$Si INEPT NMR ($C_6D_6$, 60 MHz): δ 6.56 (d, $^1J_{Si–P}$ = 6 Hz). Despite multiple attempts, a satisfactory elemental analysis could not be obtained due to the similar solubilities of $(C_5Me_5)_2Th(Cl)[P(Mes)(SiMe_3)]$ and $(C_5Me_5)_2Th[P(Mes)(SiMe_3)]_2$.

**Computational Details**

Theoretical calculations were carried out with Kohn–Sham density functional theory (KS-DFT) using the Amsterdam Density Functional (ADF2017) package.[194,195] The scalar zeroth-order regular approximation (ZORA) relativistic Hamiltonian[196] and the Perdew, Burke, and Ernzerhof (PBE) functional[197] and TZP Slater-type basis sets[198] with

small frozen cores were used for geometry optimizations. Due to the charge transfer like nature of valence excitations, the Coulomb attenuated method Becke three-parameter Lee, Yang, and Parr (CAM-B3LYP) functional[199] was employed for excitation spectra simulations using time-dependent DFT (TD-DFT) linear response calculations.

**Crystal Structure Determination and Refinement**

Selected single crystals of **1**–**7** were mounted on nylon cryoloops using viscous hydrocarbon oil. X-ray data collection was performed at 100(2) or 150(2) K. The X-ray data were collected on a Bruker CCD diffractometer with monochromated Mo Kα radiation (λ = 0.71073 Å). The data collection and processing utilized the Bruker Apex2 suite of programs.[32] The structures were solved using direct methods and refined by full-matrix least-squares methods on $F^2$ using the Bruker SHELX-97 program.[33] All non-hydrogen atoms were refined with anisotropic displacement parameters. All hydrogen atoms were placed at calculated positions and included in the refinement using a riding model. Thermal ellipsoid plots were prepared by using Olex2[34] with 50% probability displacements for non-hydrogen atoms. Crystal data and details of data collection for complexes **1**–**7** are provided in Table A-1.

**Table A-1.** X-ray crystallography data is shown for complexes **1-7**.

| **Complex** | **1** | **2** | **3** | **4** |
|---|---|---|---|---|
| CCDC deposit number | 1834568 | 1834569 | 1834570 | 1834571 |
| Empirical formula | $C_{38}H_{52}ClPTh$ | $C_{40}H_{58}P_2Th$ | $C_{51}H_{74}F_6O_6S_2Th_2$ | $C_{39}H_{55}PTh$ |
| Formula weight (g/mol) | 807.25 | 832.84 | 1425.3 | 786.84 |
| Crystal habit, color | Prism, Red | Prism, Red | Prism, Colorless | Plate, Pink |
| Temperature (K) | 100(2) | 100(2) | 100(2) | 100(2) |

| Space group | $P2_1/n$ | C2/c | $P2_1/c$ | $P12_1/n1$ |
|---|---|---|---|---|
| Crystal system | Monoclinic | Monoclinic | Monoclinic | Monoclinic |
| Volume ($Å^3$) | 3411.4(8) | 4216.8(11) | 5329.9(10) | 3441.3(6) |
| a (Å) | 11.7219(15) | 17.321(3) | 11.6583(12) | 11.6978(11) |
| b (Å) | 20.910(3) | 13.840(2) | 25.044(3) | 20.919(2) |
| *c* (Å) | 14.0570(18) | 17.800(3) | 19.140(2) | 14.2090(13) |
| $\alpha$ (˚) | 90° | 90° | 90° | 90° |
| $\beta$ (˚) | 98.072(2)° | 98.821(2)° | 107.4960(10)° | 98.2090(10)° |
| $\gamma$ (˚) | 90° | 90° | 90° | 90° |
| Z | 4 | 4 | 4 | 4 |
| Calculated density ($Mg/m^3$) | 1.572 | 1.312 | 1.776 | 1.519 |
| Absorption coefficient ($mm^{-1}$) | 4.521 | 3.635 | 5.719 | 4.404 |
| Final R indices [I > 2σ(I)] | R1 = 0.0368, wR2 = 0.0840 | R1 = 0.0439, wR2 = 0.1066 | R1 = 0.0213, wR2 = 0.0454 | R1 = 0.0204, wR2 = 0.0451 |

| **Complex** | **5** | **6** | **7** |
|---|---|---|---|
| CCDC deposit number | 1834572 | 1834574 | 1834573 |
| Empirical formula | $C_{33}H_{53}PSiTh$ | $C_{44}H_{70}P_2Si_2Th$ | $C_{32}H_{50}ClPSiTh$ |
| Formula weight (g/mol) | 740.85 | 949.16 | 761.27 |
| Crystal habit, color | Prism, Yellow | Prism, Orange | Plate, Orange |
| Temperature (K) | 100(2) | 100(2) | 100(2) |
| Space group | P-1 | C2/c | P-1 |
| Crystal system | Triclinic | Monoclinic | Triclinic |
| Volume ($Å^3$) | 3274.8(5) | 4506.8(2) | 3239.3(6) |
| a (Å) | 9.4091(8) | 15.4033(4) | 9.4027(9) |
| b (Å) | 14.9346(13) | 18.6254(5) | 14.8838(15) |
| *c* (Å) | 23.706(2) | 15.7119(4) | 23.531(2) |
| $\alpha$ (˚) | 89.868(2)° | 90° | 90.122(2)° |
| $\beta$ (˚) | 87.257(2)° | 91.091(2)° | 93.183(2)° |
| $\gamma$ (˚) | 79.804(2)° | 90° | 99.858(2)° |

| Z | 4 | 4 | 4 |
|---|---|---|---|
| Calculated density ($Mg/m^3$) | 1.503 | 1.399 | 1.561 |
| Absorption coefficient ($mm^{-1}$) | 4.658 | 12.044 | 4.791 |
| Final R indices [$I > 2\sigma(I)$] | R1 = 0.0369, wR2 = 0.0545 | R1 = 0.0226, wR2 = 0.0570 | R1 = 0.0173, wR2 = 0.0444 |

**Results and Discussion**

Reaction of $(C_5Me_5)_2ThCl_2$ with $KP(Mes)_2$ results in an immediate color change from colorless to dark purple. The $^1H$ NMR spectrum of the reaction indicated the product as $(C_5Me_5)_2Th(Cl)[P(Mes)_2]$ (**1**; Figure A-1), with coordination of only one phosphido ligand. Allowing the reaction to proceed for more than 2–3 h produces large amounts of phosphine and the coupled phosphido species $Mes_2PPMes_2$,[200] which is observed in the $^{31}P$ NMR spectrum. The reaction with 2 equiv of $KP(Mes)_2$ does not yield the bis(phosphido) complex, presumably due to the steric properties of the phosphido ligand. We note that $(C_5H_5)_2Zr(AsMes_2)_2$ is known,[201] but this is most likely due to the use of $(C_5H_5)^-$ instead of $(C_5Me_5)^-$ as well as arsenic being much larger than phosphorus, producing longer Zr–As bonds. When the steric properties are decreased using $KP[(Mes)(CH_3)]$, the bis(phosphido) complex $(C_5Me_5)_2Th[P(Mes)(CH_3)]_2$ (**2**) can be isolated (Figure A-2). Complex **2** is also dark red-purple. This is in contrast to our previously reported bis(phosphido) complex $(C_5Me_5)_2Th[PH(Mes)]_2$, which is pale yellow. Hence, the substituents on phosphorus make a large difference in the electronic

structure of the thorium complex.

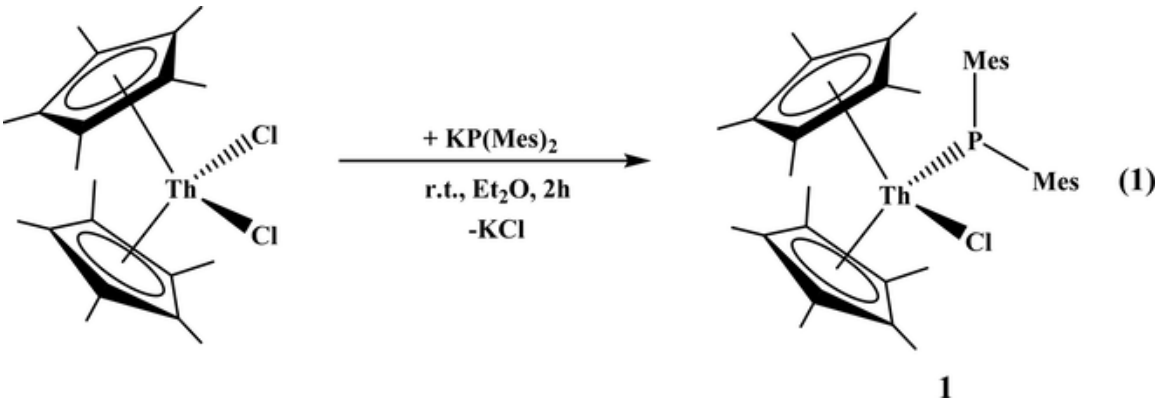


**Figure A-1**. Reaction scheme of $(C_5Me_5)_2ThCl_2$ with $KP(Mes)_2$ in $Et_2O$.

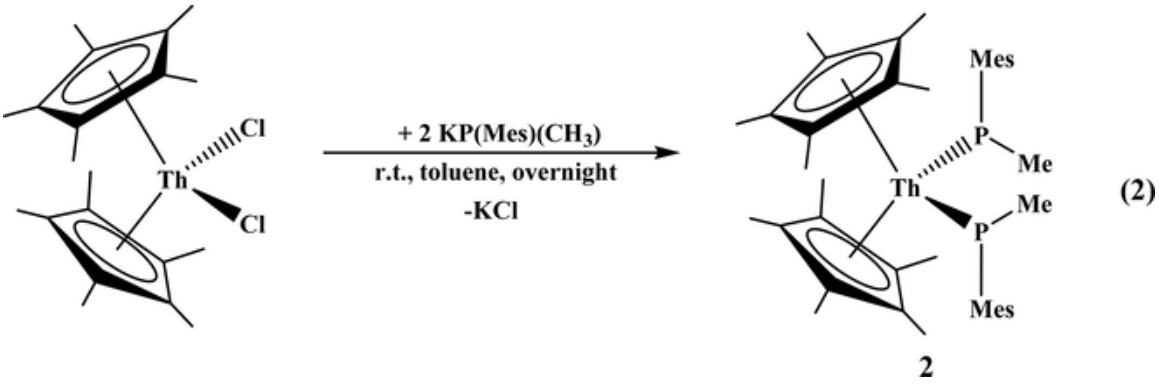


**Figure A-2**. Reaction scheme of $(C_5Me_5)_2ThCl_2$ with $KP(Mes)(CH_3)$ in toluene.

Next, we attempted to replace the chloride with a methyl group to see if any effect was observed. For this, $[(C_5Me_5)_2Th(CH_3)(OTf)]_2$ (**3**; OTf = $OSO_2CF_3$) was used. Complex **3** can be made in a way analogous to that for the uranium complex through the reaction of $(C_5Me_5)_2Th(CH_3)_2$ with AgOTf.[202] Complex **3** is isostructural with the uranium analogue $[(C_5Me_5)_2U(CH_3)(OTf)]_2$.[203] Reaction of **3** or $(C_5Me_5)_2Th(CH_3)Cl$ with $KP(Mes)_2$ produced a dark red-purple solution for which the product was identified as $(C_5Me_5)_2Th(CH_3)[P(Mes)_2]$ (**4**; Figure A-3). Next, we varied the phosphido ligand by

replacing the methyl with a silyl group. The reaction of **3** with KP[(SiMe$_3$)(Mes)] produces an orange solution of (C$_5$Me$_5$)$_2$Th(CH$_3$)[P(SiMe$_3$)(Mes)] (**5**), not dark purple.

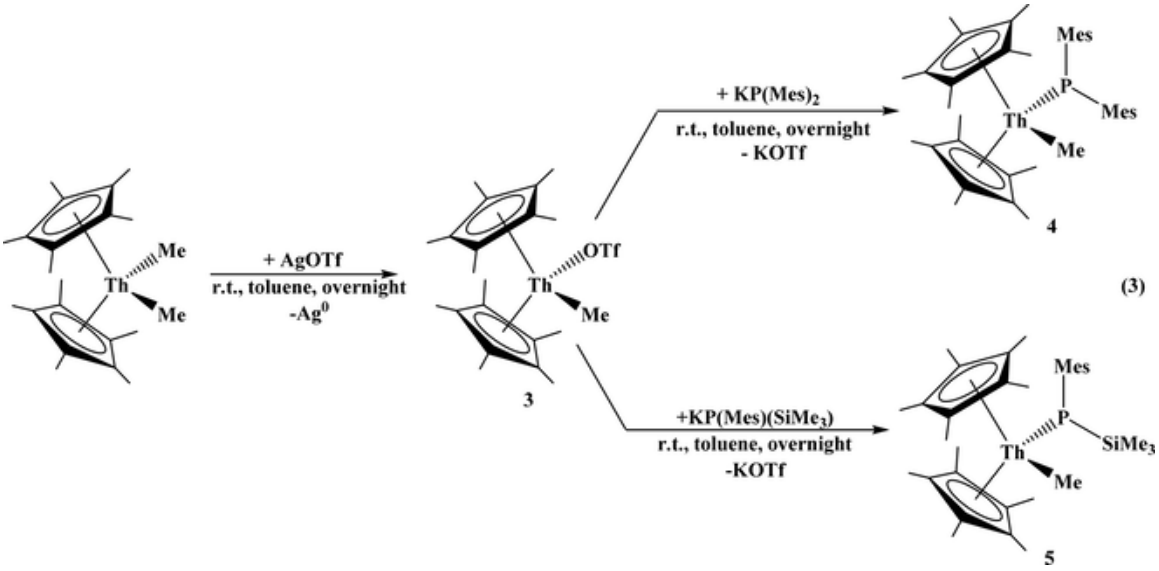


**Figure A-3.** Reaction scheme of (C$_5$Me$_5$)$_2$Th(CH$_3$)Cl with KP(Mes)$_2$ and with . KP(Mes)(SiMe$_3$).

To probe this further, (C$_5$Me$_5$)$_2$Th[P(Mes)(SiMe$_3$)]$_2$ (**6**) and (C$_5$Me$_5$)$_2$Th(Cl)[P(Mes)(SiMe$_3$)] (**7**) were both made upon reaction of (C$_5$Me$_5$)$_2$ThCl$_2$ with 2 equiv of K[P(Mes)(SiMe$_3$)] (Figure A-4). Both of these complexes are also orange. We found that the reaction favors **7**; however, approximately 10% of the product is **6** and could not be separated except by crystallization. Using 1 equiv or slightly less than 1 equiv produces **7**, however, remaining (C$_5$Me$_5$)$_2$ThCl$_2$ is observed, which was not

easily removed due to its solubility being similar to that of **7**.

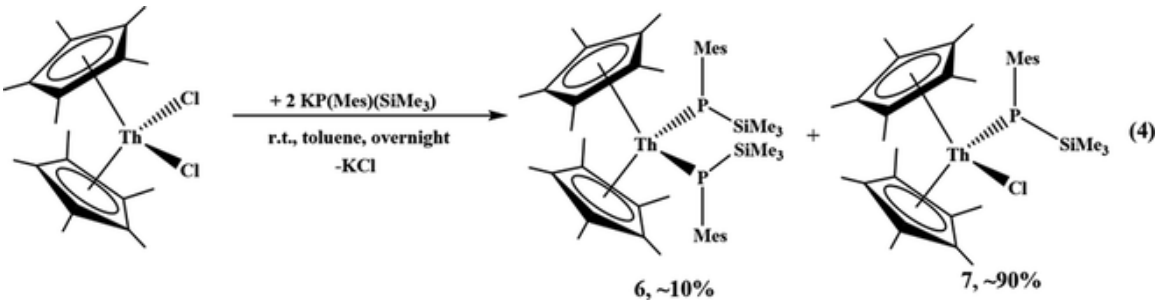


**Figure A-4.** Reaction scheme of $(C_5Me_5)_2ThCl_2$ with 2 equivalents of K[P(Mes)($SiMe_3$)].

## Structural Analysis

Complexes **1-7** were structurally characterized using single-crystal X-ray diffraction analysis. All phosphido complexes are monomeric with a pseudotetrahedral geometry featuring two $(C_5Me_5)^-$ ligands and one or two phosphido groups. Selected bond distances and angles can be found in Table A-2. All thorium–phosphorus bond distances are in the range of 2.7872(15)–2.8713(12) Å, and most are within the sum of the ionic radii for a thorium–phosphorus single bond of 2.86 Å.[204] These bond lengths are typical in metallocene complexes, as 2.861(7) and 2.887(8) Å are observed in $(C_5Me_5)_2Th(PPh_2)_2$[177] and 2.888(4) Å in $(C_5Me_5)_2Th(CH_3)[P(SiMe_3)_2]$.[183]

**Table A-2.** Selected bond distances (Å) and angles (deg) for complexes **1**, **2**, and **4**–**7.**

| **Bond distance/angle** | **1, E = Cl** | **2, E = P** | **4, E = $CH_3$** | **5, E = $CH_3$** | **6, E = Cl** | **7, E = P** |
|---|---|---|---|---|---|---|
| Th–P | 2.8525(14) | 2.7872(15) | 2.8682(8) | 2.8713(12) | 2.8472(8) | 2.8377(8) |
| Th-E | 2.6295(14) | 2.7872(15) | 2.472(3) | 2.473(4) | 2.6297(7) | 2.8376(8) |
| P–Th–E | 104.45(4) | 84.88(6) | 101.81(8) | 90.94(10) | 91.69(2) | 91.45(4) |

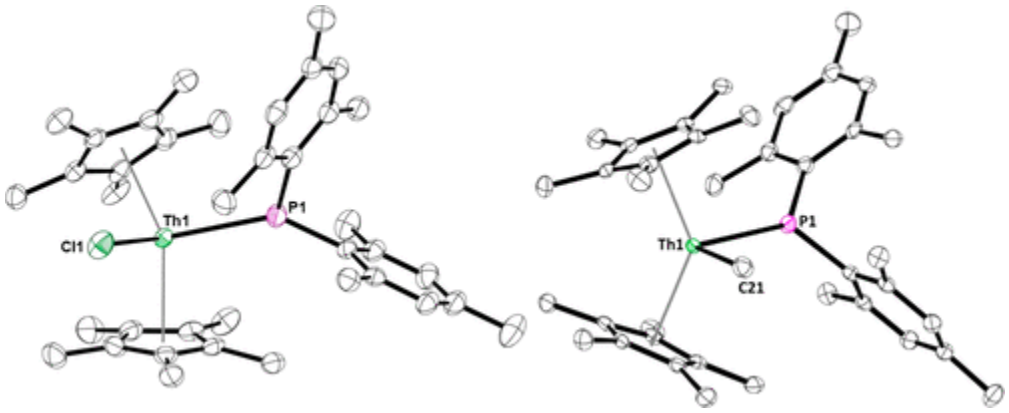


**Figure A-5.** Thermal ellipsoid plots of **1** (left) and **4** (right) shown at the 50% probability level. The hydrogen atoms have been omitted for clarity.

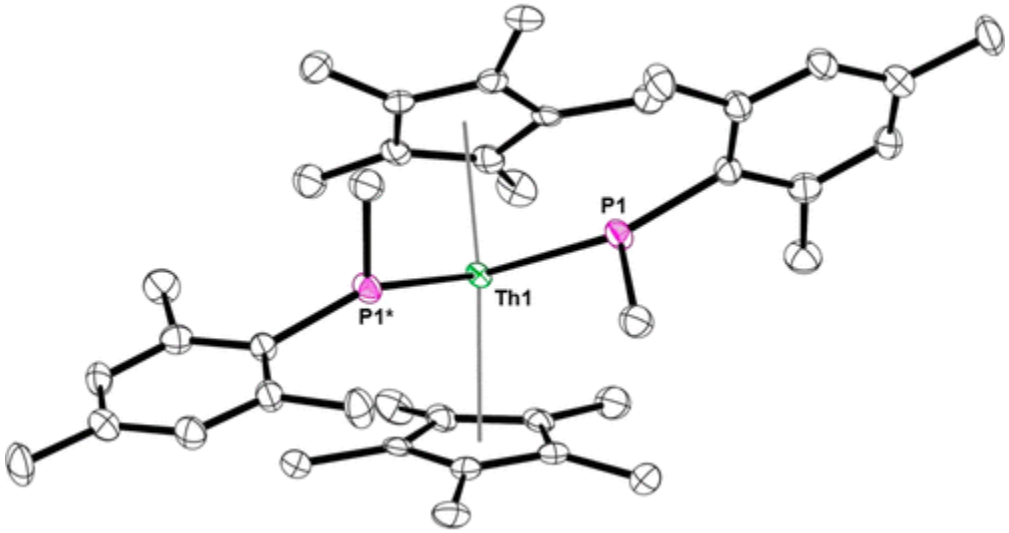


**Figure A-6.** Thermal ellipsoid plot of **2** shown at the 50% probability level. The hydrogen atoms have been omitted for clarity.

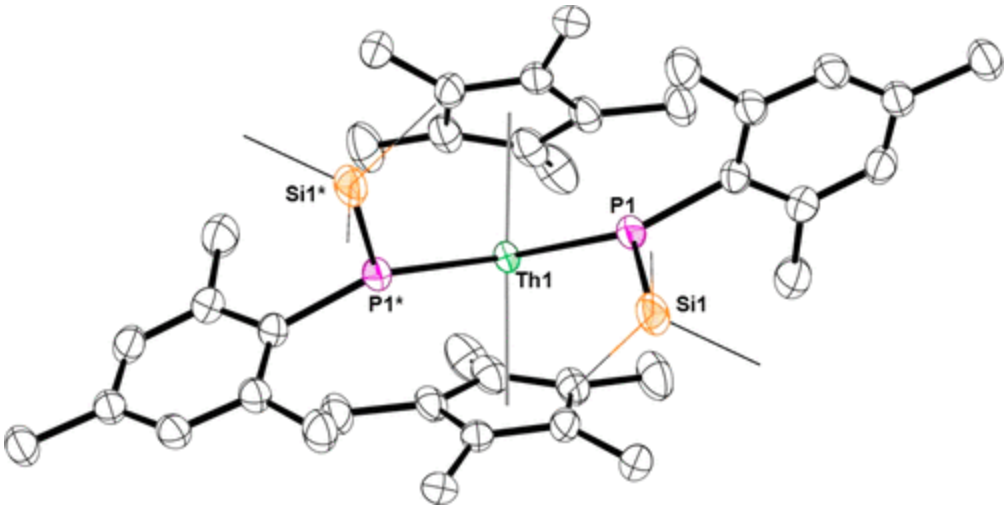


**Figure A-7.** Thermal ellipsoid plot of **6** shown at the 50% probability level. The hydrogen atoms have been omitted for clarity.

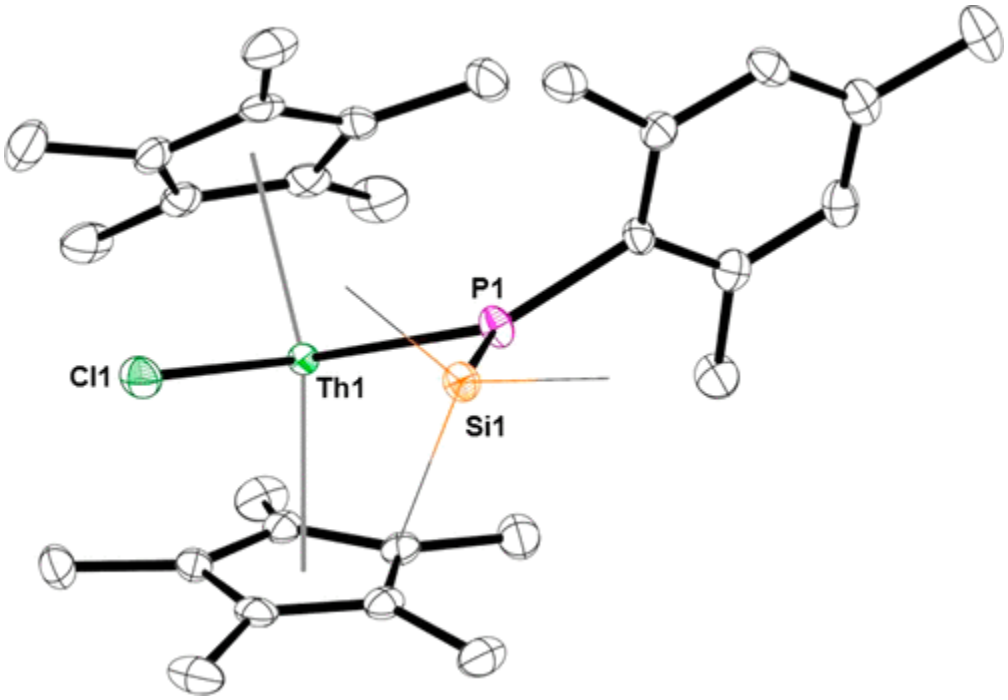


**Figure A-8.** Thermal ellipsoid plot of **7** shown at the 50% probability level. The hydrogen atoms have been omitted for clarity.

**Spectroscopy and TD-DFT Calculations**

We note that, in the $^{13}C$ NMR spectra, we observe coupling to the $^{31}P$ nuclei in some cases, but not all. There is currently no explanation for this. The $^{31}P$ NMR chemical shifts for each complex are given in Table A-3. A trend emerges from the data, with more electron donating groups causing $^{31}P$ shifts at lower frequency ("upfield", more shielded) while more withdrawing groups have $^{31}P$ signals at higher frequency ("downfield", less shielded). Resonances at 114.8, 117.5, 48.5, and 15.4 ppm were observed for $(C_5Me_5)_2ThX[P(Mes)(R)]$ (R = mesityl, methyl, silyl, and proton substituents, respectively). The difference in mesityl and methyl is likely due to a mono(phosphido)- versus bis(phosphido)-ligated complex. As such, a direct comparison could not be made, since we were unsuccessful in making $(C_5Me_5)_2Th[P(Mes_2)]_2$. Given this trend, the $^{31}P$ NMR shifts of $(C_5Me_5)_2Th(X)[P(SiMe_3)_2]$ (X = Cl and $CH_3$) were reported at +109.0 and +115.2 ppm, respectively,[183] but we found that these resonances are −109.0 and −115.2 ppm and have been corrected in Table A-4. This aligns nicely with the $^{31}P$ NMR signals for the recently reported $(Tren^R)Th[P(SiMe_3)_2]$ (Tren = $N(CH_2CH_2NR)_3$; R = DMBS = $Si^iPr_3$, −100.09 ppm; R = TIPS = $SiMe_2{}^tBu$, −66.45 ppm).[205] As the substituent on phosphorus becomes more donating, from mesityl to $SiMe_3$ to H, a shift to lower frequency is observed. For example, on comparison of $(C_5Me_5)_2Th(Cl)(PMes_2)$ (**1**), $(C_5Me_5)_2Th(Cl)[P(SiMe_3)(Mes)]$ (**7**), and $(C_5Me_5)_2Th(Cl)[P(SiMe_3)_2]$, the $^{31}P$ NMR resonances move from +114.8 to +24.8 to −109.0 ppm, respectively, by changing from two to one to zero aryl groups on the phosphido phosphorus and from zero to one to two silyl groups. This is also true of non-metallocene complexes such as $(Tren^{TIPS})ThPH_2$, which shows a $^{31}P$ NMR resonance at −144.08 ppm,[206] further upfield from the −66.45

ppm for ($Tren^{TIPS}$)Th[$P(SiMe_3)_2$]. Additionally, Th[$P(CH_2CH_2PMe_2)]_4$ has a $^{31}P$ NMR resonance at 83 ppm for the phosphido phosphorus,[207] which fits into our general scheme of the signal for a phosphido phosphorus with alkyl or aryl substituents being >75 ppm. When the phosphido phosphorus has one aryl or alkyl substituent with a more donating group such as silyl or hydrogen, then a shift to lower frequency is observed between −50 and 75 ppm. Two silyl groups or hydrogens on phosphorus are typically located <−50 ppm. These trends parallel the current literature, even with different ancillary ligands. By comparison, the bis(phosphido) complexes bis(NHC)borateTh$(PHMes)_2$ and $(C_5Me_5)_2$Th$(PHMes)_2$ have similar $^{31}P$ NMR chemical shifts at 21.7[208] and 15.4 ppm,[181] respectively. We also note that the $^{31}P$ NMR resonances for the phosphines also display a similar trend (Table A-3).

**Table A-3.** Summary of $^{31}P$ NMR chemical shifts (ppm) in $C_6D_6$.

| Phosphine | $^{31}P$ NMR Chemical Shift (ppm) in $C_6D_6$ |
|---|---|
| $HP(Mes)_2$ | -79.6 |
| $HP[(CH_3)(Mes)]$ | -105.6 |
| $HP[(SiMe_3)(Mes)]$ | -158.8 |
| HP[(H)(Mes)] | -155.4 |
| $HP(SiMe_3)_2$ | -236 |
| $HP(C_6H_5)_2$ | -27.1 |

The observation that more strongly electron donating substituents on phosphorus lead to lower frequency (upfield) $^{31}$P NMR signals, i.e. these P nuclei are more shielded, seems intuitive, although it is worthwhile reiterating that the nuclear magnetic shielding is not only related to the ground state electron density.[209]

**Table A-4.** $^{31}$P NMR Resonances for Metallocene Thorium Phosphido Complexes (Mes = $C_6H_2Me_3$-2,4,6).

| **Complex** | **$^{31}$P NMR resonance (ppm)** | **Color** | **Visible absorbance (nm)** |
|---|---|---|---|
| $(C_5Me_5)_2Th(Cl)[P(Mes)_2]$ (**1**) | 114.8 | red-purple | 534 |
| $(C_5Me_5)_2Th[P(Mes)(CH_3)]_2$ (**2**) | 117.5 | red-purple | 533 |
| $(C_5Me_5)_2Th(CH_3)[P(Mes)_2]$ (**4**) | 105.3 | red-purple | 525 |
| $(C_5Me_5)_2Th(CH_3)[P(Mes)(SiMe_3)]$ (**5**) | 11.9 | orange | 455 |
| $(C_5Me_5)_2Th[P(Mes)(SiMe_3)]_2$ (**6**) | 48.5 | orange | 490 |
| $(C_5Me_5)_2Th(Cl)[P(Mes)(SiMe_3)]$ (**7**) | 24.8 | orange | |
| $(C_5Me_5)_2Th[PH(Mes)]_2$ | 15.4 | yellow | 445 |
| $(C_5Me_5)_2Th(PPh_2)_2$ | 144 | purple | 570, 498 |
| $(C_5Me_5)_2Th[P(Et)_2]_2$ | 136 | purple | |
| $(C_5Me_5)_2Th(Cl)[P(SiMe_3)_2]$ | –109.0[a] | yellow | |
| $(C_5Me_5)_2Th(CH_3)[P(SiMe_3)_2]$ | –115.2[a] | yellow | |

[a]Corrected from ref 183.

A trend is also reflected in the observed colors of aryl- versus silyl- or hydrogen-substituted phosphido ligands (Table A-4). The electronic absorption spectra of complexes **1**, **2**, and **4** have absorption maxima of 525–535 nm; hence, a red-violet color is observed. However, when the substituent is a hydrogen or silyl, then absorption maxima are found between 440 and 500 nm. This corresponds to a yellow to yellow-orange color. Again, this fits with other substituted phosphido ligands with non-metallocene frameworks. For example, $(Tren^{TIPS})ThPH_2$ is colorless,[206] $Th[P(CH_2CH_2PMe_2)]_4$ is an intense red,[207] and $(BIMA)_3Th(PHMes)$ is yellow, while $(BIMA)_3Th(PPh_2)$, BIMA = $MeC(N^iPr)_2$, is bright orange.[210]

DFT and TDDFT calculations were performed on the complexes $(C_5Me_5)_2Th[PH(Mes)]_2$ (referred to as $Th[PH(Mes)]_2$), $(C_5Me_5)_2Th(Cl)(PMes_2)$ (**1**), $(C_5Me_5)_2Th[P(CH_3)(Mes)]_2$ (**2**), $(C_5Me_5)_2Th(CH_3)[P(Mes)(SiMe_3)]$ (**5**), and $(C_5Me_5)_2Th[P(SiMe_3)(Mes)]_2$ (**6**) to explore their electronic structure. The thorium–ligand bond lengths as well as nearest-neighbor atom bond lengths and Cp–Cp plane angles are reproduced well in the optimized geometries. An overview of the electronic structure of the complexes is detailed in the molecular orbital (MO) diagram of Figure A-9. The MO levels correspond to the energy scale on the left of the figure and inlaid for the complexes are isosurfaces (±0.03 atomic units) of the highest occupied MO (HOMO) and lowest unoccupied MO (LUMO).

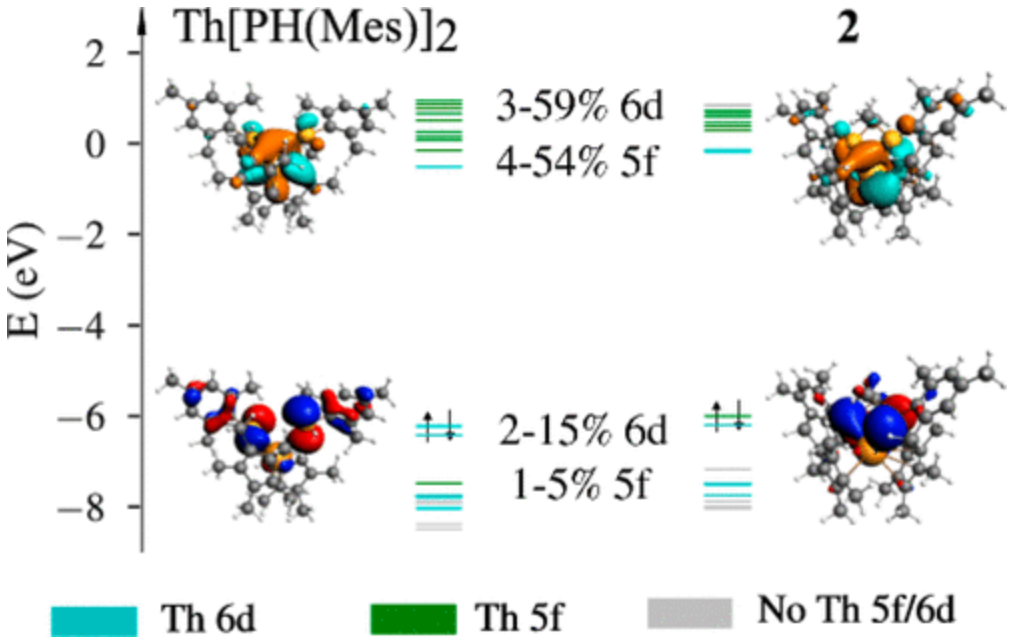


**Figure A-9.** Molecular orbital (MO) diagram of $(C_5Me_5)_2Th[PH(Mes)]_2$ (left) and $(C_5Me_5)_2Th[P(CH_3)(Mes)]_2$ (**2**) (right). Orbital energy levels are colored according to the largest contribution of Th 5f or 6d in a given MO. Inlaid are isosurfaces (±0.03) of the HOMO (below) and the LUMO (above). An MO diagram of all complexes and a table of numerical values used in generating this plot can be found in Figure A-10.

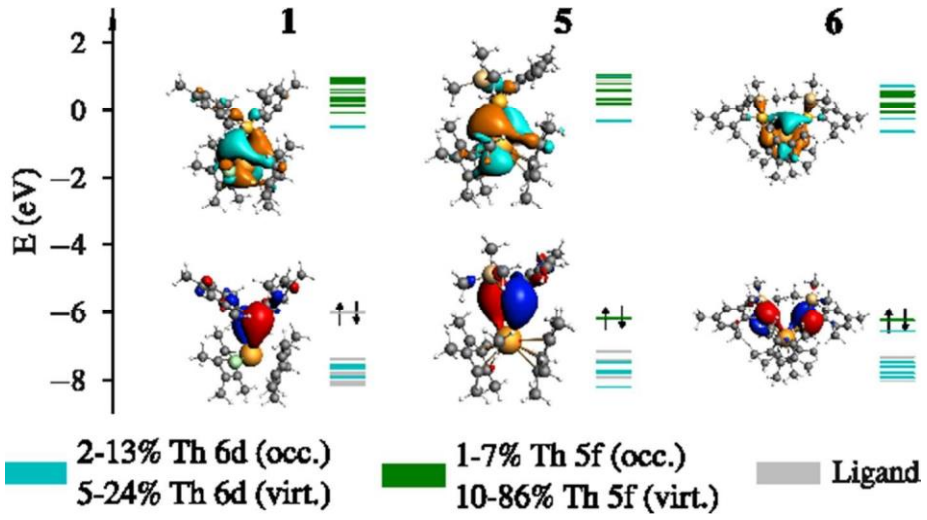


**Figure A-10.** MO diagrams of **1**, **5**, and **6**. Overall the character of the orbitals follows the same trend as established in the main document; nonnegligible mixing with Th 6d in the occupied frontier orbitals and primarily Th 6d and 5f virtual frontier orbitals.

The HOMO for all complexes is dominantly phosphorus 3p with very little thorium mixing. In the case of the bis(phosphido) complexes, HOMO-1 is of similar character. The doubly substituted phosphidos exhibit larger 5f contribution in the HOMO, whereas the primary substituted phosphido shows larger 6d contribution in the HOMO. In the case of direct Cl ligation, Th mixing is negligible. Below the HOMO, there are numerous delocalized Cp and mesityl π orbitals. For all complexes, the LUMO is primarily Th 6d in character, with orbitals above the LUMO consisting heavily of significant mixes of Th 5f, 6d, and 7s. In a further examination of the bonding, as the principal quantum number increases down a group, typically an increase in the mixing of actinide and ligand orbitals is observed. Upon comparison of complex **1** with the nitrogen analogue $(C_5Me_5)_2Th(Cl)[N(Mes)_2]$, natural bond order (NBO) analysis does indicate an increase

in covalent character in the thorium–phosphorus bond in comparison to the thorium–nitrogen bond (Table A-5). This is due to the energetics of the 2p of N versus 3p of P in relation to the 5f orbitals of thorium.

**Table A-5.** Natural bonding orbitals (NBOs) in **1** and a nitrogen-substituted analog, **N**.

| NBO | **N (L=N)** | | | NBO | **1 (L=P)** | | |
|---|---|---|---|---|---|---|---|
| | Population | % Th | % L | | Population | % Th | % L |
| Th-Cl | 1.9917 | 9.65 | 90.35 | Th-Cl | 1.9906 | 9.74 | 90.26 |
| Th-L | 1.9263 | 6.89 | 93.11 | Th-L | 1.9541 | 12.64 | 87.36 |
| Th-L* | 0.0701 | 93.11 | 6.89 | Th-L | 1.8548 | 12.73 | 87.27 |
| | | | | Th-L* | 0.0710 | 87.36 | 12.64 |
| | | | | Th-L* | 0.0638 | 87.27 | 12.73 |

Initial spectral simulation using the PBE functional was found to be inadequate and can be seen in Figure A-12. Therefore, absorption spectra were simulated with a range-separated hybrid exchange functional due to the significant charge transfer character of the transitions of interest.

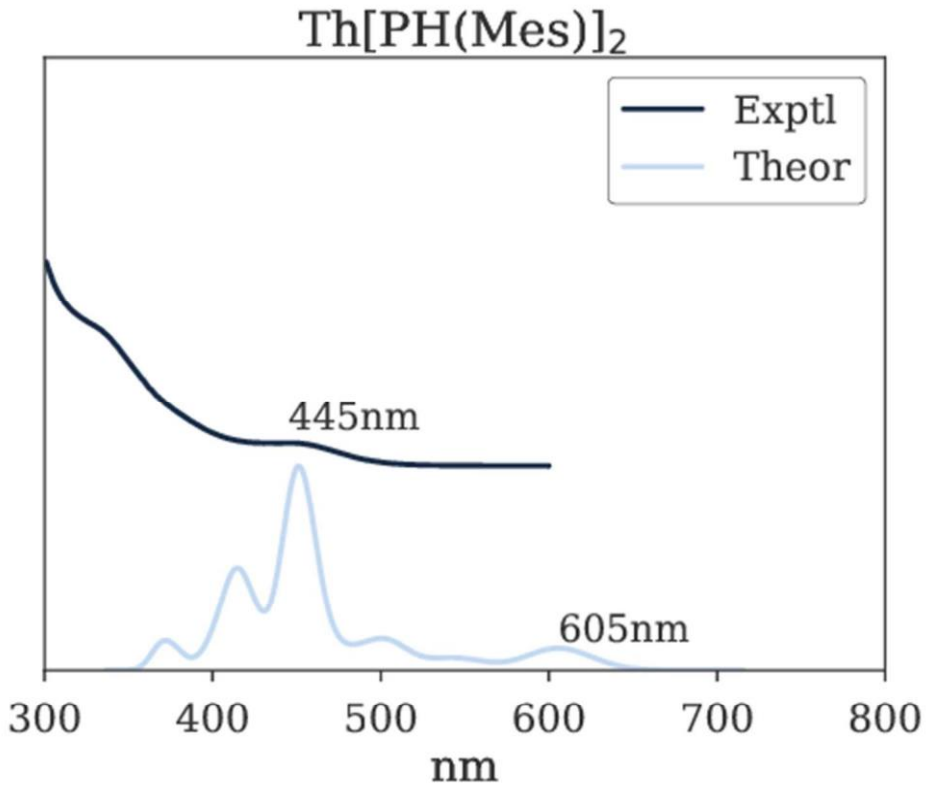


**Figure A-11.** Comparison between experimental and theoretical spectra when using a GGA functional.

Theoretical spectra were generated by Gaussian broadening (full width at half-maximum of 0.06 eV) of excitation energies weighted by their corresponding oscillator strengths. A comparison of experimental and theoretical absorption spectra of $(C_5Me_5)_2Th[PH(Mes)]_2$ and **6** can be seen in Figure A-12. The overall agreement of energies and peak intensities between the experimental and theoretical spectra is good. To inspect further the nature of the features seen in the experimental spectra, natural transition orbitals (NTOs) were computed and analyzed for all complexes. Given the similarity of the complexes, it is not surprising to see the same theme across the series. The shapes of all occupied NTOs correspond to phosphorus 3p orbitals. The virtual NTOs of the lowest energy excitations

are identifiable as 6d in nature. For the higher energy excitations, there is subtle competition between 6d and 5f character, making a clear identification in some cases difficult. The picture that emerges is that the absorbance spectra of these Th complexes are largely dominated by LMCT excitations from P to Th.

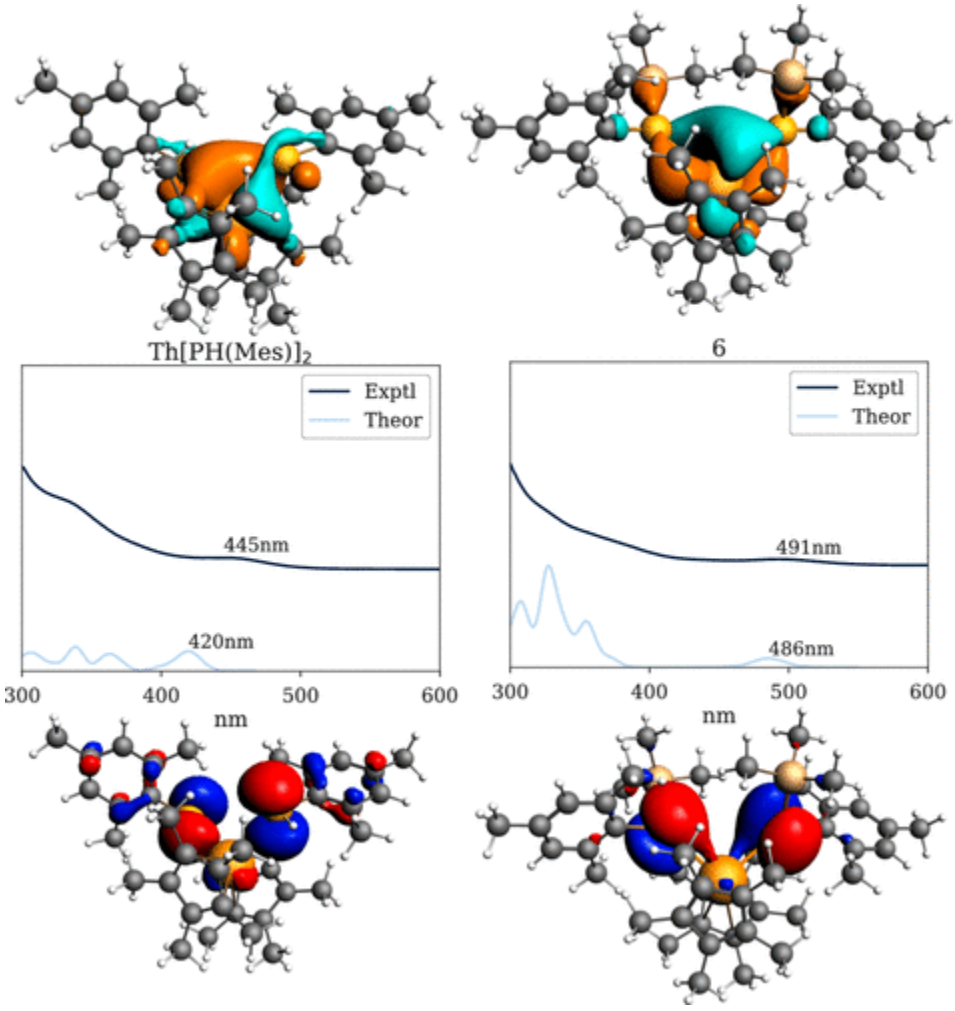


**Figure A-12.** Comparison of experimental and theoretical absorption spectra for $(C_5Me_5)_2Th[PH(Mes)]_2$ (left) and $(C_5Me_5)_2Th[P(Mes)(SiMe_3)]_2$ (**6**) (right). Theoretical spectra were generated by Gaussian broadening of 0.06 eV fwhm. The peak onset is well reproduced for most complexes. The lowest energy excitation contributing to the onset

features is depicted using isosurfaces (±0.03) of natural transition orbitals (NTOs) with the occupied orbital below the plot and the virtual orbital above the plot.

While a trend exists that the more donating the substituent on phosphorus, the lighter the color observed for the resulting thorium complex, the rationale is not so simple for correlating the UV–vis spectra to the donating strength as in $^{31}$P NMR spectroscopy. As the donation to phosphorus increases from mesityl to silyl to hydrogen, this should destabilize the phosphorus 3p orbitals more and lower the energy difference for the LMCT transitions. Therefore, the group with more electron donation should have a lower energy difference between the 3p and 5f/6d manifold. However, the UV–vis data indicate that the groups with more electron donation absorb at lower wavelength (400–500 nm range) in comparison to aryl substituents (>500 nm). For example, $(C_5Me_5)_2Th[PH(Mes)]_2$ has an absorbance maximum at 445 nm, while $(C_5Me_5)_2Th[P(CH_3)(Mes)]_2$ (**2**) has a maximum at 533 nm. The reason for this is not entirely understood. However, given the significantly different extents to which the occupied NTOs in Figure A-12 exhibit ligand to metal donation bonding, and the fact that this orbital shows π conjugation of the P lone pairs with the mesityl group for PH(Mes) but not for P(Mes)($SiMe_3$), it is clear that a simple argument based only on the energy of the phosphorus 3p lone pair orbital to explain the absorption energy trend should not be made.

**Conclusion**

The synthesis of the new thorium phosphido complexes $(C_5Me_5)_2ThX[P(Mes)R]$ has been conducted to understand the electronic structures that produce varying spectroscopic

features when the other substituents on phosphorus, R = H, Me, Mes, and $SiMe_3$, are varied. When X is another phosphide ligand, chloride, or methyl, the electronic structure does not change significantly, and the phosphido ligand seems to control that aspect of the molecule. A ligand-to-metal charge transfer (LMCT) from the 3p orbital of phosphorus to the thorium orbital, either 5f or 6d or a hybrid, is responsible for the different hues on the basis of the time-dependent density functional theory calculations. Due to the similar energetics of the 5f and 6d orbitals, the exact orbital cannot be definitively determined. The differences in structure and bonding are supported by $^{31}P$ NMR spectroscopy, which indicates the trend of increasing donating strength Mes < Me < $SiMe_3$ < H, and leads to decreasing frequency in the NMR spectra. We have further correlated our data with other phosphido complexes, showing that the trend exists beyond metallocene compounds. However, a similar rationale for the donating strength of the phosphido substituents and LMCT cannot be made; therefore, further investigations are needed. This highlights the complex nature of actinide−ligand bonding. Overall, we have shown that thorium phosphido complexes can have unique electronic structures on the basis of changes in energies of the states due to changing the substituents coordinated to phosphorus, which differ in comparison to group IV−phosphorus and thorium−nitrogen bonds.

## Appendix B: Coordination Chemistry and QTAIM Analysis of Homoleptic Dithiocarbamate Complexes, $M(S_2CN^iPr_2)_4$, M = Ti, Zr, Hf, Th, U, Np †

† This chapter is based on a manuscript that was submitted to and accepted by Inorganic Chemistry and can be cited as: Behrle, A. C.; **Myers, A. J.**; Rungthanaphatsophon, P.; Kerridge, A.; Walensky, J. R. Coordination Chemistry and QTAIM Analysis of Homoleptic Dithiocarbamate Complexes, $M(S_2CN^iPr_2)_4$, M = Ti, Zr, Hf, Th, U, Np, *Inorg. Chem.* **2018**, *57*, 10518.

Note: My contribution to this project was the synthesis and characterization of complex **7**.

### Introduction

The covalent character of actinide−ligand bonding is at the forefront of research in f-element chemistry[211,212] because the 4f orbitals have been presumed to be buried within the core orbitals and lack the radial extension to overlap with ligand-based orbitals. However, recent studies have indicated that this notion could be in error because orbital interactions have been observed in lanthanide complexes.[213,214] In contrast, transition metals have a high degree of covalent bonding due to strong nd and np orbital interactions. Interestingly, density functional theory (DFT) calculations in concert with X-ray absorption near-edge spectroscopy measurements have produced a vastly different picture of bonding in the f-block elements, which vary with the energetics of the metal-(5f) and ligand-based (np) orbitals.[167,215,216] According to first-order perturbation theory (Figure B-1), the mixing between the actinide and ligand in a molecular orbital is directly proportional to the overlap between the metal and ligand orbitals, β, with an inverse relationship between the energies of the orbitals, ε.[166,176] Therefore, an actinide−ligand

bond could appear more covalent than a transition-metal bond due to Figure B-1, because the difference in energy between the 5f and np orbitals will decrease upon going down a group, thus making the denominator small, and an increase in the covalent character is typically observed. However, the increased covalency could also be accompanied by a weaker metal−ligand bond.[217,218] For the lanthanides, the β term is virtually zero, but the energy difference between 4f and np is what could be the origin of covalent bonding. To continue to examine this phenomenon, our objective was to design a series of complexes with the same coordination sphere and oxidation state, hence creating a situation where the only differences are in the valence orbitals, ionic radius, and energy differences between the metal- and ligand-based orbitals.

$$\Psi = \Phi_f + \left(\frac{\beta}{\varepsilon_f - \varepsilon_L}\right)\Phi_L$$

**Figure B-1.** First-order perturbation theory equation.

Dithiocarbamates are an important class of ligands in the coordination chemistry of metals and main-group elements. The actinides are no exception because homoleptic dithiocarbamate complexes of thorium(IV),[219,220] uranium(IV),[221,222] neptunium(III),[155] neptunium(IV),[221,223] and plutonium(IV)[213] have been reported. Dithiocarbamate complexes bearing isopropyl groups have been examined but not structurally characterized, and we saw the opportunity to create a series of tetravalent complexes of group IV (titanium,[224,225] zirconium,[226,227] and hafnium[228]), thorium, uranium, and neptunium to investigate their molecular and electronic structures. This represents a rare study comparing transition-metal and actinide elements with identical oxidation states

and coordination environments, despite differences in their ionic radii.[167,216] Surprisingly, calculations indicate that similar covalent character is observed in the metal−sulfur bonds in transition metal and actinide complexes.

**General Considerations.**

The syntheses and manipulations described below were conducted using standard Schlenk and glovebox techniques. All reactions were conducted in a Vacuum Atmospheres inert-atmosphere ($N_2$) glovebox. $TiBr_4$, $ZrCl_4$, $HfCl_4$, and $^n$BuLi (Aldrich) were used as received. [$ThCl_4(DME)_2$],[229] [$UCl_4$],[31] and [$NpCl_4(DME)_2$][17] were synthesized as previously described. Toluene-$d_8$ (Cambridge Isotope Laboratories), $CS_2$, and $HN^iPr_2$ (Aldrich) were dried over molecular sieves and degassed with three freeze–evacuate–thaw cycles. All $^1$H and $^{13}$C NMR data were obtained on a 300 MHz DRX Bruker spectrometer. $^1$H NMR shifts given were referenced internally to the residual solvent peak at 2.08 ppm ($C_7D_7H$). For paramagnetic compounds, the $^1$H NMR resonances included the peak width at half-height given in Hertz. $^{13}$C NMR shifts were referenced internally to the residual peak at 20.42 ppm ($C_7D_8$). IR spectra were recorded as KBr pellets on a PerkinElmer Spectrum One FT-IR spectrometer. Elemental analyses were performed by Atlantic Microlab, Inc. (Norcross, GA), or Microanalytical Facility, University of California, Berkeley, using a PerkinElmer Series II 2400 CHNS analyzer. Single-crystal X-ray structure determinations were performed at the University of Missouri—Columbia.

**General Considerations for $^{237}$Np.**

**Caution!** $^{237}$Np is an α-emitting radionuclide (4.958 MeV, $t_{1/2} = 2.14 \times 10^6$ years, and a = 0.7 mCi g$^{-1}$). This research was conducted in a radiological laboratory with appropriate

counting equipment and analysis of hazards for the safe handling and manipulation of radioactive materials. Reactions were performed in a Vacuum Atmospheres inert-atmosphere (Ar) glovebox operated at negative pressure relative to the laboratory atmosphere. $^{1}$H NMR spectra were recorded on a 300 MHz DRX Bruker spectrometer. Neptunium samples were contained by placing a 4 mm polytetrafluoroethylene NMR tube liner inside a 5 mm glass NMR tube. Electronic absorption measurements were recorded on a sealed 1 cm quartz cuvette with a Varian Cary 5000 UV/vis/near-IR (NIR) spectrophotometer.

**Li($S_2CN^iPr_2$), 1**. An oven-dried Schlenk flask was charged with $HN^iPr_2$ (1.93 g, 19.10 mmol), followed by 10 mL of tetrahydrofuran (THF). The reaction flask was cooled to 0 °C, and $^n$BuLi (1.60 M in hexanes, 13.13 mL, 21.01 mmol) was added via syringe. The reaction was stirred for 1 h and cooled to −78 °C. $CS_2$ (1.45 g, 21.01 mmol) was added to the reaction via syringe, and the reaction was allowed to stir for 0.5 h at −78 °C. The reaction was stirred for an additional 12 h at room temperature to yield a clean bright-orange solution. The solvent was removed in vacuo to yield a tacky orange/red solid (3.45 g, 99%). $^{1}$H NMR ($C_7D_8$, −40 °C): δ 6.60 (sept, 1H, $^{3}J_{H–H}$ = 6.6 Hz, C*H*$(CH_3)_2$), 3.76–3.72 (m, 8H, THF), 3.53 (sept, 1H, $^{3}J_{H–H}$ = 6.6 Hz, C*H*$(CH_3)_2$), 1.90 (d, 6H, $^{3}J_{H–H}$ = 6.6 Hz, CH(C*H*$_3)_2$), 1.40–1.34 (m, 8H, THF), 1.02 (d, 6H, $^{3}J_{H–H}$ = 6.6 Hz, CH(C*H*$_3)_2$. $^{13}$C{$^{1}$H} NMR ($C_7D_8$, 25 °C): δ 211.06, 68.58 (THF), 55.43, 50.24, 25.10 (THF), 21.09, 19.57. IR (cm$^{-1}$): 2980 (s), 2922 (m), 2851 (m), 2459 (m), 1480 (s), 1420 (s), 1387 (s), 1329 (s), 1155 (s), 1146 (s), 1055 (s), 832 (m), 800 (m), 583 (m), 472 (m).

**Ti($S_2CN^iPr_2)_4$, 1**. An oven-dried 20 mL scintillation vial was charged with **1** (300 mg, 1.64 mmol) and dissolved in toluene. The reaction mixture was cooled to −20 °C, and

$TiBr_4$ (147 mg, 0.399 mmol) was added to the stirring solution. An immediate color change to dark red was observed, and the reaction was allowed to stir at room temperature for 12 h. The reaction mixture was centrifuged and filtered over a bed of Celite. The reaction mixture was concentrated and layered with hexanes to yield a red microcrystalline powder (230 mg, 77%). X-ray-quality crystals were grown from a THF/hexanes mixture at room temperature. $^1$H NMR ($C_7D_8$, −40 °C): δ 5.27 (s, br, 4H, C*H*($CH_3$)), 3.27 (s, br, 4H, C*H*($CH_3$)), 1.51 (s, br, 24H, CH(C*H*$_3$)), 0.66 (s, br, 24H, CH(C*H*$_3$)). $^{13}$C{$^1$H} NMR ($C_7D_8$, −40 °C): δ 207.39, 51.08, 49.64, 20.58, 18.70. IR ($cm^{-1}$): 2970 (s), 2930 (m), 2872 (m), 2419 (m), 1480 (s), 1446 (s), 1384 (s), 1322 (s), 1198 (s), 1148 (s), 1043 (s), 836 (m), 800 (m), 587 (m), 477 (m). Anal. Calcd for $C_{28}H_{56}N_4S_8Ti$: C, 44.65; H, 7.49; N, 7.44. Found: C, 44.71; H, 7.56; N, 7.39.

**Zr($S_2CN^iPr_2$)$_4$, 3**. An oven-dried 20 mL scintillation vial was charged with **1** (300 mg, 1.64 mmol) and dissolved in THF. The reaction mixture was cooled to −20 °C, and $ZrCl_4$ (93 mg, 0.399 mmol) was added to the stirring solution. An immediate color change to orange/red was observed, and the reaction was allowed to stir at room temperature for 12 h. The reaction mixture was centrifuged and filtered over a bed of Celite. The solvent was removed, and the yellow solid was extracted twice with toluene, filtered over a bed of Celite, and concentrated to yield a yellow microcrystalline powder (210 mg, 66%). The solvent was reduced to one-third of its original level and layered with hexanes. X-ray-quality crystals were grown from a THF/hexanes mixture at room temperature. $^1$H NMR ($C_7D_8$, −40 °C): δ 5.44 (s, br, 4H, C*H*($CH_3$)), 3.20 (s, br, 4H, C*H*($CH_3$)), 1.51 (s, br, 24H, CH(C*H*$_3$)), 0.61 (s, br, 24H, CH(C*H*$_3$)). $^{13}$C{$^1$H} NMR ($C_7D_8$, −40 °C): δ 206.31, 51.67, 49.99, 20.23, 18.60. IR ($cm^{-1}$): 2971 (s), 2929 (s), 2872 (s), 1480 (vs), 1463 (s), 1444 (s),

1370 (s), 1324 (vs), 1198 (s), 1149 (s), 1120 (w), 1041 (s), 948 (w), 908 (s), 898 (w), 849 (w), 586 (m). Anal. Calcd for $C_{28}H_{56}N_4S_8Zr$: C, 42.22; H, 7.09; N, 7.03. Found: C, 42.45; H, 7.16; N, 6.86.

**$Hf(S_2CN^iPr_2)_4$, 4**. Following the procedure for **3**, **1** (300 mg, 1.64 mmol) and $HfCl_4$ (128 mg, 0.399 mmol) yielded an orange microcrystalline precipitate (116 mg, 33%). X-ray-quality crystals were grown from a THF/hexanes mixture at room temperature. $^1$H NMR ($C_7D_8$, −40 °C): δ 5.38 (s, br, 4H, C*H*($CH_3$)), 3.18 (s, br, 4H, C*H*($CH_3$)), 1.54 (s, br, 24H, CH(C*H*$_3$)), 0.64 (s, br, 24H, CH(C*H*$_3$)). $^{13}$C{$^1$H} NMR ($C_7D_8$, −40 °C): δ 206.25, 52.06, 49.86, 20.12, 18.31. IR ($cm^{-1}$): 2969 (s), 2928 (s), 2873 (s), 1476 (s), 1447 (s), 1373 (s), 1323 (s), 1197 (s), 1146 (s), 1042 (s), 957 (w), 856 (w), 797 (w), 582 (m), 532 (w). Anal. Calcd for $C_{28}H_{56}N_4S_8Hf$: C, 38.05; H, 6.39; N, 6.34. Found: C, 37.49; H, 6.15; N, 6.26.

**$Th(S_2CN^iPr_2)_4$, 5**. An oven-dried 20 mL scintillation vial was charged with **1** (334 mg, 1.82 mmol) and dissolved in THF. $ThCl_4(DME)_2$ (246 mg, 0.444 mmol) was added to the solution at room temperature, resulting in an orange/red solution, and stirred for 12 h. The solvent was removed in vacuo, extracted twice with toluene, filtered over a bed of Celite, and concentrated to yield a colorless precipitate (233 mg, 56%). X-ray-quality crystals were grown from a concentrated THF/hexanes mixture at room temperature. $^1$H NMR ($C_7D_8$, −40 °C): δ 5.64 (s, br, 4H, C*H*($CH_3$)$_2$), 3.26 (s, br, 4H, C*H*($CH_3$)$_2$), 1.51 (s, br, 24H, CH(C*H*$_3$)$_2$), 0.68 (s, br, 24H, CH(C*H*$_3$)$_2$). $^{13}$C{$^1$H} NMR ($C_7D_8$, −40 °C): δ 204.16, 52.81, 50.47, 20.06, 18.36. IR ($cm^{-1}$): 3003 (m), 2972 (s), 2930 (s), 2876 (m), 2414 (m), 1479 (s), 1444 (s), 1383 (s), 1319 (s), 1194 (s), 1144 (s), 1118 (m), 1039 (s), 943 (m), 835 (m), 790 (m), 584 (m), 475 (m). Anal. Calcd for $C_{28}H_{56}N_4S_8Th$: C, 35.88; H, 6.02; N, 5.98. Found: C, 36.11; H, 5.84; N, 6.16.

**$U(S_2CN^iPr_2)_4$, 6**. An oven-dried 20 mL scintillation vial was charged with **1** (349 mg, 1.90 mmol) and dissolved in THF. The reaction mixture was cooled to −20 °C, and $UCl_4$ (176 mg, 0.465 mmol) was added, resulting in a brown/yellow color change. The mixture was stirred for 12 h at room temperature. The solvent was removed in vacuo, and the solid was extracted twice with toluene, filtered over a bed of Celite, and concentrated to yield a dark-brown precipitate (206 mg, 47%). X-ray-quality crystals were grown from a concentrated THF/hexanes mixture at room temperature. $^1$H NMR ($C_7D_8$, −40 °C): δ 8.27 (s, br, 4H, C*H*$(CH_3)_2$, $\nu_{1/2}$ = 49 Hz), 3.76 (s, br, 4H, C*H*$(CH_3)_2$, $\nu_{1/2}$ = 49 Hz), 3.14 (s, br, 24H, CH(C*H*$_3)_2$, $\nu_{1/2}$ = 24 Hz), 1.84 (s, br, 24H, CH(C*H*$_3)_2$, $\nu_{1/2}$ = 26 Hz). IR ($cm^{-1}$): 2970 (s), 2928 (s), 2877 (m), 1474 (s), 1446 (s), 1373 (s), 1320 (s), 1192 (s), 1145 (s), 1036 (s), 933 (m), 913 (m), 849 (w), 792 (w), 584 (m), 525 (w), 473 (w). Anal. Calcd for $C_{28}H_{56}N_4S_8U$: C, 35.64; H, 5.98; N, 5.94. Found: C, 35.77; H, 5.78; N, 5.76.

**$Np(S_2CN^iPr_2)_4$, 7**. An oven-dried 20 mL scintillation vial was charged with $NpCl_4(DME)_2$ (17.5 mg, 0.032 mmol) and dissolved in 1.5 mL of THF. After cooling to −35 °C, the solution was added to solid $Li(S_2CN^iPr_2)$ (23.5 mg, 0.13 mmol), resulting in a red/orange color change. The mixture was stirred for 18 h at room temperature and the solvent removed *in vacuo*. The solid was extracted twice with toluene and filtered over a bed of Celite, and the solvent removed in vacuo to yield a red/orange solid (20.7 mg, 70%). X-ray-quality crystals were grown from a concentrated THF/hexanes mixture at room temperature. $^1$H NMR ($C_7D_8$, −40 °C): δ 6.91 (s, br, 4H, C*H*$(CH_3)_2$, $\nu_{1/2}$ = 29 Hz), 2.70 (s, br, 24H, CH(C*H*$_3)_2$, $\nu_{1/2}$ = 16 Hz), 1.50 (s, br, 4H, C*H*$(CH_3)_2$, $\nu_{1/2}$ = 24 Hz), 0.41 (s, br, 24H, CH(C*H*$_3)_2$, $\nu_{1/2}$ = 13 Hz). Vis/NIR [THF, 2.0 mM, 25 °C; λ, nm (ε, L $mol^{-1}$

$cm^{-1}$)]: 684 (59), 746 (112), 773 (133), 789 (141), 885 (57), 891 (178), 966 (142), 952 (160), 1037 (75), 1578 (39), 1867 (30).

**Crystallographic Data Collection and Structure Determination**

Selected single crystals for the non-neptunium complexes were mounted on nylon cryoloops using viscous hydrocarbon oil. A selected single neptunium crystal was coated with viscous hydrocarbon oil inside the glovebox before being mounted on a nylon cryoloop using Devcon 2 Ton epoxy. X-ray data collection was performed at 173(2) or 100(2) K. The X-ray data were collected on a Bruker CCD diffractometer with monochromated Mo Kα radiation (λ = 0.71073 Å). The data collection and processing utilized the Bruker *Apex2* suite of programs.[32] The structures were solved using direct methods and refined by full-matrix least-squares methods on $F^2$ using the Bruker *SHELX-2014/7* program.[33] All non-H atoms were refined with anisotropic displacement parameters. All H atoms were placed at calculated positions and included in the refinement using a riding model. Thermal ellipsoid plots were prepared by using *Olex2*[34] with 50% of probability displacements for the non-H atoms. Crystal data and details for data collection for complexes **2**–**7** are also provided in Table B-1.

**Table B-1.** X-ray crystallographic data shown for complex **2-7**.

| | **2** | **3** | **4** |
|---|---|---|---|
| CCDC deposit number | 1411381 | 1411382 | 1411383 |
| Empirical formula | $C_{28}H_{56}N_4S_8Ti$ | $C_{28}H_{56}N_4S_8Zr$ | $C_{28}H_{56}N_4S_8Hf$ |
| Formula weight (g/mol) | 753.14 | 796.46 | 883.73 |
| Crystal habit, color | Prism, red | Prism, yellow | Prism, yellow |
| Temperature (K) | 173(2) | 100(2) | 100(2) |
| Space group | $P2_12_12_1$ | $P2_12_12_1$ | $P2_12_12_1$ |
| Crystal system | Orthorhombic | Orthorhombic | Orthorhombic |
| Volume (Å$^3$) | 3937.8(3) | 4006.4(4) | 4003.2(4) |
| $a$ (Å) | 13.7423(6) | 13.8180(8) | 13.8045(8) |
| $b$ (Å) | 14.4550(6) | 14.5805(9) | 14.5839(8) |
| $c$ (Å) | 19.8231(9) | 19.8855(12) | 19.8845(11) |
| $\alpha$ (˚) | 90 | 90 | 90 |
| $\beta$ (˚) | 90 | 90 | 90 |
| $\gamma$ (˚) | 90 | 90 | 90 |
| $Z$ | 4 | 4 | 4 |
| Calculated density (Mg/m$^3$) | 1.27 | 1.32 | 1.466 |
| Absorption coefficient (mm$^{-1}$) | 0.665 | 0.715 | 3.047 |
| Final R indices [I > 2σ(I)] | R = 0.0215<br>$R_W$ = 0.0542 | R = 0.0190<br>$R_W$ = 0.0457 | R = 0.0121<br>$R_W$ = 0.0291 |

| | **5** | **6** | **7** |
|---|---|---|---|
| CCDC deposit number | 1411384 | 1411385 | 1583533 |
| Empirical formula | $C_{28}H_{56}N_4S_8Th$ | $C_{28}H_{56}N_4S_8U$ | $C_{28}H_{56}N_4S_8Np$ |
| Formula weight (g/mol) | 937.28 | 943.27 | 942.24 |
| Crystal habit, color | Prism, yellow | Prism, brown | Prism, red |
| Temperature (K) | 100(2) | 100(2) | 100(2) |
| Space group | $P2_1/c$ | $P2_1$ | $P2_1$ |
| Crystal system | Monoclinic | Monoclinic | Monoclinic |
| Volume (Å$^3$) | 3996.1(6) | 2018.0(2) | 2007.8(3) |
| *a* (Å) | 17.5846(15) | 10.2466(7) | 10.2184(9) |
| *b* (Å) | 10.5094(9) | 14.0423(10) | 14.0444(12) |
| *c* (Å) | 21.9226(19) | 14.7375(10) | 14.6986(13) |
| $\alpha$ (˚) | 90 | 90 | 90 |
| $\beta$ (˚) | 99.477(1) | 107.8860(10) | 107.8560(10) |
| $\gamma$ (˚) | 90 | 90 | 90 |
| *Z* | 4 | 2 | 2 |
| Calculated density (Mg/m$^3$) | 1.558 | 1.552 | 1.559 |
| Absorption coefficient (mm$^{-1}$) | 4.173 | 4.459 | 3.027 |
| Final R indices [I > 2σ(I)] | R = 0.0218 $R_W$ = 0.0427 | R = 0.0298 $R_W$ = 0.0696 | R = 0.0199 $R_W$ = 0.0413 |

**Computational Details**

All calculations were performed at the DFT level using version 6.6 of the *TURBOMOLE* quantum chemistry software package.[230] XRD-derived structural parameters were used as the basis for geometry optimizations. The hybrid generalized gradient approximation

(GGA) Perdew–Burke–Ernzerhof (PBE0)[231] exchange-correlation functional, which incorporates a perturbatively derived 25% contribution of exact exchange, was used throughout. In all calculations, basis sets of polarized triple-ζ quality were used. For geometry optimizations, Ahlrichs-style basis sets[232,233] were employed, incorporating effective core potentials replacing 28 core electrons of Zr and 60 core electrons of Hf, Th, U, and Np.[234,235] We have successfully applied this model chemistry in previous studies of f-element complexes.[236,237] All complexes considered in this study were identified as energetic minima through vibrational frequency analysis.

The topological properties of the resulting electron densities were obtained via application of the Quantum Theory of Atoms in Molecules (QTAIM),[238] as implemented in version 14.11.23 of the *AIMAll* code.[239] In order to perform analysis of the integrated properties of the density via QTAIM, all-electron single-point-energy calculations were performed at the optimized geometries. These calculations employed the Zr TZVPalls2 basis set of Ahlrichs and May[240] and the Hf, Th, U, and Np SARC basis sets of Pantazis et al.[241,242] and incorporated scalar relativistic effects via the second-order Douglas–Kroll–Hess Hamiltonian.

**Results**

The isopropyl derivative was targeted for its solubility properties in arene solvents, which made for facile isolation. Deprotonation of $HN^iPr_2$ with $^nBuLi$, followed by the addition of $CS_2$, affords $LiS_2CN^iPr_2$, **1**. The reaction of 4 equiv of **1** with $MCl_4$ yields the corresponding homoleptic metal dithiocarbamate complexes $M(S_2CN^iPr_2)_4$ (M = Ti, **2**; Zr, **3**; Hf, **4**; Th, **5**; U, **6**, Np, **7**; Figure B-2) in moderate-to-good crystalline yields.

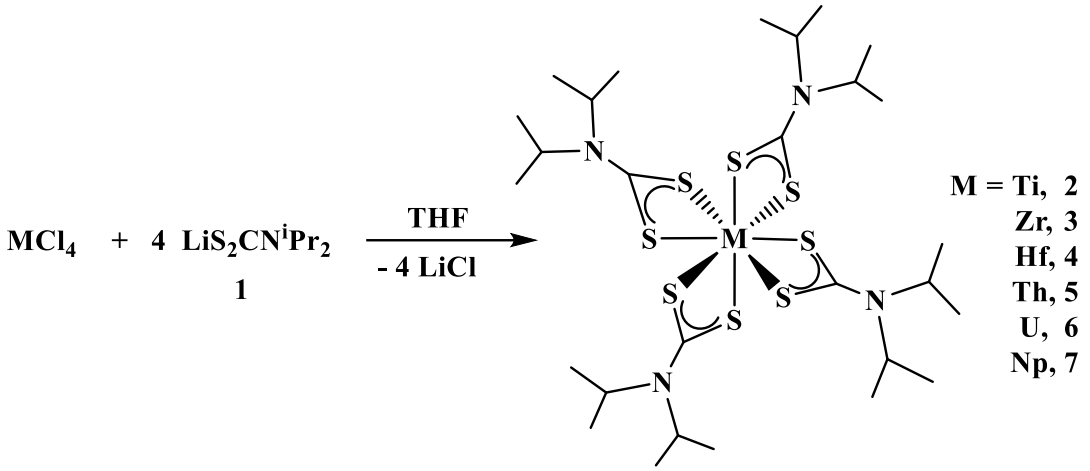


**Figure B-2.** Reaction scheme of $MCl_4$ with four equivalents of **1.**

All complexes displayed fluxional behavior in solution, as observed using $^1$H NMR spectroscopy at room temperature. This has been seen previously[243] with this ligand set; hence, $^1$H NMR spectra were taken at −40 °C. Resonances for the isopropyl methyl and methine protons are summarized in Table B-2. The resonances do not show any particular pattern for the diamagnetic species but are paramagnetically shifted for the uranium(IV) and neptunium(IV) complexes. The visible and NIR spectra (Figure B-3) of **7** showed features similar to those observed in $Np[S_2P(C_6H_5)_2]_4$.[243]

**Table B-2.** $^1$H NMR Resonances for the Isopropyl Methyl and Methine Protons for Complexes **1**–**7**.

| **Complex, M** | **CH(C*H*$_3$)$_2$ $^1$H NMR resonances (ppm)** | **C*H*(CH$_3$)$_2$ $^1$H NMR resonances (ppm)** |
|---|---|---|
| **1**, Li | 1.90, 1.02 | 6.60, 3.53 |
| **2**, Ti | 1.51, 0.66 | 5.27, 3.27 |
| **3**, Zr | 1.51, 0.61 | 5.44, 3.20 |

| | | |
|---|---|---|
| **4**, Hf | 1.54, 0.64 | 5.38, 3.18 |
| **5**, Th | 1.51, 0.68 | 5.64, 3.26 |
| **6**, U | 3.14, 1.84 | 8.27, 3.76 |
| **7**, Np | 2.70, 0.41 | 6.91, 1.50 |

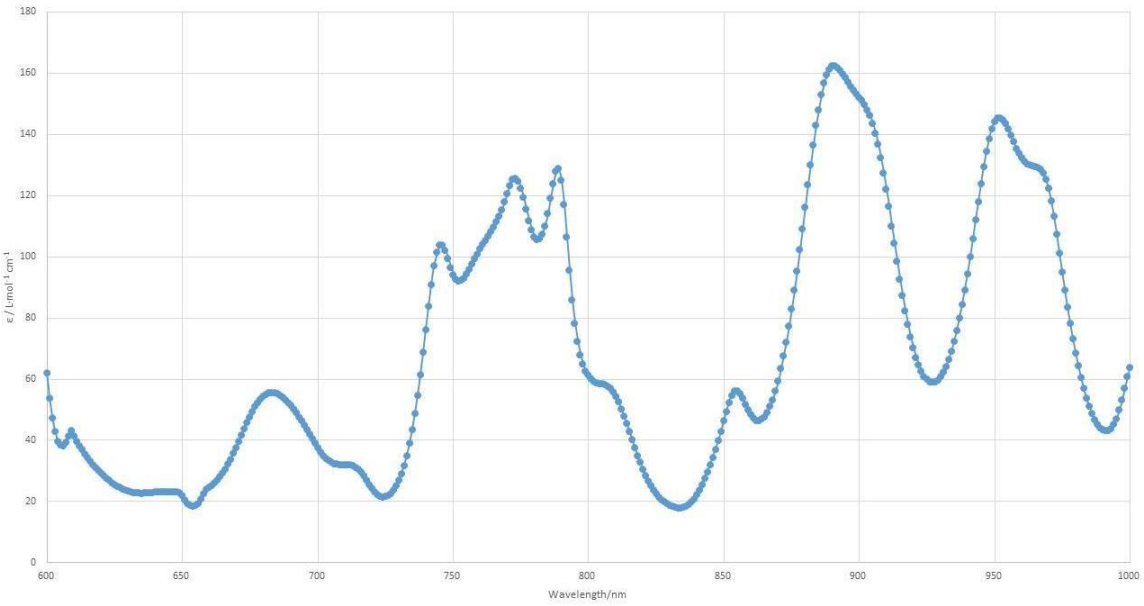


**Figure B-3.** Electronic absorption spectrum of **7** from 600-1000 nm.

The solid-state structures of complexes **2**–**7** were determined using X-ray crystallography analysis, with selected bond distances shown in Table B-3. Representative examples, complexes **4** and **7**, are shown in Figure B-4. Each complex is eight-coordinate in a trigonal-dodecahedral arrangement about the metal center. The M–S bond distances mimic the ionic radii of these complexes with the shortest M–S distances found with Ti ($r$ = 0.74 Å) and the longest with Th ($r$ = 1.05 Å).[100] The M–S bond lengths are similar to others reported. For example, the average Ti–S bond distance of 2.552 Å in **1** is similar to the range of bond lengths of 2.522(8)–2.606(8) Å in $Ti(S_2CNEt_2)_4$.[224] In **2**, an average Zr–S bond distance of 2.655 Å was observed, which is similar to 2.69 Å in

$(C_5H_5)Zr(S_2CNMe_2)_3$.[244] While no dithiocarbamate ligated complexes of Hf could be found, the average Hf–S bond distance of 2.640 Å in **4** is reasonable given that $Hf^{4+}$ ($r$ = 0.97 Å) is slightly smaller than $Zr^{4+}$ ($r$ = 0.98 Å),[100] thus having a slightly shorter bond distance. The homoleptic complexes $An(S_2CNEt_2)_4$ (An = Th,[212] Np[216]) compare well with the average Th–S and Np–S distances of 2.87 Å (2.870 Å in **5**) and 2.795 Å (2.787 Å in **7**), respectively. The average U–S bond length of 2.803 Å in **6** is similar to the U–S distances of 2.801(7) and 2.810(7) Å in $[(C_8H_8)U(S_2CNEt_2)(THF)_2][BPh_4]$.[222] The decrease in the M–S bond distances from Th to U to Np is consistent with the actinide contraction. We note that the coordination chemistry of Np, especially non-neptunyl species, is rare compared to that of Th and U.[110,139]

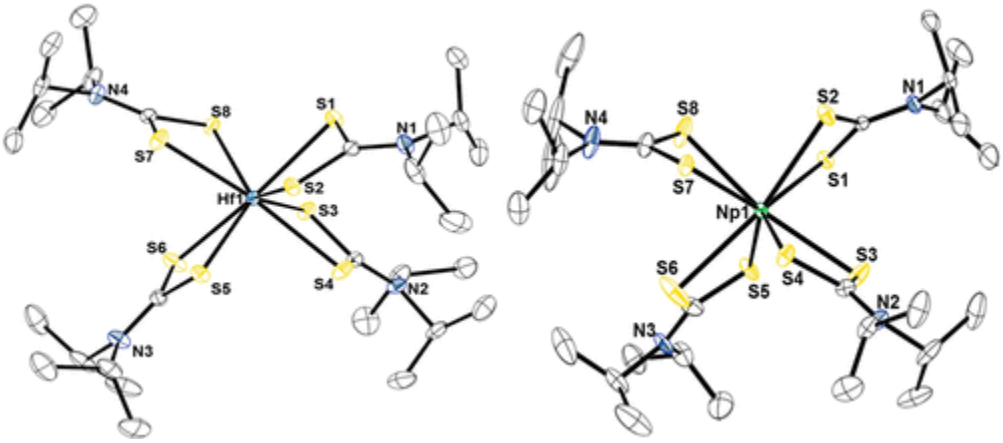


**Figure B-4.** Thermal ellipsoid plots of **4** (left) and **7** (right) shown at the 50% probability level. The hydrogen atoms have been omitted for clarity.

**Structural Parameters**

The M–S bond lengths, averaged over the eight bonds in each complex, are compared in Table B-4. Theoretical values are in very good agreement with the experiment, typically accurate to within 0.01 Å.

**Table B-3.** Selected bond distances (Å) and angles (deg) for complexes **2**–**7**.

| | **2, Ti** | **3, Zr** | **4, Hf** | **5, Th** | **6, U** | **7, Np** |
|---|---|---|---|---|---|---|
| M1-S1 | 2.5154(4) | 2.6471(6) | 2.6185(6) | 2.8824(8) | 2.818(3) | 2.7640(8) |
| M1-S2 | 2.6086(4) | 2.6509(6) | 2.6728(6) | 2.8445(7) | 2.791(3) | 2.7791(11) |
| M1-S3 | 2.5873(4) | 2.6635(6) | 2.6500(6) | 2.9016(7) | 2.835(2) | 2.7878(11) |
| M1-S4 | 2.5200(4) | 2.6488(6) | 2.6279(6) | 2.8557(8) | 2.788(3) | 2.7928(7) |
| M1-S5 | 2.5727(4) | 2.6614(6) | 2.6528(6) | 2.8731(7) | 2.800(3) | 2.8079(9) |
| M1-S6 | 2.5288(5) | 2.6487(6) | 2.6299(6) | 2.8811(8) | 2.8078(19) | 2.7786(9) |
| M1-S7 | 2.5598(4) | 2.6827(6) | 2.6382(6) | 2.8530(7) | 2.806(3) | 2.7762(9) |
| M1-S8 | 2.5253(4) | 2.6371(6) | 2.6303(6) | 2.8725(8) | 2.781(2) | 2.7992(10) |
| S1-M1-S2 | 66.872(14) | 65.581(18) | 65.635(19) | 61.68(2) | 62.74(6) | 63.31(3) |
| S1-M1-S6 | 156.435(16) | 160.746(19) | 158.45(2) | 167.57(2) | 162.92(8) | 161.31(3) |

**Table B-4.** Comparison of the Experimental and Theoretical M–S Bond Lengths in $M(S_2CN^iPr_2)_4$ (M = Ti, Zr, Hf, Th, U, Np). Mean average deviations are given in parentheses. All values are in angstroms.

| **Complex** | **Exp** | **PBE0** |
|---|---|---|
| $Ti(S_2CN^iPr_2)_4$ | 2.552 (0.001) | 2.548 (0.048) |
| $Zr(S_2CN^iPr_2)_4$ | 2.655 (0.002) | 2.665 (0.019) |
| $Hf(S_2CN^iPr_2)_4$ | 2.640 (0.002) | 2.665 (0.022) |
| $Th(S_2CN^iPr_2)_4$ | 2.870 (0.002) | 2.879 (0.001) |
| $U(S_2CN^iPr_2)_4$ | 2.803 (0.008) | 2.809 (0.012) |

| | | |
|---|---|---|
| $Np(S_2CN^iPr_2)_4$ | 2.787 (0.003) | 2.799 (0.008) |

**Topological Properties of the Electron Density**

The properties of the electron density at QTAIM-derived M–S bond critical points (BCPs) are summarized in Table B-5. While these properties are indicative of predominantly ionic interactions, $\rho < 0.1$, the magnitude of the electron densities at the M–S BCP of the uranium and neptunium complexes are noticeably higher than that in the thorium analogue, implying greater covalency in the former two. This trend is mirrored by the BCP energy densities *H* and is as seen previously,[237,245] although the difference between the values obtained for uranium/neptunium and thorium complexes is less pronounced here. The Laplacian of the electron density, $\nabla^2\rho$, is positive, indicative of a predominantly ionic interaction, although, interestingly, it is larger in the neptunium and uranium complexes. We have previously shown that positive values of the Laplacian are found in uranium complexes even when the covalency is pronounced[246] and that decreasing covalency can be accompanied by an increasing Laplacian: in this context, the Laplacian data presented here are commensurate with other metrics.

Considering the transition-metal complexes, no periodic trend is found in ρ, although the electron density is very similar in all complexes and comparable to that found in the uranium/neptunium analogues. $\nabla^2\rho$ and *H* exhibit periodic and opposing trends, suggestive of a weakly increasing covalency but perhaps simply reflective of a softening of the ions.

**Table B-5.** Topological Properties at the M–S BCPs of the PBE0-Derived Electron Densities.[a]

| Complex | ρ | $\nabla^2\rho$ | *H* |
|---|---|---|---|
| $Ti(S_2CN^iPr_2)_4$ | 0.055 | 0.089 | –0.0113 |
| $Zr(S_2CN^iPr_2)_4$ | 0.055 | 0.082 | –0.0126 |
| $Hf(S_2CN^iPr_2)_4$ | 0.054 | 0.081 | –0.0134 |
| $Th(S_2CN^iPr_2)_4$ | 0.052 | 0.063 | –0.0117 |
| $U(S_2CN^iPr_2)_4$ | 0.056 | 0.078 | –0.0134 |
| $Np(S_2CN^iPr_2)_4$ | 0.056 | 0.078 | –0.0135 |

[a]ρ = electron density, $\nabla^2\rho$ = Laplacian of the density, and *H* = energy density. All values are in atomic units.

**Integrated Properties of the Electron Density**

The QTAIM definition of an atom allows for the evaluation of both one- and two-electron integrated properties. The atomic charge *q* (a one-electron property) and the localization and delocalization indices λ and δ (two-electron properties) are summarized for Ti, Zr, Hf, Th, U, Np, and S in Table B-6. Here, a periodic trend is found: the atomic charge, *q*(M), increases from Ti to Hf, while the sulfur charge, *q*(S), drops, suggesting increased ionic interaction. Consideration of the two-electron properties supports this assertion: the M–S delocalization indices (the number of electrons shared between the two atoms), which can be considered an alternative measure of the covalent character,[237,245–247] decrease from Ti to Hf (0.438 to 0.416 to 0.400), implying a reduction

in the covalent character. The one- and two-electron data combined therefore describe a weak transition in the nature of the M–S bond from Ti to Hf. The data support the characterization of uranium and neptunium, 0.481 and 0.482, respectively, as exhibiting greater covalent character than Th (0.421) and, in fact, imply that the U/Np–S (0.481 and 0.482, respectively) bond is the most covalent of any considered here. Previous work on actinide complexes[237,245,247] led us to conclude that delocalization indices provided a more robust description of the covalency than that provided by the topological properties of the electron density alone. In comparison, the delocalization indices for the thorium and uranium complexes are very similar to those observed in dithiophosphinate and dithiophosphonate complexes.[110,236]

**Table B-6.** Integrated QTAIM Properties of the PBE0-Derived Electron Densities.[a]

| Complex | $q$(M) | λ(M) | $q$(S) | δ(M, S) |
|---|---|---|---|---|
| $Ti(S_2CN^iPr_2)_4$ | +1.89 | 18.21 | –0.14 | 0.438 |
| $Zr(S_2CN^iPr_2)_4$ | +2.15 | 36.05 | –0.19 | 0.416 |
| $Hf(S_2CN^iPr_2)_4$ | +2.28 | 68.00 | –0.21 | 0.400 |
| $Th(S_2CN^iPr_2)_4$ | +2.43 | 85.74 | –0.25 | 0.421 |
| $U(S_2CN^iPr_2)_4$ | +2.23 | 87.67 | –0.22 | 0.481 |
| $Np(S_2CN^iPr_2)_4$ | +2.17 | 88.73 | –0.21 | 0.482 |

[a] $q$ = atomic charge, λ = localization index, and δ = delocalization index. All values are in atomic units.

We have previously noted that the difference between the atomic number $Z$ and the localization index λ correlates with the oxidation states in f-element complexes,[237,248,249]

and we also find this correlation here: $Z - \lambda$ values fall in the range 3.79–4.33, close to the formal 4+ oxidation state and with a trend toward larger values for heavier elements.

**Discussion**

A few studies have been conducted comparing the molecular and electronic structures of transition-metal and actinide complexes.[250] In one report, the bonds in $(C_5Me_5)_2MCl_2$ (M = Ti, Zr, Hf, Th, U) complexes were compared, and it was concluded that half the amount of covalent character was observed in the U–Cl bond versus the transition-metal analogues.[226] In that study, titanium had the greatest covalent character. Interestingly, when looking at $MCl_6^{2-}$ complexes, the same group concluded that $UCl_6^{2-}$ had a greater covalent character in the M–Cl bond than the transition-metal analogues.[166] In this study, we have examined homoleptic transition-metal and actinide complexes, and while admittedly based only on the delocalization indices from QTAIM calculations, an increase in covalent character between the actinide–sulfur bonds is observed in comparison to their transition-metal counterparts. The similarity between $MCl_6^{2-}$ and $M(S_2CN^iPr_2)_4$ is related to their homoleptic nature as well as the energy difference of the 3p versus 5f orbitals of the actinides. As we traverse the actinide series from Th to U to Np, the 5f orbitals will decrease in energy; hence, the energy difference between the 5f and 3p orbitals of S will decrease, thus leading to an increase in the delocalization indices in the actinide complexes and the indication of enhanced covalent character. This is not the case for the transition metals, and there is a decrease in the metal–ligand overlap between the 4d (Zr) and 5d (Hf) orbitals compared to the 3d (Ti) orbitals because the d orbitals become more diffuse down group IV.

## Conclusion

Elucidation of the role of the valence orbitals of the actinides remains a challenge. Here, we investigated the homoleptic dithiocarbamate complexes $M(S_2CN^iPr_2)_4$ (M = Ti, Zr, Hf, Th, U, Np) and have shown using DFT that these complexes show a higher degree of covalent bonding in the actinide (uranium and neptunium) complexes than the group IV analogues. Interestingly, this ordering does not match previous studies with $(C_5Me_5)_2MCl_2$ (M = Ti, Zr, Hf, Th, U); however, the homoleptic system $MCl_6^{2-}$ (M = Ti, Zr, Hf, U), has an ordering similar to the complexes reported here.

## References


1) U.S Energy Information Administration. Nuclear explained U.S. nuclear industry. ***2019.*** https://www.eia.gov/energyexplained/nuclear/us-nuclear-industry.php

2) GAO-17-340: Resuming Licensing of the Yucca Mountain Repository Would Require Rebuilding Capacity at DOE and NRC, Among Other Key Steps. Apr 26, **2017**.

3) Lab, K. A. P. Nuclides and Isotopes: Chart of the Nuclides 17th Edition. **2010**.

4) Zhao, P.; Tinnacher, R. M.; Zavarin, M.; Kersting, A. B. Analysis of trace neptunium in the vicinity of underground nuclear tests at the Nevada National Security Site. *J. Environ. Radioactiv.* **2014**, 137, 163-172.

5) Albright, D.; Kramer, K. Neptunium 237 and Americium: World Inventories and Proliferation Concerns. **2005**.

6) Witze, A. Nuclear power: Desperately seeking plutonium. *Nature* **2014**, 515484–486.

7) Zhang, H.; Kaur, M.; Qiang, Y. Magnetic nanosorbents for fast separation of radioactive waste. International Nuclear Fuel Cycle Conference, Salt Lake City, UT, United States, Sept. 29-Oct. 3, **2013**, 1, 564-569.

8) Niles, K. The Hanford cleanup: What's taking so long? Bulletin of the Atomic Scientists **2015**, 70, 37-48.

9) Energy Department (2013b) Hanford Site cleanup completion framework. January, **2013**.

10) Groom, C. R.; Bruno, I. J.; Lightfoot, M. P.; Ward, S. C. The Cambridge Structural Database. *Acta Cryst*. **2016**. 72, 171-179.

11) Su, J.; Windorff, C. J., Batista, E. R.; Evans, W. J.; Gaunt, A. J.; Janicke, M. T.; Kozimor, S. A.; Scott, B. L.; Woen, D. H.; Yang, P. Identification of the Formal +2 Oxidation State of Neptunium: Synthesis and Structural Characterization of $\{Np^{II}[C_5H_3(SiMe_3)_2]_3\}^{1-}$. *J. Am. Chem. Soc.* **2018**, 140, 7425-7428.

12) Chatterjee, S.; Hall, G. B.; Engelhard, M. H.; Du, Y.; Washton, N. M.; Lukens, W. W.; Lee, S.; Pearce, C. I.; Levitskaia, T. G. Spectroscopic Characterization of Aqua $[fac\text{-}Tc(CO)_3]^+$ Complexes at High Ionic Strength. *Inorg. Chem.* **2018**, 57, 12, 6903-6912.

13) Lukens, W. W.; Shuh, D. K.; Schroeder, N. C.; Ashley, K. R. Identification of the Non-Pertechnetate Species in Hanford Waste Tanks, Tc(I)−Carbonyl Complexes. *Environ. Sci. Technol.* **2004**, 38, 1, 229-233.

14) Blanchard, D. L.; Brown, G. N.; Conradson, S. D.; Fadeff, S. K.; Golcar, G. R.; Hess, N. J.; Klinger, G. S.; Kurath, D. E. Technetium in Alkaline, High-Salt, Radioactive Tank Waste Supernate: Preliminary Characterization and Removal; PNNL-11386; Pacific Northwest National Laboratory: **1997**.

15) Liddle, S. T. The Renaissance of Non-Aqueous Uranium Chemistry. *Angew. Chem. Int. Ed.* **2015**, 54, 8604–8641; *Angew. Chem.* **2015**, 127, 8726–8764.

16) Crosswhite, H. M.; Crosswhite, H.; Carnall, W. T.; Paszek, A. P. Spectrum analysis of $U^{3+}$:$LaCl_3$. *J. Chem. Phys.* **1980**, 72, 5103-5117.

17) Reilly, S. D.; Brown, J. L.; Scott, B. L.; Gaunt, A. J. Synthesis and characterization of $NpCl_4(DME)_2$ and $PuCl_4(DME)_2$ neutral transuranic An(iv) starting materials. *Dalton Trans.* **2014**, 43, 1498–1501.

18) Fieser, M. E.; Palumbo, C. T.; La Pierre, H. S.; Halter, D. P.; Voora, V. K.; Ziller, J. W.; Furche, F.; Meyer, K.; Evans, W. J. Comparisons of lanthanide/actinide +2 ions in a tris(aryloxide)arene coordination environment. *Chem. Sci.* **2017**, 8, 7424-7433.

19) Mansell, S. M.; Kaltsoyannis, N.; Arnold, P. L. Small Molecule Activation by Uranium Tris(aryloxides): Experimental and Computational Studies of Binding of N2, Coupling of CO, and Deoxygenation Insertion of $CO_2$ under Ambient Conditions. *J. Am. Chem. Soc.* **2011**, 133, 9036-9051.

20) Castro-Rodriguez, I.; Olsen, K.; Gantzel, P.; Meyer, K. Uranium Tris-aryloxide Derivatives Supported by Triazacyclononane: Engendering a Reactive Uranium(III) Center with a Single Pocket for Reactivity. *J. Am. Chem. Soc.* **2003**, 125, 4565-4571.

21) Inman, C. J.; Frey, A. S. P.; Kilpatrick, A. F. R.; Cloke, F. G. N.; Roe, S. M. Carbon Dioxide Activation by a Uranium(III) Complex Derived from a Chelating Bis(aryloxide) Ligand. *Organometallics* **2017**, 36, 4539-4545.

22) Hümmer, J.; Heinemann, F. W.; Meyer, K. Uranium Tetrakis-Aryloxide Derivatives Supported by Tetraazacyclododecane: Synthesis of Air-Stable, Coordinatively-Unsaturated U(IV) and U(V) Complexes. *Inorg. Chem.* **2017**, 56, 3201-3206.

23) Kosog, B.; La Pierre, H. S.; Heinemann, F. W.; Liddle, S. T.; Meyer, K. Synthesis of Uranium(VI) Terminal Oxo Complexes: Molecular Geometry Driven by the Inverse Trans-Influence. *J. Am. Chem. Soc.* **2012**, 134, 5284-5289.

24) Van der Sluys, W. G.; Sattelberger, A. P. Actinide alkoxide chemistry. *Chem. Rev.* **1990**, 90, 1027-1040.

25) McKee, S. D.; Burns, C. J.; Avens, L. R. Halide Effects in the Synthesis of Mixed Uranium(IV) Aryloxide−Halide Compounds. *Inorg. Chem.* **1998**, 37, 4040-4045.

26) Berg, J. M.; Clark, D. L.; Huffman, J. C.; Morris, D. E.; Sattelberger, A. P.; Streib, W. E.; Van der Sluys, W. G.; Watkin, J. G. Early actinide alkoxide chemistry. Synthesis, characterization, and molecular structures of thorium(IV) and uranium(IV) aryloxide complexes. *J. Am. Chem. Soc.* **1992**, 114, 10811-10821.

27) Mora, E.; Maria, L.; Biswas, B.; Camp, C.; Santos, I. C.; Pécaut, J; Cruz, A.; Carrestas, J. M.; Marçalo, J.; Mazzanti, M. Diamine Bis(phenolate) as Supporting Ligands in Organoactinide(IV) Chemistry. Synthesis, Structural Characterization, and Reactivity of Stable Dialkyl Derivatives. *Organometallics*, **2013**, 32, 1409-1422.

28) Rosenzweig, M. W.; Heinemann, F. W.; Maron, L.; Meyer, K. Molecular and Electronic Structures of Eight-Coordinate Uranium Bipyridine Complexes: A Rare Example of a $Bipy^{2-}$ Ligand Coordinated to a $U^{4+}$ Ion. *Inorg. Chem.*, **2017**, 56, 2792-2800.

29) Samulski, E. T.; Karraker, D. G. Some ethoxide compounds of neptunium. *J. Inorg. Nucl. Chem.* **1967**, 29, 993-996.

30) Behrle, A. C.; Levin, J. R.; Kim, J. E.; Drewett, J. M.; Barnes, C. L.; Schelter, E. J.; Walensky, J. R. Stabilization of $M^{IV}$ = Ti, Zr, Hf, Ce, and Th using a selenium bis(phenolate) ligand. *Dalton Trans.* **2015**, 44, 2693-2702.

31) Gray, D. L.; Backus, L. A.; Krug von Nidda, H.-A.; Skanthakumar, S.; Loidl, A.; Soderholm, L.; Ibers, J. A., A U(V) Chalcogenide: Synthesis, Structure, and Characterization of $K_2Cu_3US_5$. *Inorg. Chem.* **2007**, *46*, 6992-6996.

32) *APEX2 Suite*, Madison, WI, 2006.

33) Sheldrick, G. Crystal structure refinement with SHELXL. *Acta Crystallogr. C.* **2015**, *71*, 3-8.

34) Dolomanov, O. V.; Bourhis, L. J.; Gildea, R. J.; Howard, J. A. K.; Puschmann, H. OLEX2: a complete structure solution, refinement and analysis program. *J. Appl. Cryst.* **2009**, 42, 339-341.

35) Morales, M.A.; Jain, T.K.; Labhasetwar, V; Leslie-Pelecky, D.L. Magnetic studies of iron oxide nanoparticles coated with oleic acid and Pluronic® block copolymer. *J. Appl. Phys.* **2005**, *97*, 10Q905

36) Stoll, S.; Schweiger, A. EasySpin, a comprehensive software package for spectral simulation and analysis in EPR. *J. Magn. Reson.* **2006**, 178, 42-55.

37) Van der Sluys, W. G.; Sattelberger, A. P.; Streib, W. E.; Huffman, J. C. Tetrakis(2,6-di-t-butylphenoxy)uranium(IV): The first structurally characterized neutral homoleptic aryloxide complex of uranium(IV). *Polyhedron* **1989**, 8, 1247-1249.

38) Pyykkö, P. Additive covalent radii for single-, double-, and triple-bonded molecules and tetrahedrally bonded crystals: a summary. *J. Phys. Chem. A* **2015**, 119, 2326-2337.

39) Johnson, A. T.; Parker, T. G.; Dickens, S. M.; Pfeiffer, J. K.; Oliver, A. G.; Wall, D.; Wall, N. A.; Finck, M. R.; Carney, K. P. Synthesis and Crystal Structures of Volatile Neptunium(IV) β-Diketonates. *Inorg. Chem.* **2017**, 56, 13553-13561.

40) De Ridder, D. J. A.; Apostolidis, C.; Rebizant, J.; Kanellakopulos, B.; Maier, R. Tris($\eta^5$-cyclopentadienyl)phenolatoneptunium(IV). *Acta Crystallogr., Sect. C: Cryst. Struct. Commun.* **1996**, 52, 1436-1438.

41) Zhang, Z.; Parker, B. F.; Lohrey, T. D.; Teat, S. J.; Arnold, J.; Rao, L. Complexation-assisted reduction: complexes of glutaroimide-dioxime with tetravalent actinides (Np(iv) and Th(iv)). *Dalton Trans.* **2018**, 47, 8134-8141.

42) Magnani, N.; Apostolidis, C.; Morgenstern, A.; Colineau, E.; Griveau, J.-C.; Bolvin, H.; Walter, O.; Caciuffo, R. Magnetic Memory Effect in a Transuranic Mononuclear Complex. *Angew. Chem., Int. Ed.* **2011**, 50, 1696-1698.

43) Magnani, N.; Colineau, E.; Eloirdi, R., Griveau, J.-C., Caciuffo, R.; Cornet, S. M.; May, I.; Sharrad, C. A.; Collison, D.; Winpenny, R. E. P. Superexchange Coupling and Slow Magnetic Relaxation in a Transuranium Polymetallic Complex. *Phys. Rev. Lett.* **2010**, 104, 197202.

44) Jobiliong, A.; Oshima, Y.; Brooks, J. S.; Albrecht-Schmitt, T. E. Magnetism and electron spin resonance in single crystalline β-$AgNpO_2(SeO_3)$. *Solid State Commun.* **2004**, 132, 337-342.

45) Poirot, I.; Kot, W.; Shalimoff, G.; Edelstein, N.; Abraham, M. M.; Finch, C. B.; Boatner, L. A. Optical and EPR investigations of $Np^{4+}$ in single crystals of $ZrSiO_4$. *Phys. Rev. B: Condens. Matter Mater. Phys.* **1988**, 37, 3255-3264.

46) Amoretti, G.; Giori, D. C.; Schianchi, G.; Calestani, G.; Rizzoli, C.; Spirlet, J. C. Actinide and rare earth ions in single crystals of $ThO_2$: Preparation, EPR studies and related problems. *J. Less-Common Met.* **1986**, 122, 35-45.

47) Gamp, E.; Edelstein, N. Effects of small distortions on the EPR of the $\Gamma_6$ state ($T_d$ symmetry) of $Np(BH_3CH_3)_4$ diluted in $Zr(BH_3CH_3)_4$. *J. Chem. Phys.* **1984**, 80, 5963-5967.

48) Rajnak, K.; Banks, R. H.; Gamp, E.; Edelstein, N. Analysis of the optical spectrum of $Np(BD_4)_4$ diluted in $Zr(BD_4)4$ and the magnetic properties of $Np(BH_4)_4$ and $Np(BH_3CH_3)_4$. *J. Chem. Phys.* **1984**, 80, 5951-5962.

49) Butler, J. E.; Hutchison Jr., C. A. Electron paramagnetic resonance and electron nuclear double resonance of 237-neptunium hexafluoride in uranium hexafluoride single crystals. *J. Chem. Phys.* **1981**, 74, 3102 -3119.

50) Edelstein, N.; Kolbe, W.; Bray, J. E. Electron paramagnetic resonance spectrum of the $\Gamma_8$ ground state of $Np^{4+}$ diluted in $Cs_2ZrCl_6$. *Phys. Rev. B: Condens. Matter Mater. Phys.* **1980**, 21, 338-342.

51) Bray, J. E. Paramagnetic resonance of tetravalent neptunium-237 in single crystals of $Cs_2ZrCl_6$. *Phys. Rev. B: Condens. Matter Mater. Phys.* **1978**, 18, 2973-2977.

52) Richardson, R. P.; Gruber, J. B. Paramagnetic Resonance of Tetravalent Neptunium-237 in Single Crystals of $ThO_2$. *J. Chem. Phys.* **1972**, 56, 256-260.

53) Leung, A. F.; Wong, E. Y. Electron Paramagnetic Resonance of $NpO_2^{2+}$ in $Cs_2UO_2Cl_4$ and $CsUO_2(NO3)_3$. *Phys. Rev.* **1969**, 180, 380-385.

54) Gendron, F.; Páez-Hernández, D.; Notter, F.-P.; Pritchard, B.; Bolvin, H.; Autschbach, J. Magnetic Properties and Electronic Structure of Neptunyl(VI) Complexes: Wavefunctions, Orbitals, and Crystal-Field Models. *Chem. – Eur. J.* **2014**, 20, 7994-8011.

55) Páez-Hernández, D.; Bolvin, H. Magnetic properties of a fourfold degenerate state: $Np^{4+}$ ion diluted in $Cs_2ZrCl_6$ crystal. *J. Electron Spectrosc. Relat. Phenom.* **2014**, 194, 74-80.

56) Robinson, J. R.; Booth, C. H.; Carroll, P. J.; Walsh, P. J.; Schelter, E. J. Dimeric Rare-Earth BINOLate Complexes: Activation of 1,4-Benzoquinone through Lewis Acid Promoted Potential Shifts. *Chem. – Eur. J.* **2013**, 19, 5996-6004.

57) Werner, D.; Deacon, G. B.; Junk, P. C.; Anwander, R. Cerium(III/IV) Formamidinate Chemistry, and a Stable Cerium(IV) Diolate. *Chem. – Eur. J.* **2014**, 20, 4426-4438.

58) Hohloch, S.; Pankhurst, J. R.; Jaekel, E. E.; Parker, B. F.; Lussier, D. J.; Garner, M. E.; Booth, C. H.; Love, J. B.; Arnold, J. Benzoquinonoid-bridged dinuclear actinide complexes. *Dalton Trans.* **2017**, 46, 11615-11625.

59) Cotton, F. A.; Marler, D. O.; Schwotzer, W. Dinuclear uranium alkoxides. Preparation and structures of $KU_2(OCMe_3)_9$, $U_2(OCMe_3)_9$, and $U_2(OCHMe_2)_{10}$, containing [uranium(IV), uranium(IV)], [uranium(IV), uranium(V)], and [uranium(V), uranium(V)], respectively. *Inorg. Chem.* **1984**, 23, 4211-4215.

60) Fortier, S.; Wu, G.; Hayton, T. W. Synthesis and Characterization of Three Homoleptic Alkoxides of Uranium: $[Li(THF)]_2[U^{IV}(O^tBu)_6]$, $[Li(Et_2O)][U^{V}(O^tBu)_6]$, and $U^{VI}(O^tBu)_6$. *Inorg. Chem.* **2008**, 47, 4752-4761.

61) Brennan, J. G.; Anderson, R. A. Electron-Transfer Reactions of Trivalent Uranium. Preparation and Structure of $(MeC_5H_4)_3U{=}NPh$ and $[(MeC_5H_4)_3U]_2[\mu\text{-}\eta^1,\eta^2\text{-}PhNCO]$. *J. Am. Chem. Soc.* **1985**, 107, 514-516.

62) Nocton, G.; Horeglad, P.; Pécaut, J.; Mazzanti, M. Polynuclear Cation−Cation Complexes of Pentavalent Uranyl: Relating Stability and Magnetic Properties to Structure. *J. Am. Chem. Soc.* **2008**, 130, 16633-16645.

63) Spencer, L. P.; Schelter, E. J.; Yang, P.; Gdula, R. L.; Scott, B. L.; Thompson, J. D.; Kiplinger, J. L.; Batista, E. R.; Boncella, J. M. Cation-Cation Interactions, Magnetic Communication and Reactivity of the Pentavalent Uranium Ion $[U(NR)_2]^+$.*Angew. Chem., Int. Ed.* **2009**, 48, 3795-3798.

64) Morss, L. R.; Edelstein, N. M.; Fuger, J. *The Chemistry of the Actinide and Transactinide Elements*, Springer, Netherlands, **2006**, p. 2130

65) Seaman, L. A.; Walensky, J. R.; Wu, G.; Hayton, T. W. In Pursuit of Homoleptic Actinide Alkyl Complexes. *Inorg. Chem.* **2013**, 52, 3556-3564.

66) Fortier, S.; Melot, B. C.; Wu, G.; Hayton, T. W. Homoleptic Uranium(IV) Alkyl Complexes: Synthesis and Characterization. *J. Am. Chem. Soc.* **2009**, 131, 15512-15521.

67) Fortier, S.; Walensky, J. R.; Wu, G.; Hayton, T. W. High-Valent Uranium Alkyls: Evidence for the Formation of $U^{VI}(CH_2SiMe_3)_6$. *J. Am. Chem. Soc.* **2011**, 133, 11732-11743.

68) Pedrick, E. A.; Hrobarik, P.; Seaman, L. A.; Wu, G.; Hayton, T. W. Synthesis, structure and bonding of hexaphenyl thorium(iv): observation of a non-octahedral structure. *Chem. Commun.* **2016**, 52, 689-692.

69) Kraft, S. J.; Fanwick, P. E.; Bart, S. C. Carbon–Carbon Reductive Elimination from Homoleptic Uranium(IV) Alkyls Induced by Redox-Active Ligands. *J. Am. Chem. Soc.* 2012, 134, 6160-6168.

70) Johnson, S. A.; Kiernicki, J. J.; Fanwick, P. E.; Bart, S. C. New Benzylpotassium Reagents and Their Utility for the Synthesis of Homoleptic Uranium(IV) Benzyl Derivatives. *Organometallics*, **2015**, 34, 2889-2895.

71) Manriquez, J. M.; Fagan, P. J.; Marks, T. J.; Vollmer, S. H.; Day, C. S.; Day, V. W. Pentamethylcyclopentadienyl organoactinides. Trivalent uranium organometallic chemistry and the unusual structure of bis(pentamethylcyclopentadienyl)uranium monochloride. *J. Am. Chem. Soc.* **1979**, 101, 5075-5078.

72) Van der Sluys, W. G.; Burns, C. J.; Sattelberger, A. P. First example of a neutral homoleptic uranium alkyl. Synthesis, properties, and structure of $U[CH(SiMe_3)_2]_3$. *Organometallics* **1989**, 8, 855-857.

73) Di Bella, S.; Lanza, G.; Fragalà, I. L.; Marks, T. J. Electronic Structure and Photoelectron Spectroscopy of the Monomeric Uranium(III) Alkyl $[\eta^5\text{-}(CH_3)_5C_5]_2UCH[Si(CH_3)_3]_2$. *Organometallics*, **1996**, 15, 205-208.

74) Matson, E. M.; Forrest, W. P.; Fanwick, P. E.; Bart, S. C. Functionalization of Carbon Dioxide and Carbon Disulfide Using a Stable Uranium(III) Alkyl Complex. *J. Am. Chem. Soc.* **2011**, 133, 4948-4954.

75) Edwards, P. G.; Andersen, R. A.; Zalkin, A. Preparation of tetraalkyl phosphine complexes of the f-block metals. Crystal structure of $Th(CH_2Ph)_4(Me_2PCH_2CH_2PMe_2)$ and $U(CH_2Ph)_3Me(Me_2PCH_2CH_2PMe_2)$. *Organometallics* **1984**, 3, 293–298.

76) Seaman, L. A.; Pedrick, E. A.; Tsuchiya, T.; Wu, G.; Jakubikova, E.; Hayton, T. W. Comparison of the Reactivity of 2-Li-$C_6H_4CH_2NMe_2$ with $MCl_4$ (M=Th, U): Isolation of a Thorium Aryl Complex or a Uranium Benzyne Complex. *Angew. Chem. Int. Ed.* **2013**, 52, 10589-10592.

77) E. A. Pedrick , L. A. Seaman , J. C. Scott , L. Griego , G. Wu and T. W. Hayton , *Organometallics*, **2016**, 35 , 494-502.

78) Oakes, F. T.; Sebastian, J. F. Direct observation of metalated N,N-dimethylbenzylamines by ft NMR spectroscopy. *J. Organomet. Chem.* **1978**, 159, 363-371.

79) Lubben, T. V.; Ploessl, K.; Norton, J. R.; Miller, M. M.; Anderson, O. P. Synthesis and structure of two organozirconocenes with α nitrogen substituents. *Organometallics*, **1992**, 11, 122-127.

80) Cantat, T.; Scott, B. L.; Kiplinger, J. L. Convenient access to the anhydrous thorium tetrachloride complexes $ThCl_4(DME)_2$, $ThCl_4(1,4\text{-dioxane})_2$ and $ThCl_4(THF)_{3.5}$ using commercially available and inexpensive starting materials. *Chem. Commun*. **2010**, 46, 919-921.

81) Avens, L. R.; Bott, S. G.; Clark, D. L.; Sattelberger, A. P.; Watkin, J. G.; Zwick, B. D. A Convenient Entry into Trivalent Actinide Chemistry: Synthesis and Characterization of $AnI_3(THF)_4$ and $An[N(SiMe_3)_2]_3$ (An = U, Np, Pu). *Inorg. Chem.* **1994**, 33, 2248-2256.

82) Monreal, M. J.; Thomson, R. K.; Cantat, T.; Travia, N. E.; Scott, B. L.; Kiplinger, J. L. $UI_4(1,4\text{-dioxane})_2$, [$UCl_4$(1,4-dioxane)]2, and $UI_3(1,4\text{-dioxane})_{1.5}$: Stable and Versatile Starting Materials for Low- and High-Valent Uranium Chemistry. Organometallics **2011**, 30, 2031-2038.

83) Behrle, A. C.; Schmidt, J. A. R. Synthesis and Reactivity of Homoleptic α-Metalated N,N-Dimethylbenzylamine Rare-Earth-Metal Complexes. *Organometallics* **2011**, 30, 3915-3918.

84) Ives, C.; Fillis, E. L.; Hagadorn, J. R. Lithium, titanium and vanadium dithiocarboxylates. *Dalton Trans.* **2003**, 527-531.

85) Roger, M.; Arliguie, T.; Thuéry, P.; Fourmigué, M.; Ephritikhine, M. Homoleptic Tris(dithiolene) and Tetrakis(dithiolene) Complexes of Uranium(IV). *Inorg. Chem.* **2005**, 44, 594-600.

86) Moro, F.; Mills, D. P.; Liddle, S. T.; van Slageren, J. The Inherent Single-Molecule Magnet Character of Trivalent Uranium. *Angew. Chem., Int. Ed.* 2013, 52, 3430-3433.

87) Meihaus, K. R.; Rinehart, J. D.; Long, J. R. Dilution-Induced Slow Magnetic Relaxation and Anomalous Hysteresis in Trigonal Prismatic Dysprosium(III) and Uranium(III) Complexes. *Inorg. Chem.* **2011**, 50, 8484-8489.

88) Rinehart, J. D.; Long, J. R. Slow Magnetic Relaxation in a Trigonal Prismatic Uranium(III) Complex. *J. Am. Chem. Soc.* **2009**, 131, 12558-12559.

89) Ortu, F.; Formanuik, A.; Innes, J. R.; Mills, D. P. New vistas in the molecular chemistry of thorium: low oxidation state complexes. *Dalton Trans.*, 2016, 45, 7537-7549.

90) Evans, W. J.; Walensky, J. R.; Ziller, J. W. Synthesis of a Thorium Tuck-In Complex, [($\eta^5$:$\eta^1$-$C_5Me_4CH_2$)($\eta^5$-$C_5Me_5$)Th{iPrNC(Me)NiPr}], by C-H Bond Activation Initiated by $(C_5Me_5)^-$. *Chem. – Eur. J.* **2009**, 15, 12204-12207.

91) Siladke, N. A.; Webster, C. L.; Walensky, J. R.; Takase, M. K.; Ziller, J. W.; Grant, D. J.; Gagliardi L.; Evans, W. J. Actinide Metallocene Hydride Chemistry: C–H Activation in Tetramethylcyclopentadienyl Ligands to Form [μ-$\eta^5$-$C_5Me_3H(CH_2)$-κC]$^{2-}$ Tuck-over Ligands in a Tetrathorium Octahydride Complex. *Organometallics*, **2013**, 32, 6522-6531.

92) Jantunen, K. C.; Burns, C. J.; Castro-Rodriguez, I.; Da Re, R. E.; Golden, J. T.; Morris, D. E.; Scott, B. L.; Taw, F. L.; Kiplinger, J. L. Thorium(IV) and Uranium(IV) Ketimide Complexes Prepared by Nitrile Insertion into Actinide−Alkyl and −Aryl Bonds. *Organometallics*, **2004**, 23, 4682-4692.

93) Brown, D.; Holah, D. G.; Rickard, C. E. F. Structure of thorium(IV) tetrakis-(NN-diethyldithiocarbamate). *J. Chem. Soc. A*, **1970**, 423-425.

94) Macor, J. A.; Brown, J. L.; Cross, J. N.; Daly, S. R.; Gaunt, A. J.; Girolami, G. S.; Janicke, M. T.; Kozimor, S. A.; Neu, M. P.; Olson, A. C.; Reilly, S. D.; Scott, B. L. Coordination chemistry of 2,2′-biphenylenedithiophosphinate and diphenyldithiophosphinate with U, Np, and Pu. *Dalton Trans.* **2015**, 44, 18923-18936.

95) Clark, D. L.; Miller, M. M.; Watkin, J. G. Synthesis, characterization, and x-ray structure of the uranium thiolate complex $U(S\text{-}2,6\text{-}Me_2C_6H_3)[N(SiMe_3)_2]_3$. *Inorg. Chem.* **1993**, 32, 772-774.

96) Andersen, R. A. Tris((hexamethyldisilyl)amido)uranium(III): preparation and coordination chemistry. *Inorg. Chem.* **1979**, 18, 1507-1509.

97) Baker, R. J. The coordination and organometallic chemistry of $UI_3$ and $U\{N(SiMe_3)_2\}_3$: Synthetic reagents par excellence. *Coord. Chem. Rev.* **2012**, 256, 2843-2871.

98) Behrle, A. C.; Kerridge, A.; Walensky, J. R. Dithio- and Diselenophosphinate Thorium(IV) and Uranium(IV) Complexes: Molecular and Electronic Structures, Spectroscopy, and Transmetalation Reactivity. *Inorg. Chem.* **2015**, 54, 11625-11636.

99) Pinkerton, A. A.; Storey, A. E.; Zellweger, J.-M. Dithiophosphinate complexes of the actinides. Part 1. Preparation and characterisation of complexes of thorium(IV) and

the crystal structures of [Th($S_2PR_2$)$_4$], R = Me or $C_6H_{11}$. *J. Chem. Soc., Dalton Trans.*, **1981**, 1475-1480.

100) Shannon, R. Revised effective ionic radii and systematic studies of interatomic distances in halides and chalcogenides. *Acta Crystallogr., Sect. A* **1976**, 32, 751−767.

101) Mond, L.; Langer, C.; Quincke, F. Action of carbon monoxide on nickel. *J. Chem. Soc. Trans*. **1890**, 57, 749–753.

102) Kealy, T. J.; Pauson, P. L. A New Type of Organo-Iron Compound. *Nature* **1951**, 168, 1039-1040.

103) Schrock, R. R. Multiple metal-carbon bonds for catalytic metathesis reactions (Nobel Lecture). *Angew. Chem. Int. Ed.* **2006**, 45, 3748–3759; *Angew. Chem.* **2006**, 118, 3832–3844.

104) Grubbs, R. H. Olefin-metathesis catalysts for the preparation of molecules and materials (Nobel Lecture). *Angew. Chem. Int. Ed.* **2006**, 45, 3760–3765; *Angew. Chem*. **2006**, 118, 3845–3850.

105) Stollenz, M.; Meyer, F. Mesitylcopper – A Powerful Tool in Synthetic Chemistry. *Organometallics* **2012**, 31, 7708–7727.

106) Hillard, E. A.; Jaouen, G. Bioorganometallics: Future Trends in Drug Discovery, Analytical Chemistry, and Catalysis. *Organometallics* **2011**, 30, 20–27.

107) Ephritikhine, E. M. The vitality of uranium molecular chemistry at the dawn of the XXIst century. *Dalton Trans.* **2006**, 2501–2516.

108) Liddle, S. T. The Renaissance of Non-Aqueous Uranium Chemistry. *Angew. Chem. Int. Ed.* **2015**, 54, 8604–8641; *Angew. Chem.* **2015**, 127, 8726–8764.

109) Ephritikhine, M. Recent Advances in Organoactinide Chemistry As Exemplified by Cyclopentadienyl Compounds. *Organometallics* **2013**, 32, 2464–2488.

110) Jones, M. B.; Gaunt, A. J. Recent Developments in Synthesis and Structural Chemistry of Nonaqueous Actinide Complexes. *Chem. Rev*. **2013**, 113, 1137−1198.

111) Langeslay, R. R.; Fieser, M. E.; Ziller, J. W.; Furche, F.; Evans, W. J. Synthesis, structure, and reactivity of crystalline molecular complexes of the $\{[C_5H_3(SiMe_3)_2]_3Th\}^{1-}$ anion containing thorium in the formal +2 oxidation state. *Chem. Sci.* **2015**, 6, 517–521.

112) MacDonald, M. R.; Fieser, M. E.; Bates, J. E.; Ziller, J. W.; Furche, F.; Evans, W. J. Identification of the +2 Oxidation State for Uranium in a Crystalline Molecular Complex, [K(2.2.2-Cryptand)][$(C_5H_4SiMe_3)_3U$]. *J. Am. Chem. Soc.* **2013**, 135, 13310–13313.

113) La Pierre, H. S.; Scheurer, A.; Heinemann, F. W.; Hieringer, W.; Meyer, K. Synthesis and characterization of a uranium(II) monoarene complex supported by δ backbonding. *Angew. Chem. Int. Ed.* **2014**, 53, 7158–7162; *Angew. Chem.* **2014**, 126, 7286–7290.

114) Windorff, C. J.; MacDonald, M. R.; Meihaus, K. R.; Ziller, J. W.; Long, J. R.; Evans, W. J. Expanding the Chemistry of Molecular $U^{2+}$ Complexes: Synthesis, Characterization, and Reactivity of the $\{[C_5H_3(SiMe_3)_2]_3U\}-$ Anion. *Chem. - Eur. J.* **2016**, 22, 772–782.

115) Dutkiewicz, M. S.; Farnaby, J. H.; Apostolidis, C.; Colineau, E.; Walter, O.; Magnani, N.; Gardiner, M. G.; Love, J. B.; Kaltsoyannis, N.; Caciuffo, R.; Arnold, P. L. Organometallic neptunium(III) complexes. *Nat. Chem.* **2016**, 8, 797-802.

116) Windorff, C. J.; Chen, G. P.; Cross, J. N.; Evans, W. J.; Furche, F.; Gaunt, A. J.; Janicke, M. T.; Kozimor, S. A.; Scott, B. L. Identification of the Formal +2 Oxidation State of Plutonium: Synthesis and Characterization of $\{Pu^{II}[C_5H_3(SiMe_3)_2]_3\}^-$. *J. Am. Chem. Soc.* **2017**, 139, 3970–3973.

117) Goodwin, C.; Su, J.; Albrecht-Schmitt, T.; Blake, A.; Batista, E.; Daly, S.; Dehnen, S.; Evans, W.; Gaunt, A.; Kozimor, S.; Lichtenberger, N.; Scott, B.; Yang, P. $[Am(C_5Me_4H)_3]$: An Organometallic Americium Complex. *Angew. Chem. Int. Ed.* **2019**, 58, 11695–11699; *Angew. Chem.* **2019**, 131, 11821–11825.

118) Marks, T. J.; Seyam, A. M. Observations on the thermal decomposition of some uranium(IV) tetraalkyls. *J. Organomet. Chem.* **1974**, 67, 61–66.

119) Marks, T. J. in Progress in Inorganic Chemistry. Chemistry and Spectroscopy of f-Element Organometallics Part II,: the Actinides (Ed.: S. J. Lippard), Wiley, New York, **1979**.

120) Sigurdson, E. R.; Wilkinson, G. Lithium alkyl anions of uranium(IV) and uranium(V). Addition compounds of uranium(VI) hexaisopropoxide with lithium, magnesium, and aluminium alkyls. *J. Chem. Soc. Dalton* **1977**, 812–818.

121) Marks, T. J.; Wachter, W. A. Tris($\eta^5$-cyclopentadienyl)alkyl and -alkenyl compounds of thorium(IV). *J. Am. Chem. Soc.* **1976**, 98, 703–710.

122) Marks, T. J.; Seyam, A. M. Stable uranium(IV) alkyl and aryl complexes. *J. Am. Chem. Soc.* **1972**, 94, 6545–6546.

123) Manriquez, J. M.; Fagan, P. J.; Marks, T. J.; Vollmer, S. H.; Day, C. S.; Day, V. W. Pentamethylcyclopentadienyl organoactinides. Trivalent uranium organometallic

chemistry and the unusual structure of bis(pentamethylcyclopentadienyl)uranium monochloride. *J. Am. Chem. Soc.* **1979**, 101, 5075–5078.

124) Edwards, P. G.; Andersen, R. A.; Zalkin, A. Preparation of tetraalkyl phosphine complexes of the f-block metals. Crystal structure of $Th(CH_2Ph)_4(Me_2PCH_2CH_2PMe_2)$ and $U(CH_2Ph)_3Me(Me_2PCH_2CH_2PMe_2)$. *Organometallics* **1984**, 3, 293–298.

125) Behrle, A. C.; Myers, A. J.; Rungthanaphatsophon, P.; Lukens, W. W.; Barnes, C. L.; Walensky, J. R. Uranium(iii) and thorium(iv) alkyl complexes as potential starting materials. *Chem. Commun.* **2016**, 52, 14373–14375.

126) Boreen, M. A.; Parker, B. F.; Lohrey, T. D.; Arnold, J. A Homoleptic Uranium(III) Tris(aryl) Complex. J. Am. Chem. *Soc*. **2016**, 138, 15865–15868.

127) Arnaudet, L.; Charpin, P.; Folcher, G.; Lance, M.; Nierlich, M.; Vigner, D. Characterization of the anion $[(\eta^5\text{-}C_5H_5)_3\ U^{III}\text{-}n\text{-}C_4H_9]^-$. Synthesis and crystal structure of tricyclopentadienyl n-butyluranium(III) lithium cryptate: $[(C_5H_5)_3UC_4H_9]^-$ $[LiC_{14}H_{28}N_2O_4]^+$. *Organometallics* **1986**, 5, 270–274.

128) Evans, W. J.; Traina, C. A.; Ziller, J. W. Synthesis of Heteroleptic Uranium $(\mu\text{–}\eta^6\text{:}\eta^6\text{-}C_6H_6)^{2-}$ Sandwich Complexes via Facile Displacement of $(\eta^5\text{-}C_5Me_5)^{1-}$ by Ligands of Lower Hapticity and Their Conversion to Heteroleptic Bis(imido) Compounds. *J. Am. Chem. Soc.* **2009**, 131, 17473–17481.

129) Matson, E. M.; Forrest, W. P.; Fanwick, P. E.; Bart, S. C. Use of Alkylsodium Reagents for the Synthesis of Trivalent Uranium Alkyl Complexes. *Organometallics* **2012**, 31, 4467–4473.

130) Matson, E. M.; Forrest, W. P.; Fanwick, P. E.; Bart, S. C. Synthesis and Reactivity of Trivalent Tp*U($CH_2Ph)_2$(THF): Insertion vs Oxidation at Low-Valent Uranium. *Organometallics* **2013**, 32, 1484–1492.

131) Matson, E. M.; Kiernicki, J. J.; Fanwick, P. E.; Bart, S. C. Expanding the Family of Uranium(III) Alkyls: Synthesis and Characterization of Mixed-Ligand Derivatives. Eur. J. Inorg. Chem. **2016**, 2527–2533.

132) Tatebe, C. J.; Johnson, S. A.; Zeller, M.; Bart, S. C. Generation of Tp*2U(N3) from a family of new uranium(III) alkyl complexes. *J. Organomet. Chem.* **2018**, 857, 152–158.

133) La Pierre, H. S.; Meyer, K. in Progress in Inorganic Chemistry, Vol. 58. Activation of Small Molecules by Molecular Uranium Complexes, Wiley, New York, **2014**.

134) Arnold, P. L. Uranium-mediated activation of small molecules. *Chem. Commun.* **2011**, 47, 9005–9010.

135) Liddle, S. T.; van Slageren, J. Improving f-element single molecule magnets. *Chem. Soc. Rev.* **2015**, 44, 6655– 6669.

136) Johnson, S. A.; Bart, S. C. Achievements in uranium alkyl chemistry: celebrating sixty years of synthetic pursuits. *Dalton Trans.* **2015**, 44, 7710–7726.

137) Walter, O. Actinide Organometallic Complexes with π-Ligands. *Chem. - Eur. J.* **2019**, 25, 2927–2934.

138) Ibers, J. Neglected Neptunium. *Nat. Chem.* **2010**, 2, 996.

139) Arnold, P. L.; Dutkiewicz, M. S.; Walter, O. Organometallic Neptunium Chemistry. *Chem. Rev.* **2017**, 117, 11460−11475.

140) Zwick, B. D. in Transuranium Elements: A Half Century. Transuranium Organometallics Elements: The Next Generation. (Eds.: L. R. Morss, J. Fuger), American Chemical Society, Washington, DC, **1992**.

141) Karraker, D. G. in Organometallics of the f-Elements. Proceedings of the NATO Advanced Study Institute held at Sogesta, Urbino, Italy, September 11–22, 1978 (Eds.: T. J. Marks, R. D. Fischer), Springer, Dordrecht, **1979**.

142) Dutkiewicz, M. S.; Apostolidis, C.; Walter, O.; Arnold, P. L. Reduction chemistry of neptunium cyclopentadienide complexes: from structure to understanding. *Chem. Sci.* **2017**, 8, 2553–2561.

143) Bolander, R. Kernforschungszentrum Karlsruhe GmbH (Germany, F. R.). Inst. Fuer Heisse Chemie; Karlsruhe Univ. (T. H.) (Germany, F. R.), Fakultaet fuer Chemie **1986**.

144) Pattenaude, S. A.; Anderson, N. H.; Bart, S. C.; Gaunt, A. J.; Scott, B. L. Non-aqueous neptunium and plutonium redox behaviour in THF – access to a rare Np(iii) synthetic precursor. *Chem. Commun.* **2018**, 54, 6113–6116.

145) Dickie, D. A.; Lee, P. T. K.; Labeodan, O. A.; Schatte, G.; Weinberg. N.; Lewis, A. R.; Bernard, G. M.; Wasylishen, R. E.; Clyburne, J. A. C. Flexible coordination of the carboxylate ligand in tin(ii) amides and a 1,3-diaza-2,4-distannacyclobutanediyl. *Dalton Trans*. **2007**, 27, 2862-2869.

146) Schrock, R. R.; Parshall, G. W. σ-Alkyl and -Aryl Complexes of the Group 4-7 Transition Metals. *Chem. Rev.* **1976**, 76, 243–268.

147) Jana, R.; Pathak, T. P.; Sigman, M. S. Advances in Transition Metal (Pd,Ni,Fe)-Catalyzed Cross-Coupling Reactions Using Alkyl-organometallics as Reaction Partners. *Chem. Rev.* **2011**, 111, 1417–1492.

148) Gaunt, A. J.; Enriquez, A. E.; Reilly, S. D.; Scott, B. L.; Neu, M. P. Structural Characterization of $Pu[N(SiMe_3)_2]_3$, a Synthetically Useful Nonaqueous Plutonium(III) Precursor. *Inorg. Chem.* **2008**, 47, 26–28.

149) Gaunt, A. J.; Reilly, S. D.; Enriquez, A. E.; Scott, B. L.; Ibers, J. A.; Sekar, P.; Ingram, K. I. M.; Kaltsoyannis, N.; Neu, M. P. Experimental and Theoretical Comparison of Actinide and Lanthanide Bonding in $M[N(EPR_2)_2]_3$ Complexes (M = U, Pu, La, Ce; E = S, Se, Te; R = Ph, iPr, H). *Inorg. Chem.* **2008**, 47, 29−41.

150) Mazzanti, M.; Wietzke, R.; Pcaut, J.; Latour, J.-M.; Maldivi, P.; Remy, M. Structural and Density Functional Studies of Uranium(III) and Lanthanum(III) Complexes with a Neutral Tripodal N-Donor Ligand Suggesting the Presence of a U−N Back-Bonding Interaction. *Inorg. Chem.* **2002**, 41, 2389–2399.

151) Roger, M.; Barros, N.; Arliguie, T.; Thury, P.; Maron, L.; Ephritikhine, M. U(SMes*)n, (n = 3, 4) and Ln(SMes*)3 (Ln = La, Ce, Pr, Nd): Lanthanide(III)/Actinide(III) Differentiation in Agostic Interactions and an Unprecedented η3 Ligation Mode of the Arylthiolate Ligand, from X-ray Diffraction and DFT Analysis. *J. Am. Chem. Soc.* 2006, 128, 8790– 8802.

152) Jones, M. B.; Gaunt, A. J.; Gordon, J. C.; Kaltsoyannis, N.; Neu, M. P.; Scott, B. L. Uncovering f-element bonding differences and electronic structure in a series of 1 : 3 and 1 : 4 complexes with a diselenophosphinate ligand. *Chem. Sci.* **2013**, 4, 1189–1203.

153) Galley, S. S.; Arico, A. A.; Lee, T.-H.; Deng, X.; Yao, Y.-X.; Sperling, J. M.; Proust, V.; Storbeck, J. S.; Dobrosavljevic, V.; Neu, J. N.; Siegrist, T.; Baumbach, R. E.; Albrecht-Schmitt, T. E.; Kaltsoyannis, N.; Lanat, N. Uncovering the Origin of Divergence in the CsM(CrO4)2 (M = La, Pr, Nd, Sm, Eu; Am) Family through Examination of the Chemical Bonding in a Molecular Cluster and by Band Structure Analysis. *J. Am. Chem. Soc.* **2018**, 140, 1674–1685.

154) Dan, D.; Celis-Barros, C.; White, F. D.; Sperling, J. M.; Albrecht-Schmitt, T. E. Origin of Selectivity of a Triazinyl Ligand for Americium(III) over Neodymium(III). *Chem. - Eur. J.* **2019**, 25, 3248–3252.

155) Brown, D.; Holah, D. G.; Rickard, C. E. F. N,N-diethyldithiocarbamate complexes of trivalent lanthanide and actinide elements and the crystal structure of tetraethylammonium neptunium(III) tetrakis-(N,N-diethyldithiocarbamate). *J. Chem. Soc. A* **1970**, 786−790.

156) Amoretti, G., Calculation of the Stevens factors α, β and γ in the intermediate coupling scheme for U and Np ions with f2, f3 and f4 configurations. *J. Phys.* **1984**, 45, 1067–1069.

157) Gendron, F.; Autschbach, J. Puzzling Lack of Temperature Dependence of the $PuO_2$ Magnetic Susceptibility Explained According to Ab Initio Wave Function Calculations. *J. Phys. Chem. Lett.* **2017**, 8, 673– 678.

158) Raphael, G.; Lallement R. Susceptibilite magnetique de PuO2. *Solid State Commun.* **1968**, 6, 383–385.

159) Hutchison, C. A.; Candela, G. A. Magnetic Susceptibilities of Uranium (IV) Ions in Cubic Crystalline Fields. *J. Chem. Phys.* **1957**, 27, 707– 710.

160) Satten, R. A.; Schreiber, C. L.; Wong, E. Y. Energy Levels of $U^{4+}$ in an Octahedral Crystalline Field. *J. Chem. Phys.* **1965**, 42, 162–171.

161) Lukens, W. W.; Beshouri, S. M.; Blosch, L. L.; Stuart, A. L.; Andersen, R. A. Preparation, Solution Behavior, and Solid-State Structures of $(1,3\text{-}R_2C_5H_3)_2UX_2$, Where R Is $CMe_3$ or $SiMe_3$ and X Is a One-Electron Ligand. *Organometallics* **1999**, 18, 1235-1246.

162) Galley, S. S.; Sperling, J. M.; Windorff, C. J.; Zeller, M.; Albrecht-Schmitt, T. E.; Bart, S. C. Conversion of Americia to Anhydrous Trivalent Americium Halides. *Organometallics* **2019**, 38, 606–609.

163) Ehlers, A. W.; Baerends, E. J.; Lammertsma, K. Nucleophilic or Electrophilic Phosphinidene Complexes $ML_n$=PH; What Makes the Difference? *J. Am. Chem. Soc.* **2002**, 124, 2831–2838.

164) Stafford, H.; Rookes, T. M.; Wildman, E. P.; Balázs, G.; Wooles, A. J.; Scheer, M.; Liddle, S. T. Terminal Parent Phosphanide and Phosphinidene Complexes of Zirconium(IV). *Angew. Chem. Int. Ed*. **2017**, 56, 7669–7673

165) Ingram, K. I. M.; Tassell, M. J.; Gaunt, A. J.; Kaltsoyannis, N. Covalency in the f Element−Chalcogen Bond. Computational Studies of $M[N(EPR_2)_2]_3$ (M = La, Ce, Pr, Pm, Eu, U, Np, Pu, Am, Cm; E = O, S, Se, Te; R = H, iPr, Ph). *Inorg. Chem.* **2008**, 47, 7824−7833.

166) Lukens, W. W.; Edelstein, N. M.; Magnani, N.; Hayton, T. W.; Fortier, S.; Seaman, L. A. Quantifying the σ and π Interactions between U(V) f Orbitals and Halide, Alkyl, Alkoxide, Amide and Ketimide Ligands. *J. Am. Chem. Soc*. **2013**, 135, 10742−10754.

167) Minasian, S. G.; Keith, J. M.; Batista, E. R.; Boland, K. S.; Clark, D. L.; Conradson, S. D.; Kozimor, S. A.; Martin, R. L.; Schwarz, D. E.; Shuh, D. K.; Wagner, G. L.; Wilkerson, M. P.; Wolfsberg, L. E.; Yang, P. Determining Relative f and d Orbital Contributions to M−Cl Covalency in $MCl_6^{2-}$ (M = Ti, Zr, Hf, U) and $UOCl^{5-}$ Using Cl KEdge X-ray Absorption Spectroscopy and Time-Dependent Density Functional Theory. *J. Am. Chem. Soc.* **2012**, 134, 5586−5597.

168) Kaltsoyannis, N. Does Covalency Increase or Decrease across the Actinide Series? Implications for Minor Actinide Partitioning. *Inorg. Chem*. **2013**, 52, 3407−3413.

169) Behrle, A. C.; Myers, A. J.; Kerridge, A.; Walensky, J. R. Coordination Chemistry and QTAIM Analysis of Homoleptic Dithiocarbamate Complexes, $M(S_2CN^iPr_2)_4$ (M = Ti, Zr, Hf, Th, U, Np). *Inorg. Chem.* **2018**, 57, 17, 10518-10524

170) Arnold, P. L.; McMullon, M. W.; Kühn, F. E.; Rieb, J. C-H bond activation by f-block complexes. *Angew. Chem., Int. Ed.* **2015**, 54, 82-100.

171) Peterman, D. R.; Law, J. D.; Todd, T. A; Tillotson, R. D. In Separations for the Nuclear Fuel Cycle in the 21st Century; Lumetta, G. J., Ed,; American Chemical Society: Washington, DC. **2006**; 251

172) Myers, A. J.; Tarlton, M. L.; Kelley, S. P.; Lukens, W. W.; Walensky, J. R. Synthesis and Utility of a Neptunium(III) Hydrocarbyl Complex. *Angew. Chem. Int. Ed.* **2019**, 58, 14891.

173) Avens, L. R.; Barnhart, D. M.; Burns, C. J.; McKee, S. D.; Smith, W. H. Oxidation Chemistry of a Uranium(III) Aryloxide. *Inorg. Chem.* **1994**, 33, 4245-4254.

174) Fox, A. R.; Arnold, P. L.; Cummins, C. C. Uranium−Nitrogen Multiple Bonding: Isostructural Anionic, Neutral, and Cationic Uranium Nitride Complexes Featuring a Linear U═N═U Core *J. Am. Chem. Soc.* **2010**, 132, 10, 3250-3251.

175) Matson, E. M.; Breshears, A. T.; Kiernicki, J. J.; Newell, B. S.; Fanwick, P. E.; Shores, M. P.; Walensky, J. R.; Bart, S. C. Trivalent Uranium Phenylchalcogenide Complexes: Exploring the Bonding and Reactivity with $CS_2$ in the $Tp^*_2UEPh$ Series (E = O, S, Se, Te). *Inorg. Chem.* **2014**, 53, 12977−12985.

176) Walensky, J. R.; Martin, R. L.; Ziller, J. W.; Evans, W. J. Importance of Energy Level Matching for Bonding in $Th^{3+}$-$Am^{3+}$ Actinide Metallocene Amidinates, $(C_5Me_5)_2[^{iPr}NC(Me)N^{iPr}]An$. *Inorg. Chem.* **2010**, 49, 10007−10012.

177) Wrobleski, D. A.; Ryan, R. R.; Wasserman, H. J.; Salazar, K. V.; Paine, R. T.; Moody, D. C. Synthesis and characterization of bis(diphenylphosphido)bis(pentamethylcyclopentadienyl)thorium(IV),$[(\eta^5\text{-}C_5(CH_3)_5]_2Th(PPh_2)_2$. *Organometallics* **1986**, 5, 90−94.

178) Ortu, F.; Formanuik, A.; Innes, J. R.; Mills, D. P. New vistas in the molecular chemistry of thorium: low oxidation state complexes. *Dalton Trans.* **2016**, 45, 7537−7549.

179) Lam, O. P.; Anthon, C.; Heinemann, F. W.; O'Connor, J. M.; Meyer, K. Structural and Spectroscopic Characterization of a Charge Separated Uranium Benzophenone Ketyl Radical Complex. *J. Am. Chem. Soc*. **2008**, 130, 6567−6576.

180) Ren, W.; Zi, G.; Walter, M. D. Synthesis, Structure, and Reactivity of a Thorium Metallocene Containing a 2,2′Bipyridyl Ligand. *Organometallics* **2012**, 31, 672−679.

181) Behrle, A. C.; Walensky, J. R. Insertion of tBuNC into thoriumphosphorus and thorium-arsenic bonds: phosphaazaallene and arsaazaallene moieties in f element chemistry. *Dalton Trans.* **2016**, 45, 10042−10049.

182) Behrle, A. C.; Castro, L.; Maron, L.; Walensky, J. R. Formation of a Bridging Phosphinidene Thorium Complex. *J. Am. Chem. Soc.* **2015**, 137, 14846−14849.

183) Hall, S. W.; Huffman, J. C.; Miller, M. M.; Avens, L. R.; Burns, C. J.; Sattelberger, A. P.; Arney, D. S. J.; England, A. F. Synthesis and characterization of bis(pentamethylcyclopentadienyl)uranium(IV) and -thorium(IV) compounds containing the bis(trimethylsilyl)phosphide ligand. *Organometallics* **1993**, 12, 752−758.

184) Hou, Z.; Stephan, D. W. Generation and reactivity of the first mononuclear early metal phosphinidene complex, $Cp^*_2Zr{:}P(C_6H_2Me_3\text{-}2,4,6)$. *J. Am. Chem. Soc.* **1992**, 114, 10088−10089.

185) Yang, P.; Zhou, E.; Hou, G.; Zi, G.; Ding, W.; Walter, M. D. Experimental and Computational Studies on the Formation of Thorium−Copper Heterobimetallics. *Chem. - Eur. J.* **2016**, 22, 13845−13849.

186) Erickson, K. A.; Kagan, B. D.; Scott, B. L.; Morris, D. E.; Kiplinger, J. L. Revisiting the bis(dimethylamido) metallocene complexes of thorium and uranium: improved syntheses, structure, spectroscopy, and redox energetics of $(C_5Me_5)_2An(NMe_2)_2$ (An = Th, U). *Dalton Trans.* **2017**, 46, 11208−11213.

187) Bartlett, R. A.; Olmstead, M. M.; Power, P. P.; Sigel, G. A. Synthesis and spectroscopic and x-ray structural studies of the mesitylphosphines $Ph_2Mes$ and $PHMes_2$ (Mes = 2,4,6-$Me_3C_6H_2$) and their lithium salts $[Li(THF)_3PHMes]$ and $[\{Li(OEt_2)PMes_2\}_2]$. *Inorg. Chem.* **1987**, 26, 1941−1946.

188) Becker, G.; Mundt, O.; Rössler, M.; Schneider, E. Bildung und Eigenschaften von Acylphosphanen. VI. Synthese von Alkyl- und Arylbis (trimethylsilyl)- sowie Alkyl und Aryltrimethylsilyphosphanen. *Z. Anorg. Allg. Chem*. **1978**, 443, 42−52.

189) Ishiyama, T.; Mizuta, T.; Miyoshi, K.; Nakazawa, H. Synthesis and Characterization of Some Zirconium and Hafnium Complexes with a Phosphide-Pendant Cyclopentadienyl Ligand. *Organometallics* **2003**, 22, 1096−1105.

190) Fagan, P. J.; Manriquez, J. M.; Maatta, E. A.; Seyam, A. M.; Marks, T. J. Synthesis and properties of bis(pentamethylcyclopentadienyl) actinide hydrocarbyls and hydrides. A new class of highly reactive f-element organometallic compounds. *J. Am. Chem. Soc*. **1981**, 103, 6650−6667.

191) Gilman, H.; Pacevitz, H. A.; Baine, O. Benzylalkali Compounds. *J. Am. Chem. Soc.* **1940**, 62, 1514−1520.

192) Lin, Z.; Marks, T. J. Metal, bond energy, and ancillary ligand effects on actinide-carbon.sigma.-bond hydrogenolysis. A kinetic and mechanistic study. *J. Am. Chem. Soc*. **1987**, 109, 7979−7985.

193) Toscano, P. J.; Marks, T. J. Dicyclopentadienyldimethylthorium/silica surface chemistry. High-resolution carbon-13 CPMAS NMR evidence for alkylation of surface silicon sites. *Langmuir* **1986**, 2, 820−823.

194) te Velde, G.; Bickelhaupt, F. M.; Baerends, E. J.; Fonseca Guerra, C.; van Gisbergen, S. J. A.; Snijders, J. G.; Ziegler, T. Chemistry with ADF. *J. Comput. Chem.* **2001**, 22, 931−967.

195) ADF; SCM, Theoretical Chemistry, Vrije Universiteit, Amsterdam, The Netherlands, **2017**; http://www.scm.com.

196) Lenthe, E. v.; Baerends, E. J.; Snijders, J. G. Relativistic regular two-component Hamiltonians. *J. Chem. Phys*. **1993**, 99, 4597−4610.

197) Perdew, J. P.; Burke, K.; Ernzerhof, M. Generalized Gradient Approximation Made Simple. *Phys. Rev. Lett*. **1996**, 77, 3865−3868.

198) Van Lenthe, E.; Baerends, E. J. Optimized Slater-type basis sets for the elements 1−118. *J. Comput. Chem*. **2003**, 24, 1142−1156.

199) Yanai, T.; Tew, D. P.; Handy, N. C. A new hybrid exchange− correlation functional using the Coulomb-attenuating method (CAMB3LYP). *Chem. Phys. Lett.* **2004**, 393, 51−57.

200) Yasui, S.; Ogawa, Y.; Shioji, K.; Mishima, M.; Yamazaki, S. Dramatic Effect of Atmosphere on Product Distribution from SteadyState Photolysis of Triarylphosphines. *Bull. Chem. Soc. Jpn.* **2014**, 87, 988−996.

201) Elrod, L. T.; Boxwala, H.; Haq, H.; Zhao, A. W.; Waterman, R. As−As Bond Formation via Reductive Elimination from a Zirconocene Bis(dimesitylarsenide) Compound. *Organometallics* **2012**, 31, 5204− 5207.

202) Evans, W. J.; Walensky, J. R.; Ziller, J. W. Reactivity of Methyl Groups in Actinide Metallocene Amidinate and Triazenido Complexes with Silver and Copper Salts. *Organometallics* **2010**, 29, 101−107.

203) Kiplinger, J. L.; John, K. D.; Morris, D. E.; Scott, B. L.; Burns, C. J. $[(C_5Me_5)_2U(Me)(OTf)]_2$: A New Reagent for Uranium Metallocene Chemistry. Preparation of the First Actinide Hydrazonato Complexes. *Organometallics* **2002**, 21, 4306−4308.

204) Pyykkö, P. Additive Covalent Radii for Single-, Double-, and Triple-Bonded Molecules and Tetrahedrally Bonded Crystals: A Summary. *J. Phys. Chem. A* **2015**, 119, 2326−2337.

205) Rookes, T. M.; Wildman, E. P.; Balazs, G.; Gardner, B. M.; Wooles, A. J.; Gregson, M.; Tuna, F.; Scheer, M.; Liddle, S. T. Actinide−Pnictide (An−Pn) Bonds Spanning Non-Metal, Metalloid, and Metal Combinations (An = U, Th; Pn = P, As, Sb, Bi). *Angew. Chem., Int. Ed.* **2018**, 57, 1332−1336.

206) Wildman, E. P.; Balazs, G.; Wooles, A. J.; Scheer, M.; Liddle, S. T. Thorium−phosphorus triamidoamine complexes containing Th−P single- and multiple-bond interactions. *Nat. Commun.* **2016**, 7, 12884.

207) Edwards, P. G.; Harman, M.; Hursthouse, M. B.; Parry, J. S. The synthesis and crystal structure of the thorium tetraphosphido complex, $Th[P(CH_2CH_2PMe_2)_2]_4$, an actinide complex with only metalphosphorus ligand bonds. *J. Chem. Soc., Chem. Commun.* **1992**, 1469−1470.

208) Garner, M. E.; Arnold, J. Reductive Elimination of Diphosphine from a Thorium−NHC−Bis(phosphido) Complex. *Organometallics* **2017**, 36, 4511−4514.

209) Viesser, R. V.; Ducati, L. C.; Tormena, C. F.; Autschbach, J. The unexpected roles of σ and π orbitals in electron donor and acceptor group effects on the $^{13}C$ NMR chemical shifts in substituted benzenes. *Chem. Sci*. **2017**, 8, 6570−6576.

210) Settineri, N. S.; Arnold, J. Insertion, protonolysis and photolysis reactivity of a thorium monoalkyl amidinate complex. *Chem. Sci*. **2018**, 9, 2831−2841.

211) Vitova, T.; Pidchenko, I.; Fellhauer, D.; Bagus, P. S.; Joly, Y.; Pruessmann, T.; Bahl, S.; Gonzalez-Robles, E.; Rothe, J.; Altmaier, M.; Denecke, M. A.; Geckeis, H. The

role of the 5f valence orbitals of early actinides in chemical bonding. *Nat. Commun*. **2017**, 8, 16053.

212) Neidig, M. L.; Clark, D. L.; Martin, R. L. Covalency in f-element complexes. *Coord. Chem. Rev.* **2013**, 257, 394−406.

213) Löble, M. W.; Keith, J. M.; Altman, A. B.; Stieber, S. C. E.; Batista, E. R.; Boland, K. S.; Conradson, S. D.; Clark, D. L.; Lezama Pacheco, J.; Kozimor, S. A.; Martin, R. L.; Minasian, S. G.; Olson, A. C.; Scott, B. L.; Shuh, D. K.; Tyliszczak, T.; Wilkerson, M. P.; Zehnder, R. A. Covalency in Lanthanides. An X-ray Absorption Spectroscopy and Density Functional Theory Study of $LnCl_6^{x-}$ (x = 3, 2). *J. Am. Chem. Soc.* **2015**, 137, 2506−2523.

214) Minasian, S. G.; Batista, E. R.; Booth, C. H.; Clark, D. L.; Keith, J. M.; Kozimor, S. A.; Lukens, W. W.; Martin, R. L.; Shuh, D. K.; Stieber, S. C. E.; Tylisczcak, T.; Wen, X.-d. Quantitative Evidence for Lanthanide-Oxygen Orbital Mixing in $CeO_2$, $PrO_2$, and $TbO_2$. *J. Am. Chem. Soc*. **2017**, 139, 18052−18064.

215) Minasian, S. G.; Keith, J. M.; Batista, E. R.; Boland, K. S.; Clark, D. L.; Kozimor, S. A.; Martin, R. L.; Shuh, D. K.; Tyliszczak, T. New evidence for 5f covalency in actinocenes determined from carbon Kedge XAS and electronic structure theory. *Chem. Sci.* **2014**, 5, 351− 359.

216) Kozimor, S. A.; Yang, P.; Batista, E. R.; Boland, K. S.; Burns, C. J.; Clark, D. L.; Conradson, S. D.; Martin, R. L.; Wilkerson, M. P.; Wolfsberg, L. E. Trends in Covalency for d- and f-Element Metallocene Dichlorides Identified Using Chlorine K-Edge X-ray Absorption Spectroscopy and Time-Dependent Density Functional Theory. *J. Am. Chem. Soc.* **2009**, 131, 12125−12136.

217) Minasian, S. G.; Krinsky, J. L.; Arnold, J. Evaluating f-Element Bonding from Structure and Thermodynamics. *Chem. - Eur. J.* **2011**, 17, 12234−12245.

218) Barros, N.; Maynau, D.; Maron, L.; Eisenstein, O.; Zi, G.; Andersen, R. A. Single but Stronger UO, Double but Weaker UNMe Bonds: The Tale Told by $Cp_2UO$ and $Cp_2UNR$. *Organometallics* **2007**, 26, 5059−5065.

219) Bagnall, K. W.; Yanir, E. Thorium(IV) and uranium(IV) carbamates. *J. Inorg. Nucl. Chem.* **1974**, 36, 777−779.

220) Brown, D.; Holah, D. G.; Rickard, C. E. F. Structure of thorium(IV) tetrakis-(NN-diethyldithiocarbamate). *J. Chem. Soc. A* **1970**, 423−425.

221) Bagnall, K. W.; Brown, D.; Holah, D. G. Actinide(IV)N,Ndiethyldithiocarbamate complexes. *J. Chem. Soc. A* **1968**, 1149−1153.

222) Boisson, C.; Berthet, J. C.; Ephritikhine, M.; Lance, M.; Nierlich, M. Reactivity of the cationic uranium amide compound $[U(\nu\text{-}C_8H_8)(NEt_2(OC_4H_8)_2][BPh_4]$. *J. Organomet. Chem.* **1996**, 522, 249−257.

223) Charushnikova, I. A.; Fedoseev, A. M.; Polyakova, I. N. Crystal structure of neptunium(IV) N,N-diethyl dithiocarbamate $Np[S_2CN(C_2H_5)_2]_4$. *Russ. J. Coord. Chem.* **2006**, 32, 751−755.

224) Colapietro, M.; Vaciago, A.; Bradley, D. C.; Hursthouse, M. B.; Rendall, I. F. Structural studies of metal dithiocarbamates. Part VI. The crystal and molecular structure of tetrakis(N,Ndiethyldithiocarbamato)titanium(IV). *J. Chem. Soc., Dalton Trans*. **1972**, 1052−1057.

225) Bradley, D. C.; Gitlitz, M. H. N,N-Dialkyldithiocarbamates of transition-metals of Groups IV and V. *Chem. Commun*. **1965**, 289a−289a.

226) Bradley, D. C.; Rendall, I. F.; Sales, K. D. Covalent compounds of quadrivalent transition metals. Part VI. Spectroscopic studies on titanium, vanadium, and zirconium diethyldithiocarbamates. *J. Chem. Soc., Dalton Trans*. **1973**, 2228−2233.

227) Lindmark, A. F.; Fay, R. C. Kinetics of hindered rotation about carbon-nitrogen single bonds in some N,N-diisopropyldithiocarbamates. *Inorg. Chem*. **1983**, 22, 2000−2006.

228) Behnam-Dehkordy, M.; Crociani, B.; Nicolini, M.; Richards, R. L. The reactions of t-BuNC with halides of Titanium(IV), Hafnium(IV), Vanadium(III), Niobium(IV), Molybdenum(V) and Tungsten(VI); insertion into metal halogen bonds and ligand displacement reactions. *J. Organomet. Chem*. **1979**, 181, 69−80.

229) Cantat, T.; Scott, B. L.; Kiplinger, J. L. Convenient access to the anhydrous thorium tetrachloride complexes $ThCl_4(DME)_2$, $ThCl_4(1,4\text{-dioxane})_2$ and $ThCl_4(THF)_{3.5}$ using commercially available and inexpensive starting materials. *Chem. Commun*. **2010**, 46, 919− 921.

230) Ahlrichs, R.; Bar, M.; Hä ser, M.; Horn, H.; Kö lmel, C. Electronic structure calculations on workstation computers: The program system turbomole. *Chem. Phys. Lett.* **1989**, 162, 165−169.

231) Adamo, C.; Barone, V. Toward reliable density functional methods without adjustable parameters: The PBE0 model. *J. Chem. Phys.* **1999**, 110, 6158−6170.

232) Weigend, F.; Ahlrichs, R. Balanced basis sets of split valence, triple zeta valence and quadruple zeta valence quality for H to Rn: Design and assessment of accuracy. *Phys. Chem. Chem. Phys.* **2005**, 7, 3297−3305.

233) Cao, X.; Dolg, M. Segmented contraction scheme for smallcore actinide pseudopotential basis sets. *J. Mol. Struct.: THEOCHEM* **2004**, 673, 203−209.

234) Andrae, D.; Haußermann, U.; Dolg, M.; Stoll, H.; Preuß, H.¨Energy-adjustedab initio pseudopotentials for the second and third row transition elements. *Theor. Chim. Acta* **1990**, 77, 123−141.

235) Küchle, W.; Dolg, M.; Stoll, H.; Preuss, H. Energy-adjusted pseudopotentials for the actinides. Parameter sets and test calculations for thorium and thorium monoxide. *J. Chem. Phys.* **1994**, 100, 7535−7542.

236) Hashem, E.; Swinburne, A. N.; Schulzke, C.; Evans, R. C.; Platts, J. A.; Kerridge, A.; Natrajan, L. S.; Baker, R. J. Emission spectroscopy of uranium(iv) compounds: a combined synthetic, spectroscopic and computational study. *RSC Adv.* **2013**, 3, 4350−4361.

237) Behrle, A. C.; Kerridge, A.; Walensky, J. R. Dithio- and Diselenophosphinate Thorium(IV) and Uranium(IV) Complexes: Molecular and Electronic Structures, Spectroscopy, and Transmetalation Reactivity. *Inorg. Chem.* **2015**, 54, 11625−11636.

238) Bader, R. F. W. Atoms in molecules: a quantum theory. Clarendon Press: Oxford, U.K., **2003**.

239) van Lenthe, E.; Baerends, E. J.; Snijders, J. G. Relativistic total energy using regular approximations. *J. Chem. Phys.* **1994**, 101, 9783− 9792.

240) Ahlrichs, R.; May, K. Contracted all-electron Gaussian basis sets for atoms Rb to Xe. *Phys. Chem. Chem. Phys.* **2000**, 2, 943−945.

241) Pantazis, D. A.; Chen, X.-Y.; Landis, C. R.; Neese, F. AllElectron Scalar Relativistic Basis Sets for Third-Row Transition Metal Atoms. *J. Chem. Theory Comput.* **2008**, 4, 908−919.

242) Pantazis, D. A.; Neese, F. All-Electron Scalar Relativistic Basis Sets for the Actinides. *J. Chem. Theory Comput.* **2011**, 7, 677−684.

243) Muetterties, E. L. Solution state, nuclear magnetic resonance spectral features for tetrakis(N-methyl-N-(perfluorophenyl)dithiocarbamato)zirconium(IV). *Inorg. Chem.* **1974**, 13, 1011−1012.

244) Bruder, A. H.; Fay, R. C.; Lewis, D. F.; Sayler, A. A. Synthesis, characterization, and x-ray structure of $\eta^5$-cyclopentadienyltris(N,N-dimethyldithiocarbamato)zirconium(IV). *J. Am. Chem. Soc*. **1976**, 98, 6932−6938.

245) Behrle, A. C.; Barnes, C. L.; Kaltsoyannis, N.; Walensky, J. R. Systematic Investigation of Thorium(IV)− and Uranium(IV)−Ligand Bonding in Dithiophosphonate, Thioselenophosphinate, and Diselenophosphonate Complexes. *Inorg. Chem.* **2013**, 52, 10623−10631.

246) Di Pietro, P.; Kerridge, A. U−Oyl Stretching Vibrations as a Quantitative Measure of the Equatorial Bond Covalency in Uranyl Complexes: A Quantum-Chemical Investigation. *Inorg. Chem.* **2016**, 55, 573−583.

247) Smiles, D. E.; Wu, G.; Hrobarik, P.; Hayton, T. W. Synthesis, Thermochemistry, Bonding, and $^{13}$C NMR Chemical Shift Analysis of a Phosphorano-Stabilized Carbene of Thorium. *Organometallics* **2017**, 36, 4519−4524.

248) Kerridge, A. Oxidation state and covalency in f-element metallocenes (M = Ce, Th, Pu): a combined CASSCF and topological study. *Dalton Trans.* **2013**, 42, 16428−16436.

249) Kerridge, A. f-Orbital covalency in the actinocenes (An = ThCm): multiconfigurational studies and topological analysis. *RSC Adv.* **2014**, 4, 12078−12086.

250) Cavigliasso, G.; Kaltsoyannis, N. Energy Decomposition Analysis of Metal−Metal Bonding in $[M_2X_8]^{2-}$ (X = Cl, Br) Complexes of 5f (U, Np, Pu), 5d (W, Re, Os), and 4d (Mo, Tc, Ru) Elements. *Inorg. Chem.* **2007**, 46, 3557−3565.

# VITA

Alexander J. Myers was born in Pasadena, California on February 1st, 1985. He was raised in Albuquerque, New Mexico and graduated from La Cueva High School in 2003. He served in the Army from 2003 to 2005, during which time he was deployed to South Korea and Iraq. Alex attended New Mexico State University in January of 2011 and did research with Dr. Michael Johnson where they investigated metal encapsulation and solvation of metal complexes in reverse micelles. He received a Bachelor of Arts in Chemistry in May 2014. In July of 2014 he started his graduate research career in the laboratory of Dr. Justin Walensky at the University of Missouri. During this time, he was awarded a DOE Science Graduate Student Research Program fellowship where he spent 3 months working with Dr. Wayne Lukens at Lawrence Berkeley National Laboratory exploring the magnetic properties of some neptunium compounds. He will receive his Doctor of Philosophy in Chemistry in December of 2019.